REPORT NO.
UCB/SEMM-90/14

STRUCTURAL ENGINEERING
MECHANICS AND MATERIALS

FINITE ELEMENT ANALYSIS OF REINFORCED CONCRETE STRUCTURES UNDER MONOTONIC LOADS

BY

HYO-GYOUNG KWAK
FILIP C. FILIPPOU

NOVEMBER 1990

DEPARTMENT OF CIVIL ENGINEERING
UNIVERSITY OF CALIFORNIA
BERKELEY, CALIFORNIA

FINITE ELEMENT ANALYSIS OF REINFORCED CONCRETE STRUCTURES UNDER MONOTONIC LOADS

by

H. G. Kwak

Visiting Scholar
Korea Advanced Institute of Science and Technology

and

Filip C. Filippou

Associate Professor
Department of Civil Engineering

A Report on Research Conducted under
Grant RTA-59M848 from the
California Department of Transportation

Report No. UCB/SEMM-90/14
Structural Engineering, Mechanics and Materials
Department of Civil Engineering
University of California Berkeley, California

November 1990

ABSTRACT

This study deals with the finite element analysis of the monotonic behavior of reinforced concrete beams, slabs and beam-column joint subassemblages. It is assumed that the behavior of these members can be described by a plane stress field. Concrete and reinforcing steel are represented by separate material models which are combined together with a model of the interaction between reinforcing steel and concrete through bond-slip to describe the behavior of the composite reinforced concrete material. The material behavior of concrete is described by two failure surfaces in the biaxial stress space and one failure surface in the biaxial strain space. Concrete is assumed as a linear elastic material for stress states which lie inside the initial yield surface. For stresses outside this surface the behavior of concrete is described by a nonlinear orthotropic model, whose axes of orthotropy are parallel to the principal strain directions. The concrete stress-strain relation is derived from equivalent uniaxial relations in the axes of orthotropy. The behavior of cracked concrete is described by a system of orthogonal cracks, which follow the principal strain directions and are thus rotating during the load history. Crushing or cracking of concrete takes place when the strains lie outside the ultimate surface in the biaxial strain space.

A new smeared finite element model is proposed based on an improved cracking criterion, which is derived from fracture mechanics principles. This model retains objectivity of the results for very large finite elements, since it considers cracking to be concentrated over a small region around the integration point and not over the entire finite element, as do previous models.

A new reinforcing steel model which is embedded inside a concrete element, but accounts for the effect of bond-slip is developed. This model results in significant savings in the number of nodes needed to account for the effect of bond-slip, particularly, in three dimensional finite element models. A new nonlinear solution scheme is developed in connection with this model.

Finally, correlation studies between analytical and experimental results and several parameter studies are conducted with the objective to establish the validity of the proposed models and identify the significance of various effects on the local and global response of reinforced concrete members. These studies show that the effects of tension-stiffening and bond-slip are very important and should always be included in finite element models of the response of reinforced concrete members. On the other hand, parameters, such as the tensile strength of concrete and the value of the cracked shear constant, do not seem to affect the response of slender beams in bending.

ACKNOWLEDGEMENTS

This report is part of a larger study on the seismic behavior of reinforced concrete highway structures supported by Grant No. RTA-59M848 from the California Department of Transportation (CALTRANS). This support is gratefully acknowledged. Any opinions expressed in this report are those of the authors and do not reflect the views of the sponsoring agency.

TABLE OF CONTENTS

CHAPTER 1
INTRODUCTION

1.1 General

Reinforced concrete (RC) has become one of the most important building materials and is widely used in many types of engineering structures. The economy, the efficiency, the strength and the stiffness of reinforced concrete make it an attractive material for a wide range of structural applications. For its use as structural material, concrete must satisfy the following conditions:

(1) *The structure must be strong and safe.* The proper application of the fundamental principles of analysis, the laws of equilibrium and the consideration of the mechanical properties of the component materials should result in a sufficient margin of safety against collapse under accidental overloads.

(2) *The structure must be stiff and appear unblemished.* Care must be taken to control deflections under service loads and to limit the crack width to an acceptable level.

(3) *The structure must be economical.* Materials must be used efficiently, since the difference in unit cost between concrete and steel is relatively large.

The ultimate objective of design is the creation of a safe and economical structure. Advanced analytical tools can be an indispensable aid in the assessment of the safety and the serviceability of a proposed design. This is, especially, true for many complex modern structures such as nuclear power plants, bridges, off-shore platforms for oil and gas exploration and underground or underwater tunnels, which are subjected to very complex load histories. The safety and serviceability assessment of these structures necessitates the development of accurate and reliable methods and models for their analysis. In addition, the rise in cost of structures encourages engineers to seek more economical alternative designs often resorting to innovative construction methods without lowering the safety of the structure. Intimately related to the increase in scale of modern structures is the extent and impact of disaster in terms of human and economical loss in the event of structural failure. As a result, careful and detailed structural safety analysis becomes more and more necessary. The objective of such an analysis is the investigation of the behavior of the structure under all possible loading conditions, both, monotonic and cyclic, its time-dependent behavior, and, especially, its behavior under overloading.

Reinforced concrete structures are commonly designed to satisfy criteria of serviceability and safety. In order to ensure the serviceability requirement it is necessary to predict the cracking and the deflections of RC structures under service loads. In order to assess the margin of safety of RC structures against failure an accurate estimation of the ultimate load is essential and the prediction of the load-deformation behavior of the structure throughout the range of elastic and inelastic response is desirable.

Within the framework of developing advanced design and analysis methods for modern structures the need for experimental research continues. Experiments provide a firm basis for design equations, which are invaluable in the preliminary design stages. Experimental research also supplies the basic information for finite element models, such as material properties. In addition, the results of finite element models have to be evaluated by comparing them with experiments of full-scale models of structural subassemblages or, even, entire structures. The development of reliable analytical models can, however, reduce the number of required test specimens for the solution of a given problem, recognizing that tests are time-consuming and costly and often do not simulate exactly the loading and support conditions of the actual structure.

The development of analytical models of the response of RC structures is complicated by the following factors:

- Reinforced concrete is a composite material made up of concrete and steel, two materials with very different physical and mechanical behavior;
- Concrete exhibits nonlinear behavior even under low level loading due to nonlinear material behavior, environmental effects, cracking, biaxial stiffening and strain softening;
- Reinforcing steel and concrete interact in a complex way through bond-slip and aggregate interlock.

These complex phenomena have led engineers in the past to rely heavily on empirical formulas for the design of concrete structures, which were derived from numerous experiments. With the advent of digital computers and powerful methods of analysis, such as the finite element method, many efforts to develop analytical solutions which would obviate the need for experiments have been undertaken by investigators. The finite element method has thus become a powerful computational tool, which allows complex analyses of the nonlinear response of RC structures to be carried out in a routine fashion. With this method the importance and interaction of different nonlinear effects on the response of RC structures can be studied analytically. The present study is part of this continuing

effort and concerns the analysis of reinforced concrete beams, slabs, and beam-to-column subassemblages under monotonic loads. A follow-up study will address the response of these structures under cyclic load reversals.

1.2 Literature Survey

A brief review of previous studies on the application of the finite element method to the analysis of reinforced concrete structures is presented is this section. A more detailed description of the underlying theory and the application of the finite element method to the analysis of linear and nonlinear reinforced concrete structures is presented in excellent state-of-the-art reports by the American Society of Civil Engineers in 1982 (ASCE 1982) and 1985 (Meyer and Okamura, eds. 1985).

The earliest publication on the application of the finite element method to the analysis of RC structures was presented by Ngo and Scordelis (1967). In their study, simple beams were analyzed with a model in which concrete and reinforcing steel were represented by constant strain triangular elements, and a special bond link element was used to connect the steel to the concrete and describe the bond-slip effect. A linear elastic analysis was performed on beams with predefined crack patterns to determine principal stresses in concrete, stresses in steel reinforcement and bond stresses. Since the publication of this pioneering work, the analysis of reinforced concrete structures has enjoyed a growing interest and many publications have appeared. Scordelis et al. (1974) used the same approach to study the effect of shear in beams with diagonal tension cracks and accounted for the effect of stirrups, dowel shear, aggregate interlock and horizontal splitting along the reinforcing bars near the support.

Nilson (1972) introduced nonlinear material properties for concrete and steel and a nonlinear bond-slip relationship into the analysis and used an incremental load method of nonlinear analysis. Four constant strain triangular elements were combined to form a quadrilateral element by condensing out the central node. Cracking was accounted for by stopping the solution when an element reached the tensile strength, and reloading incrementally after redefining a new cracked structure. The method was applied to concentric and eccentric reinforced concrete tensile members which were subjected to loads applied at the end of the reinforcing bars and the results were compared with experimental data.

Franklin (1970) advanced the capabilities of the analytical method by developing a nonlinear analysis which automatically accounted for cracking within finite elements and the redistribution of stresses in the structure. This made it possible to trace the response of two-dimensional systems from initial loading to failure in one continuous analysis. Incremental loading with iterations within each

increment was used to account for cracking in the finite elements and for the nonlinear material behavior. Franklin used special frame-type elements, quadrilateral plane stress elements, axial bar members, two-dimensional bond links and tie links to study reinforced concrete frames and RC frames coupled with shear walls.

Plane stress elements were used by numerous investigators to study the behavior of reinforced concrete frame and wall systems. Nayak and Zienkiewicz (1972) conducted two-dimensional stress studies which include the tensile cracking and the elasto-plastic behavior of concrete in compression using an initial stress approach. Cervenka (1970) analyzed shear walls and spandrel beams using an initial stress approach in which the elastic stiffness matrix at the beginning of the entire analysis is used in all iterations. Cervenka proposed a constitutive relationship for the composite concrete-steel material through the uncracked, cracked and plastic stages of behavior.

For the analysis of RC beams with material and geometric nonlinearities Rajagopal (1976) developed a layered rectangular plate element with axial and bending stiffness in which concrete was treated as an orthotropic material. RC beam and slab problems have also been treated by many other investigators (Lin and Scordelis 1975; Bashur and Darwin 1978; Rots et al. 1985; Barzegar and Schnobrich 1986; Adeghe and Collins 1986; Bergmann and Pantazopoulou 1988; Cervenka et al. 1990; Kwak 1990) using similar methods.

Selna (1969) analyzed beams and frames made up of one-dimensional elements with layered cross sections which accounted for progressive cracking and changing material properties through the depth of the cross section as a function of load and time. Significant advances and extensions of the finite element analysis of reinforced concrete beams and frames to include the effects of heat transfer due to fire, as well as the time-dependent effects of creep and shrinkage, were made by Becker and Bresler (1974).

Two basically different approaches have been used so far for the analysis of RC slabs by the finite element method: the modified stiffness approach and the layer approach. The former is based on an average moment-curvature relationship which reflects the various stages of material behavior, while the latter subdivides the finite element into imaginary concrete and steel layers with idealized stress-strain relations for concrete and reinforcing steel.

Experimental and analytical studies of RC slabs were conducted by Joffriet and McNeice (1971). The analyses were based on a bilinear moment-curvature relation which was derived from an empirically determined effective moment of inertia of the cracked slab section including the effect

of tension stiffening. The change in bending stiffness of the elements due to cracking normal to the principal moment direction is accounted for by reducing the flexural stiffness of the corresponding element.

Dotroppe et al. (1973) used a layered finite element procedure in which slab elements were divided into layers to account for the progressive cracking through the slab thickness. Scanlon and Murray (1974) have developed a method of incorporating both cracking and time-dependent effects of creep and shrinkage in slabs. They used layered rectangular slab elements which could be cracked progressively layer by layer, and assumed that cracks propagate only parallel and perpendicular to orthogonal reinforcement. Lin and Scordelis (1975) utilized layered triangular finite elements in RC shell analysis and included the coupling between membrane and bending effects, as well as the tension stiffening effect of concrete between cracks in the model.

The finite element analysis of an axisymmetric solid under axisymmetric loading can be readily reduced to a two-dimensional analysis. Bresler and Bertero (1968) used an axisymmetric model to study the stress distribution in a cylindrical concrete specimen reinforced with a single plain reinforcing bar. The specimen was loaded by applying tensile loads at the ends of the bar.

In one of the pioneering early studies Rashid (1968) introduced the concept of a "smeared" crack in the study of the axisymmetric response of prestressed concrete reactor structures. Rashid took into account cracking and the effects of temperature, creep and load history in his analyses. Today the smeared crack approach of modeling the cracking behavior of concrete is almost exclusively used by investigators in the nonlinear analysis of RC structures, since its implementation in a finite element analysis program is more straightforward than that of the discrete crack model. Computer time considerations also favor the smeared crack model in analyses, which are concerned with the global response of structures. At the same time the concerted effort of many investigators in the last 20 years has removed many of the limitations of the smeared crack model (ASCE 1982; Meyer and Okamura, eds. 1985).

Gilbert and Warner (1978) used the smeared crack model and investigated the effect of the slope of the descending branch of the concrete stress-strain relation on the behavior of RC slabs. They were among the first to point out that analytical results of the response of reinforced concrete structures are greatly influenced by the size of the finite element mesh and by the amount of tension stiffening of concrete. Several studies followed which corroborated these findings and showed the effect of mesh size (Bazant and Cedolin 1980; Bazant and Oh 1983; Kwak 1990) and tension stiffening (Barzegar and Schnobrich 1986; Leibengood et al. 1986) on the accuracy of finite element analyses of RC structures with the smeared crack model. In order to better account for the tension stiffening effect of concrete between cracks some investigators have artificially increased the stiffness of

reinforcing steel by modifying its stress-strain relationship (Gilbert and Warner 1977). Others have chosen to modify the tensile stress-strain curve of concrete by including a descending post-peak branch (Lin and Scordelis 1975; Vebo and Ghali 1977; Barzegar and Schnobrich 1986; Abdel Rahman and Hinton 1986).

In the context of the smeared crack model two different representations have emerged: the fixed crack and the rotating crack model. In the fixed crack model a crack forms perpendicular to the principal tensile stress direction when the principal stress exceeds the concrete tensile strength and the crack orientation does not change during subsequent loading. The ease of formulating and implementing this model has led to its wide-spread used in early studies (Hand et al. 1973; Lin and Scordelis 1975). Subsequent studies, however, showed that the model is associated with numerical problems caused by the singularity of the material stiffness matrix. Moreover, the crack pattern predicted by the finite element analysis often shows considerable deviations from that observed in experiments (Jain and Kennedy 1974).

The problems of the fixed crack model can be overcome by introducing a cracked shear modulus, which eliminates most numerical difficulties of the model and considerably improves the accuracy of the crack pattern predictions. The results do not seem to be very sensitive to the value of the cracked shear modulus (Vebo and Ghali 1977; Barzegar and Schnobrich 1986), as long as a value which is greater than zero is used, so as to eliminate the singularity of the material stiffness matrix and the associated numerical instability. Some recent models use a variable cracked shear modulus to represent the change in shear stiffness, as the principal stresses in the concrete vary from tension to compression (Balakrishnan and Murray 1988; Cervenka et al. 1990).

de Borst and Nauta (1985) have proposed a model in which the total strain rate is additively decomposed into a concrete strain rate and a crack strain rate. The latter is, in turn, made up of several crack strain components. After formulating the two-dimensional concrete stress-strain relation and transforming from the crack direction to the global coordinate system of the structure, a material matrix with no coupling between normal and shear stress is constructed. In spite of its relative simplicity and ease of application, this approach still requires the selection of a cracked shear modulus of concrete.

In the rotating crack model proposed by Cope et al. (1980) the crack direction is not fixed during the subsequent load history. Several tests by Vecchio and Collins (1982) have shown that the crack orientation changes with loading history and that the response of the specimen depends on the current rather than the original crack direction. In the rotating crack model the crack direction is kept perpendicular to the direction of principal tensile strain and, consequently, no shear strain occurs in the crack plane. This eliminates the need for a cracked shear modulus. A disadvantage of this approach

is the difficulty of correlating the analytical results with experimental fracture mechanics research, which is at odds with the rotating crack concept. This model has, nonetheless, been successfully used in analytical studies of RC structures, whose purpose is to study the global structural behavior, rather than the local effects in the vicinity of a crack (Gupta and Akbar 1983; Adeghe and Collins 1986).

While the response of lightly reinforced beams in bending is very sensitive to the effect of tension stiffening of concrete, the response of RC structures in which shear plays an important role, such as over-reinforced beams and shear walls, is much more affected by the bond-slip of reinforcing steel than the tension stiffening of concrete. To account for the bond-slip of reinforcing steel two different approaches are common in the finite element analysis of RC structures. The first approach makes use of the bond link element proposed by Ngo and Scordelis (1967). This element connects a node of a concrete finite element with a node of an adjacent steel element. The link element has no physical dimensions, i.e. the two connected nodes have the same coordinates.

The second approach makes use of the bond-zone element developed by de Groot et al. (1981). In this element the behavior of the contact surface between steel and concrete and of the concrete in the immediate vicinity of the reinforcing bar is described by a material law which considers the special properties of the bond zone. The contact element provides a continuous connection between reinforcing steel and concrete, if a linear or higher order displacement field is used in the discretization scheme. A simpler but similar element was proposed by Keuser and Mehlhorn (1987), who showed that the bond link element cannot represent adequately the stiffness of the steel-concrete interface.

Even though many studies of the bond stress-slip relationship between reinforcing steel and concrete have been conducted, considerable uncertainty about this complex phenomenon still exists, because of the many parameters which are involved. As a result, most finite element studies of RC structures do not account for bond-slip of reinforcing steel and many researchers express the opinion that this effect in included in the tension-stiffening model.

Very little work has been done, so far, on the three-dimensional behavior of reinforced concrete systems using solid finite elements, because of the computational effort involved and the lack of knowledge of the material behavior of concrete under three-dimensional stress states. Suidan and Schnobrich (1973) were the first to study the behavior of beams with 20-node three-dimensional isoparametric finite elements. The behavior of concrete in compression was assumed elasto-plastic based on the von-Mises yield criterion. A coarse finite element mesh was used in these analyses for cost reasons.

In spite of the large number of previous studies on the nonlinear finite element analysis of reinforced concrete structures, only few conclusions of general applicability have been arrived at. The inclusion of the effects of tension stiffening and bond-slip is a case in point. Since few rational models of this difficult problem have been proposed so far, it is rather impossible to assess exactly what aspects of the behavior are included in each study and what the relative contribution of each is. Similar conclusions can be reached with regard to other aspects of the finite element analysis. Even though the varying level of sophistication of proposed models is often motivated by computational cost considerations, the multitude of proposed approaches can lead to the conclusion that the skill and experience of the analyst is the most important aspect of the study and that the selection of the appropriate model depends on the problem to be solved.

Recognizing that many of the previously proposed models and methods have not been fully verified so far, it is the intent of this study to address some of the model selection issues, in particular, with regard to the effects of tension-stiffening and bond-slip.

1.3 Objectives and Scope

The present investigation of the nonlinear response to failure of RC structures under short term monotonic loads was initiated with the intent to investigate the relative importance of several factors in the nonlinear finite element analysis of RC structures: these include the effect of tension-stiffening and bond-slip and their relative importance on the response of under- and over-reinforced beams and slabs, the effect of size of the finite element mesh on the analytical results, the effect of the nonlinear behavior of concrete and steel on the response of under- and over-reinforced beams and slabs. In the progress of this study improved material models were developed and included in the analysis. These are presently extended to study the behavior of RC structures under cyclic loads, which will be the subject of a future report.

The main objectives of this study are:

- To develop improved analytical models for the study of the nonlinear behavior of RC beams, slabs and beam-column joints under short term monotonic loads. These models should be simple enough to allow extension to cyclic loading conditions without undue computational cost.
- To investigate the relative importance of the nonlinear behavior of concrete, reinforcing steel and their interaction through bond-slip on the response of under- and over-reinforced concrete beams and slabs.

- To investigate the effect of size of the finite element mesh on the results of the nonlinear analysis of RC structures and to develop an improved criterion for reducing the numerical error associated with large finite element mesh size.
- To investigate the relative contribution of bond-slip and tension stiffening to the post-cracking stiffness of under- and over-reinforced beams and beam-column joints.
- To investigate the effect of material and numerical parameters, such as concrete tensile strength and shear retention factor, on the response of reinforced concrete beams.

Following the introduction and a brief review of previous studies in Chapter 1 Chapter 2 deals with the description of the material behavior of concrete and reinforcing steel and their interaction through bond-slip. The behavior of concrete and reinforcing steel is modeled independently. A new discrete, embedded steel model is developed which accounts for the relative slip between reinforcing steel and concrete. The behavior of concrete under biaxial loading conditions is described by a nonlinear orthotropic model, in which the axes of orthotropy coincide with the principal strain directions (rotating crack model). The effect of size of the finite element mesh is discussed in connection with a new smeared crack model and an improved criterion is derived from fracture mechanics considerations in order to reduce the numerical error associated with large size finite elements.

Chapter 3 discusses the inclusion of the material models in a finite element for plane stress analysis of RC beams. A new plate bending element is also developed based on the Mindlin plate theory and the layer concept. The element accounts for shear deformations and is capable of modeling the gradual propagation of cracks through the depth of the slab. Chapter 3 concludes with a discussion of computational aspects of the solution. The iteration scheme and the resulting nonlinear solution procedure are described along with the associated convergence criteria. A special purpose nonlinear solution is developed for the solution of the embedded discrete bar model with bond-slip.

The validity of the proposed models is established by comparing the analytical predictions with results from experimental and previous analytical studies in Chapter 4. Finally, Chapter 5 presents the conclusions of this study along with recommendations for future work.

CHAPTER 2
MATERIAL MODELING

2.1 General

Reinforced concrete structures are made up of two materials with different characteristics, namely, concrete and steel. Steel can be considered a homogeneous material and its material properties are generally well defined. Concrete is, on the other hand, a heterogeneous material made up of cement, mortar and aggregates. Its mechanical properties scatter more widely and cannot be defined easily. For the convenience of analysis and design, however, concrete is often considered a homogeneous material in the macroscopic sense.

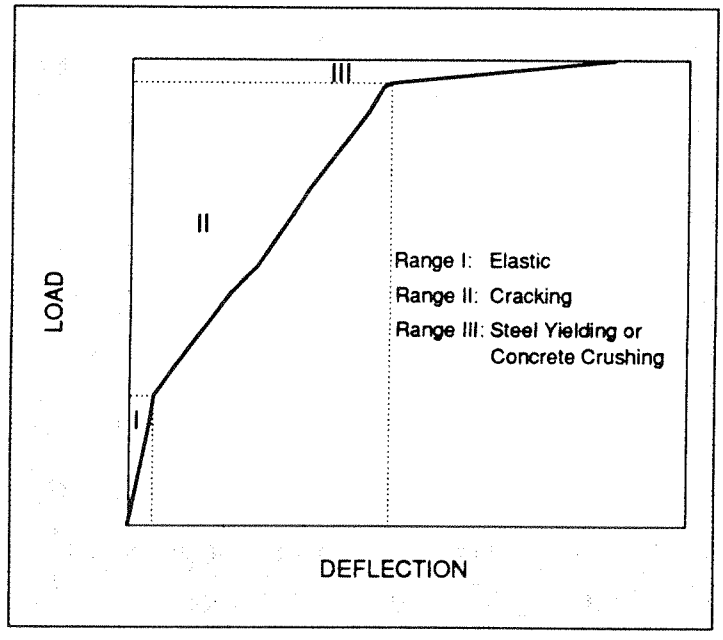

Fig. 2.1 Typical Load-Displacement Relationship for a R/C Element

The typical stages in the load-deformation behavior of a reinforced concrete simply supported beam are illustrated in Fig. 2.1. Similar relations are obtained for other types of reinforced concrete structural elements. This highly nonlinear response can be roughly divided into three ranges of behavior: the uncracked elastic stage, the crack propagation and the plastic (yielding or crushing) stage.

The nonlinear response is caused by two major effects, namely, cracking of concrete in tension, and yielding of the reinforcement or crushing of concrete in compression. Nonlinearities also arise from the interaction of the constituents of reinforced concrete, such as bond-slip between reinforcing steel and surrounding concrete, aggregate interlock at a crack and dowel action of the reinforcing steel crossing a crack. The time-dependent effects of creep, shrinkage and temperature variation also contribute to the nonlinear behavior. Furthermore, the stress-strain relation of concrete is not only nonlinear, but is different in tension than in compression and the mechanical properties are dependent on concrete age at loading and on environmental conditions, such as ambient temperature and humidity. The material properties of concrete and steel are also strain-rate dependent to a different extent.

Because of these differences in short- and long-term behavior of the constituent materials, a general purpose model of the short- and long-term response of RC members and structures should be based on separate material models for reinforcing steel and concrete, which are then combined along with models of the interaction between the two constituents to describe the behavior of the composite reinforced concrete material. This is the approach adopted in this study. The assumptions made in the description of material behavior are summarized below:

- The stiffness of concrete and reinforcing steel is formulated separately. The results are then superimposed to obtain the element stiffness;
- The smeared crack model is adopted in the description of the behavior of cracked concrete;
- Cracking in more than one direction is represented by a system of orthogonal cracks;
- The crack direction changes with load history (rotating crack model);
- The reinforcing steel is assumed to carry stress along its axis only and the effect of dowel action of reinforcement is neglected;
- The transfer of stresses between reinforcing steel and concrete and the resulting bond-slip is explicitly accounted for in a new discrete reinforcing steel model, which is embedded in the concrete element.

In the following the behavior of each constituent material and the derivation of the corresponding material stiffness matrix is discussed separately. This is followed by the model of the interaction between reinforcing steel and concrete through bond. The superposition of the individual material stiffness matrices to form the stiffness of the composite reinforced concrete material and the numerical implementation of this approach in the nonlinear analysis of beams and slabs is discussed in the next chapter.

2.2 Concrete

2.2.1 Behavior of Concrete

Concrete exhibits a large number of microcracks, especially, at the interface between coarser aggregates and mortar, even before subjected to any load. The presence of these microcracks has a great effect on the mechanical behavior of concrete, since their propagation during loading contributes to the nonlinear behavior at low stress levels and causes volume expansion near failure. Many of these microcracks are caused by segregation, shrinkage or thermal expansion of the mortar. Some microcracks may develop during loading because of the difference in stiffness between aggregates and mortar. Since the aggregate-mortar interface has a significantly lower tensile strength than mortar, it constitutes the weakest link in the composite system. This is the primary reason for the low tensile strength of concrete.

The response of a structure under load depends to a large extent on the stress-strain relation of the constituent materials and the magnitude of stress. Since concrete is used mostly in compression, the stress-strain relation in compression is of primary interest. Such a relation can be obtained from cylinder tests with a height to diameter ratio of 2 or from strain measurements in beams.

The concrete stress-strain relation exhibits nearly linear elastic response up to about 30% of the compressive strength. This is followed by gradual softening up to the concrete compressive strength, when the material stiffness drops to zero. Beyond the compressive strength the concrete stress-strain relation exhibits strain softening until failure takes place by crushing.

2.2.2 Concrete Models

Many mathematical models of the mechanical behavior of concrete are currently in use in the analysis of reinforced concrete structures. These can be divided into four main groups: orthotropic models, nonlinear elasticity models, plastic models and endochronic models (Chen 1976, ASCE 1982, Meyer and Okamura, eds. 1985).

The orthotropic model is the simplest. It can match rather well experimental data under proportional biaxial loading and approximates the concrete behavior under general biaxial loading adequately. The model was also found capable of representing the hysteretic behavior of concrete under cyclic loading (Darwin and Pecknold 1977). It is particularly suitable for the analysis of reinforced concrete beams, panels and shells, since the stress state of these structures is predominantly biaxial, and the model can be calibrated against an extensive experimental data base. The equivalent uniaxial strain model was recently extended to monotonic triaxial behavior (Chen 1976; ASCE 1982).

The nonlinear elasticity model is based on the concept of variable moduli and matches well several available test data. In the pre-failure regime unique approximate relationships have been established between hydrostatic and volumetric strain and between deviatoric stress and strain. From these relationships expressions for the tangent bulk and shear modulus can be derived. Thus, the nonlinear response of concrete is simulated by a piecewise linear elastic model with variable moduli. The model is, therefore, computationally simple and is particularly well suited for finite element calculations. When unloading takes place, the behavior can be approximated by moduli which are different from those at loading. The model exhibits, however, continuity problems for stress paths near neutral loading. As a result, the variable moduli model is unable to describe accurately the behavior of concrete under high stress, near the compressive strength and in the strain softening range.

The plastic model, especially, the strain hardening plastic model can be considered as a generalization of the previous models. The formulation of the constitutive relations in the strain hardening plastic model is based on three fundamental assumptions: (1) the shape of the initial yield surface; (2) the evolution of the loading surface, i.e. the hardening rule; and (3) the formulation of an appropriate flow rule. Even though this model represents successfully the behavior in the strain hardening region, the strain softening behavior of concrete beyond the peak stress cannot be described adequately by the classical theory of work-hardening plasticity which is based on Drucker's postulate of material stability. It is, therefore, not appropriate to use this model in the analysis of reinforced concrete structures which experience strain softening. The model is, nevertheless, used extensively in the study of concrete behavior, since the introduction of additional assumptions renders it capable of simulating the behavior of concrete with sufficient accuracy (Chen 1976; Arnesen et al. 1980).

The endochronic theory of plasticity is based on the concept of intrinsic or endochronic time. The intrinsic time is used to measure the extent of damage in the internal structure of the concrete material under general deformation histories. Many features of concrete behavior may be represented by this theory without need for loading-unloading conditions. The introduction of loading criteria becomes, however, necessary for an accurate material representation. The most logical way of accomplishing this is by introducing loading surfaces and plasticity hardening rules. Recent applications have clearly demonstrated the power of the endochronic approach (ASCE 1982). Further research, is, however, needed to refine the theory, and to reduce the number of material constants which describe the material behavior.

A very promising model has been recently proposed by Bazant and Ozbolt (1989). The so-called microplane model seems to be capable of representing quite well several features of the monotonic

and triaxial behavior of concrete and is thus, particularly, well suited for local analyses of reinforced concrete structures. It is, however, very expensive computationally and its use in the analysis of large scale structures does not appear feasible at present.

The orthotropic model is adopted in this study for its simplicity and computational efficiency. The ultimate objective of this work is the response analysis of large structures under cyclic loads for which the endochronic and the microplane model are prohibitively expensive.

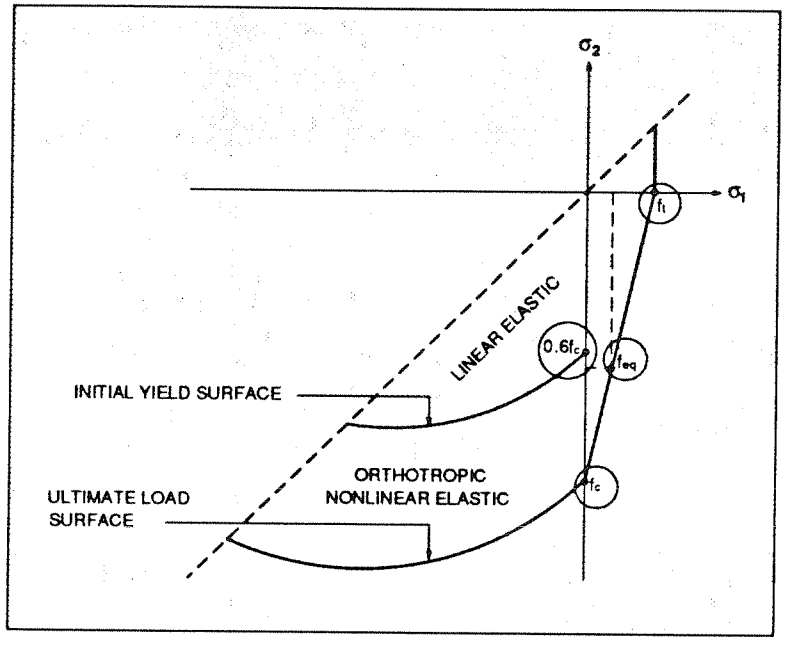

Fig. 2.2 Strength Failure Envelope of Concrete

Under combinations of biaxial compressive stress concrete exhibits strength and stress-strain behavior which is different from that under uniaxial loading conditions. Fig. 2.2 shows the biaxial strength envelope of concrete under proportional loading (Kupfer et al. 1969; Tasuji et al. 1978). Under biaxial compression concrete exhibits an increase in compressive strength of up to 25% of the uniaxial compressive strength, when the stress ratio σ_1/σ_2 is 0.5. When the stress ratio σ_1/σ_2 is equal to 1 the concrete compressive strength is approximately $1.16 \cdot f_c$, where f_c is the uniaxial concrete compressive strength. Under biaxial tension concrete exhibits constant or perhaps slightly increased tensile strength compared with that under uniaxial loading. Under a combination of tension and compression the compressive strength decreases almost linearly with increasing principal tensile stress (Fig. 2.2).

The principal stress ratio also affects the stiffness and strain ductility of concrete. Under biaxial compression concrete exhibits an increase in initial stiffness which may be attributed to Poisson's effect. It also exhibits an increase in strain ductility indicating that less internal damage takes place

under biaxial compression than under uniaxial loading. More details are presented by Kupfer et al. (1969), Chen (1976), and Tasuji et al. (1978). Even though the principal compressive strain and the principal tensile strain at failure decrease with increasing tensile stress in the compression-tension region, failure basically takes place by cracking and the principal compressive stress and strain remain in the ascending branch of the concrete stress-strain relation.

Since most of a beam or slab which is subjected to bending moments, experiences biaxial stress combinations in the tension-tension or compression-compression region and only small portions near the supports lie in the compression-tension region, the proposed concrete model uses a different degree of approximation in each region of the biaxial stress and strain space.

The behavior of the model depends on the location of the present stress state in the principal stress space in Fig. 2.2. In the biaxial compression region the model remains linear elastic for stress combinations inside the initial yield surface in Fig. 2.2. Both the initial yield and the ultimate load surface are described by the expression proposed by Kupfer et al. (1969) (Fig. 2.2)

$$F = \frac{(\sigma_1 + \sigma_2)^2}{(\sigma_2 + 3.65\sigma_1)} - A f_c = 0 \tag{2.1}$$

where σ_1 and σ_2 are the principal stresses, f_c is the uniaxial compressive strength and A is a parameter. A=0.6 defines the initial yield surface, while A=1.0 defines the ultimate load surface under biaxial compression.

For stress combinations outside the initial yield surface but inside the ultimate failure surface the behavior of concrete is described by a nonlinear elastic orthotropic model. This model derives the biaxial stress-strain behavior from equivalent uniaxial stress-strain relations in the axes of orthotropy.

In describing the uniaxial stress-strain behavior of concrete many empirical formulas have been proposed. These are summarized by Popovics (1969) and ASCE (1982). Fig. 2.3a shows the simplest of the nonlinear models, the linearly elastic-perfectly plastic model, which was used by Lin and Scordelis (1975) in a study of reinforced concrete slabs and walls. Fig. 2.3b shows the inelastic-perfectly plastic model proposed by the European Concrete Committee (CEB 1978) made up of a parabola and a horizontal line. The model proposed by Hognestad (1951) is shown in Fig. 2.3c. This model is capable of representing quite well the uniaxial stress-strain behavior of a wide range of concretes. Finally, Fig. 2.3d shows a piecewise linear model in which the nonlinear stress-strain

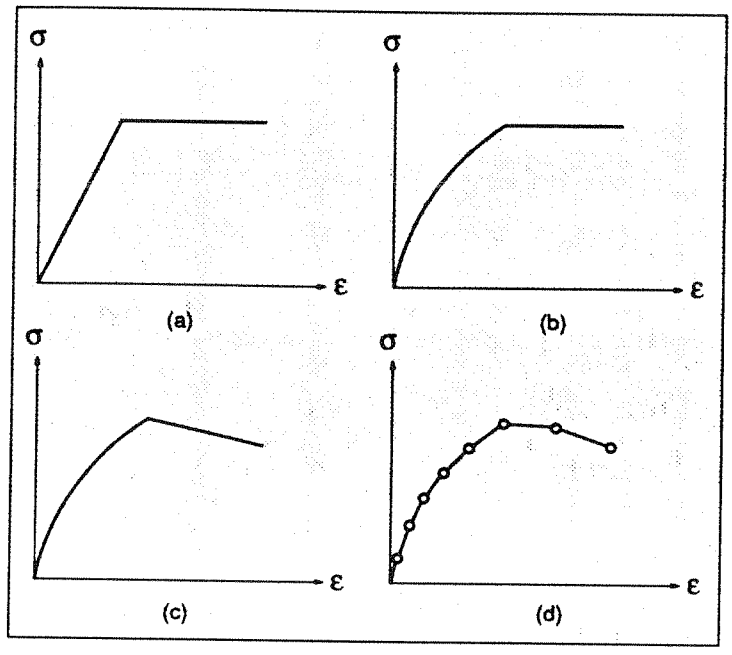

Fig. 2.3 Idealization of Stress-Strain Curve of Concrete

relation is approximated by a series of straight line segments. Although this is the most versatile model capable of representing a wide range of stress-strain curves, its use is restricted to cases in which experimental data for the uniaxial concrete stress-strain relation are available.

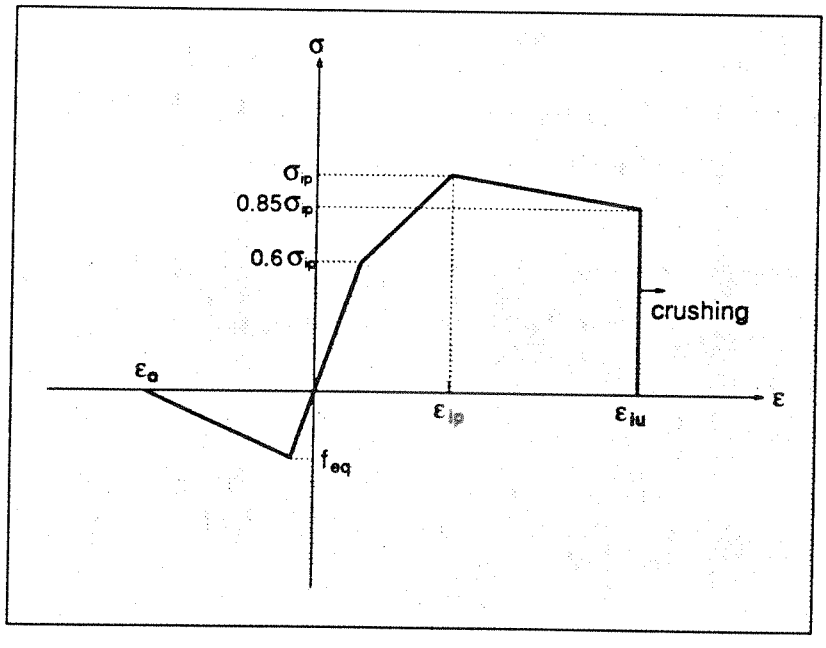

Fig. 2.4 Stress-Strain Relation of Concrete

In the present study the model of Hognestad (1951) is used after some modifications. These modifications are introduced in order to increase the computational efficiency of the model, and in view of the fact that the response of typical reinforced concrete structures is much more affected by the tensile than by the compressive behavior of concrete. This stems from the fact that the concrete tensile strength is generally less than 20% of the compressive strength. In typical reinforced concrete beams and slabs which are subjected to bending, the maximum compressive stress at failure does not reach the compressive strength. This means that the compressive stresses in most of the member reach a small fraction of the compressive strength at failure. The behavior of these members is, therefore, dominated by crack formation and propagation, and the yielding of reinforcing steel.

The equivalent concrete compressive strength in each axis of orthotropy σ_{ip} is determined from the biaxial failure surface of concrete, where i is equal to 1 or 2. In order to simplify the concrete material model the stress-strain relation in compression is assumed piecewise linear with three branches. The material remains linear elastic up to a stress of $0.6 \cdot \sigma_{ip}$ (Fig. 2.4), since at a stress between 50% to 70% of σ_{ip} cracks at nearby aggregate surfaces start to bridge in the form of mortar cracks and other bond cracks continue to grow slowly. Beyond this stress the behavior is assumed linear up to the compressive strength σ_{ip} followed by a linear descending branch which represents strain softening. The strain ε_{ip} at the compressive strength σ_{ip} in Fig. 2.4 is determined so as to match the strain energy in compression of the uniaxial experimental stress-strain curve.

When the biaxial stresses exceed Kupfer's failure envelope, concrete enters into the strain softening range of behavior where a linear orthotropic model describes the biaxial behavior (Darwin and Pecknold 1977). In this region failure occurs by crushing of concrete when the principal compressive strain exceeds the limit value ε_{iu} in Fig. 2.4. In order to define the crushing of concrete under biaxial compressive strains a strain failure surface is used as ultimate failure criterion. This surface, which is shown in Fig. 2.5, is described by the following equation in complete analogy to Kupfer's stress failure envelope in Eq. 2.1:

$$C = \frac{(\varepsilon_1 + \varepsilon_2)^2}{(\varepsilon_2 + 3.65\varepsilon_1)} - \varepsilon_{cu} = 0 \qquad (2.2)$$

where ε_1 and ε_2 are the principal strains and ε_{cu} is the ultimate strain of concrete in uniaxial loading. For strain combinations outside the strain failure surface the element is assumed to lose its strength completely and is not able to carry any more stress.

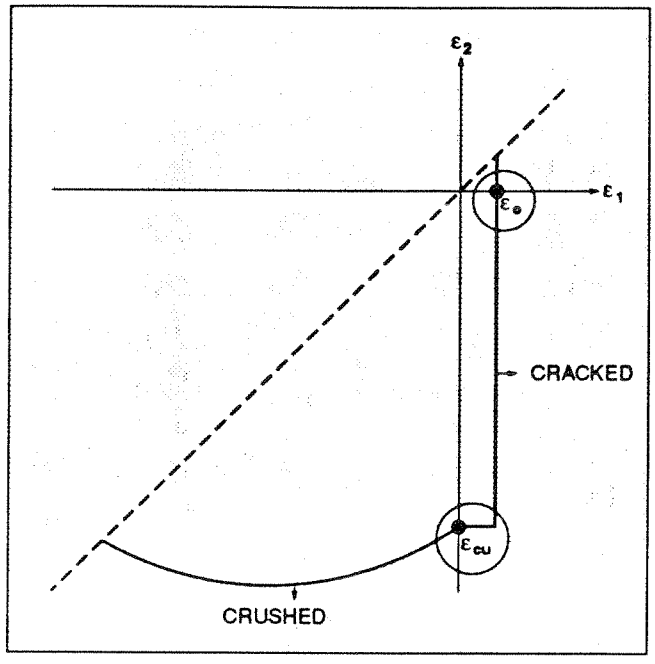

Fig. 2.5 Strain Failure Envelope of Concrete

The equations which define the parameters of the equivalent uniaxial stress-strain relation in the main axes of orthotropy can now be summarized for the compression-compression region of the principal stress space. Denoting the principal stress ratio by α

$$\alpha = \frac{\sigma_1}{\sigma_2} \qquad \text{where} \qquad (\ |\sigma_1| \geq |\sigma_2| \ ) \tag{2.3}$$

yields the following equations

$$\sigma_{2p} = \frac{1 + 3.65\alpha}{(1+\alpha)^2} \cdot f_c \tag{2.4}$$

$$\varepsilon_{2p} = \varepsilon_{co} \cdot \left(3\frac{\sigma_{2p}}{f_c} - 2 \right) \tag{2.5}$$

$$\sigma_{1p} = \alpha \cdot \sigma_{2p} \tag{2.6}$$

$$\varepsilon_{1p} = \varepsilon_{co} \cdot \left[-1.6 \cdot \left(\frac{\sigma_{1p}}{f_c} \right)^3 + 2.25 \cdot \left(\frac{\sigma_{1p}}{f_c} \right)^2 + 0.35 \cdot \left(\frac{\sigma_{1p}}{f_c} \right) \right] \tag{2.7}$$

where ε_{co} is the strain corresponding to the concrete compressive strength f_c under uniaxial stress conditions.

In the biaxial compression-tension and tension-tension region the following assumptions are adopted in this study: (1) failure takes place by cracking and, therefore, the tensile behavior of concrete dominates the response; (2) the uniaxial tensile strength of concrete is reduced to the value f_{eq}, as shown in Figs. 2.2 and 2.4 to account for the effect of the compressive stress; in the tension-tension region the tensile strength remains equal to the uniaxial tensile strength f_t in Fig. 2.4; (3) the concrete stress-strain relation in compression is the same as under uniaxial loading and does not change with increasing principal tensile stress. Thus σ_{ip} in Fig. 2.4 is equal to f_c and ε_{iu} is equal to ε_{cu}. The last assumption holds true in the range of compressive stresses which is of practical interest in typically reinforced beams and slabs.

The proposed model assumes that concrete is linear elastic in the compression-tension and the biaxial tension region for tensile stresses smaller than f_{eq} in Fig. 2.4. Beyond the tensile strength the tensile stress decreases linearly with increasing principal tensile strain (Fig. 2.4). Ultimate failure in the compression-tension and the tension-tension region takes place by cracking, when the principal tensile strain exceeds the value ε_o in Fig. 2.4. This results in the strain failure surface of Fig. 2.5. The value of ε_o is derived from fracture mechanics concepts, as will be described in the following section. When the principal tensile strain exceeds ε_o, the material only loses its tensile strength normal to the crack, while it is assumed to retain its strength parallel to the crack direction.

2.2.3 Behavior of Cracked Concrete

2.2.3.1 Description of a Cracked Section

The nonlinear response of concrete is often dominated by progressive cracking which results in localized failure. Fig. 2.6a depicts part of a reinforced concrete member in flexure. The member has cracked at discrete locations where the concrete tensile strength is exceeded. At the cracked section all tension is carried by the steel reinforcement. Tensile stresses are, however, present in the concrete between the cracks, since some tension is transferred from steel to concrete through bond. The magnitude and distribution of bond stresses between the cracks determines the distribution of tensile stresses in the concrete and the reinforcing steel between the cracks.

Additional cracks can form between the initial cracks, if the tensile stress reaches the tensile strength of concrete between previously formed cracks. The final cracking state is reached when a tensile force of sufficient magnitude to form an additional crack between two existing cracks can no longer be transferred by bond from steel to concrete. Figs. 2.6c, 2.6d and 2.6e show the idealized

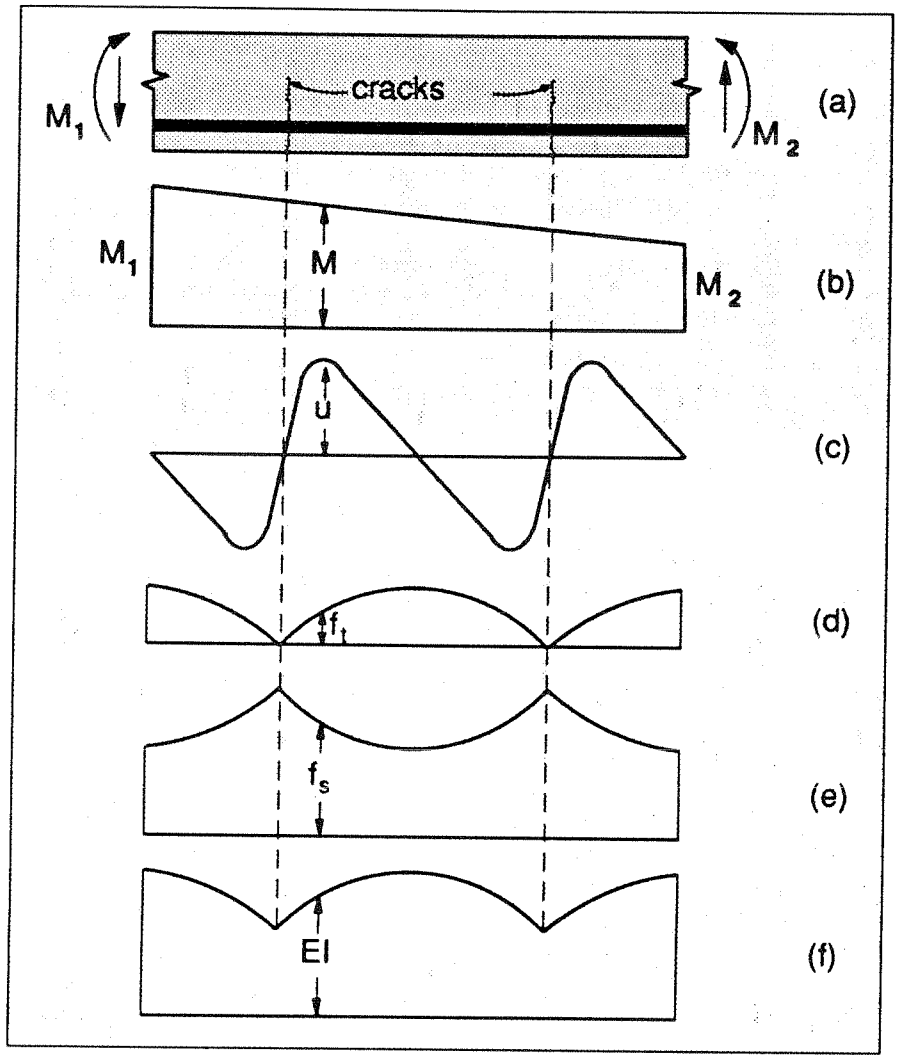

Fig. 2.6 ***Effect of Cracking in Reinforced Concrete Beam***
(a) Portion of Beam
(b) Bending Moment Distribution
(c) Bond Stress Distribution
(d) Concrete Tensile Stress Distribution
(e) Steel Tensile Stress Distribution
(f) Flexural Stiffness Distribution in Elastic Range

distribution between cracks of bond stress, concrete tensile stress and steel tensile stress, respectively. Because concrete is carrying some tension between the cracks, the flexural rigidity is clearly greater between the cracks than at the cracks, as shown in Fig. 2.6f (Park and Paulay 1975).

In order to improve the accuracy of finite element models in representing cracks and, in some cases, in order to improve the numerical stability of the solution the tension stiffening effect was introduced in several models. The physical behavior in the vicinity of a crack can be inferred from Figs. 2.6d and 2.6e. As the concrete reaches its tensile strength, primary cracks form. The number and the extent of cracks are controlled by the size and placement of the reinforcing steel. At the primary cracks the concrete stress drops to zero and the steel carries the entire tensile force. The concrete between the cracks, however, still carries some tensile stress, which decreases with increasing load magnitude. This drop in concrete tensile stress with increasing load is associated with the breakdown of bond between reinforcing steel and concrete. At this stage a secondary system of internal cracks, called bond cracks, develops around the reinforcing steel, which begins to slip relative to the surrounding concrete.

Since cracking is the major source of material nonlinearity in the serviceability range of reinforced concrete structures, realistic cracking models need to be developed in order to accurately predict the load-deformation behavior of reinforced concrete members. The selection of a cracking model depends upon the purpose of the finite element analysis. If overall load-deflection behavior is of primary interest, without much concern for crack patterns and estimation of local stresses, the "smeared" crack model is probably the best choice. If detailed local behavior is of interest, the adoption of a "discrete" crack model might be necessary.

Unless special connecting elements and double nodes are introduced in the finite element discretization of the structure, the well established "smeared" crack model results in perfect bond between steel and concrete, because of the inherent continuity of the displacement field. In this case the steel stress at the cracks will be underestimated.

One way of including the tension stiffening effect in the smeared crack model is to increase the average stiffness of the finite element which contains the crack. Considering that the finite element has relatively large dimensions compared to the size of the cracked section two methods have been proposed. In the first method the tension portion of the concrete stress-strain curve is assigned a descending branch. In this case the tension stiffening effect is represented as either a step-wise reduction of tensile stress or as a gradually unloading model (Lin and Scordelis 1975; Gilbert and Warner 1977; Barzegar and Schnobrich 1986). Even in terms of plain concrete this is not completely unrealistic, since the stiffness of the test loading apparatus affects the strain softening stiffness in tension and disagreement exists on the ability of concrete to carry stress beyond the ultimate tensile strength. In the second tension stiffening model the steel stiffness is increased (Gilbert and Warner

1977, Cervenka et al. 1990). The additional stress in the reinforcing steel represents the tensile force carried by the concrete between the cracks. For reasons of computational convenience it is assumed that the orientation of this additional stress coincides with the orientation of the reinforcing steel.

2.2.3.2 Crack Models

The first reinforced concrete finite element model which includes the effect of cracking was developed by Ngo and Scordelis (1967), who carried out a linear elastic analysis of beams with predefined crack patterns. The cracks were modeled by separating the nodal points of the finite element mesh and thus creating a discrete crack model. With the change of topology and the redefinition of nodal points the narrow band width of the stiffness matrix is destroyed and a greatly increased computational effort results in this model. Moreover, the lack of generality in crack orientation has made the discrete crack model unpopular. In spite of these shortcomings, the use of discrete crack models in finite element analysis offers certain advantages over other methods. For those problems that involve a few dominant cracks, the discrete crack approach offers a more realistic description of the cracks, which represent strain discontinuities in the structure. Such discontinuities are correctly characterized by the discrete crack model.

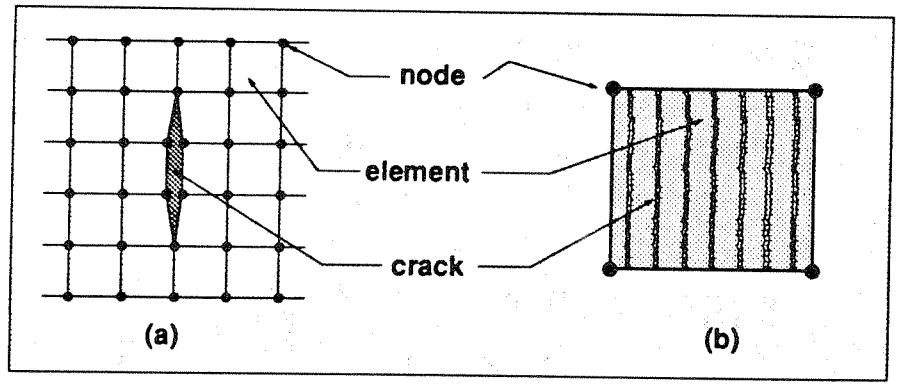

Fig. 2.7 Cracking Models: (a) Discrete Crack, (b) Smeared Crack

The need for a crack model that offers automatic generation of cracks and complete generality in crack orientation, without the need of redefining the finite element topology, has led the majority

of investigators to adopt the smeared crack model. Rather than representing a single crack, as shown in Fig. 2.7a, the smeared crack model represents many finely spaced cracks perpendicular to the principal stress direction, as illustrated in Fig. 2.7b. This approximation of cracking behavior of concrete is quite realistic, since the fracture behavior of concrete is very different from that of metals. In concrete fracture is preceded by microcracking of material in the fracture process zone, which manifests itself as strain softening. This zone is often very large relative to the cross section of the member due to the large size of aggregate (Fig. 2.8). In a steel member fracture is preceded by yielding of material in the process zone which is concentrated near the crack tip and has a relatively small size (Fig. 2.8). In this case a discrete crack model is a more realistic representation of actual behavior.

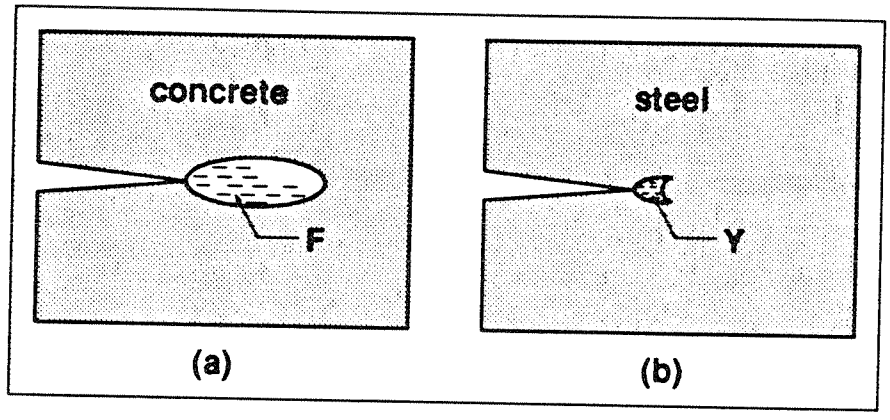

Fig. 2.8 ***Relative Size of Crack Process Zone***
(a) Fracture Zone (F) of Concrete
(b) Yielding Zone (Y) of Steel

The smeared crack model first used by Rashid (1968) represents cracked concrete as an elastic orthotropic material with reduced elastic modulus in the direction normal to the crack plane. With this continuum approach the local displacement discontinuities at cracks are distributed over some tributary area within the finite element and the behavior of cracked concrete can be represented by average stress-strain relations. In contrast to the discrete crack concept, the smeared crack concept fits the nature of the finite element displacement method, since the continuity of the displacement field remains intact.

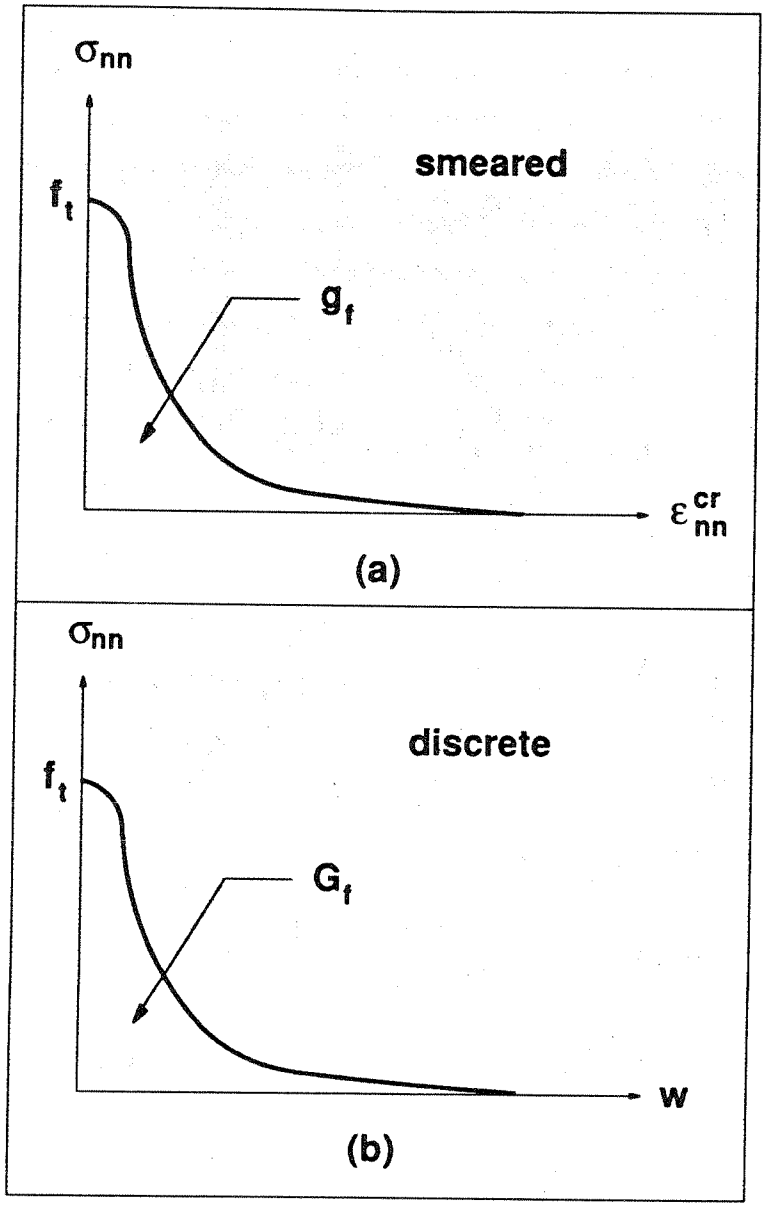

Fig. 2.9 *Strain Softening Behavior of Concrete*
(a) Tensile Stress vs. Crack Strain Relation
(b) Tensile Stress vs. Crack Opening Displacement Relation

Although this approach is simple to implement and is, therefore, widely used, it has nevertheless a major drawback, which is the dependency of the results on the size of the finite element mesh used in the analysis (Vebo and Ghali 1977; Bazant and Cedolin 1980). When large finite elements are used, each element has a large effect on the structural stiffness. When a single element cracks, the stiffness of the entire structure is greatly reduced. Higher order elements in which the material behavior is established at a number of integration points do not markedly change this situation, because, in

most cases, when a crack takes place at one integration point, the element stiffness is reduced enough so that a crack will occur at all other integration points of the element in the next iteration. Thus, a crack at an integration point does not relieve the rest of the material in the element, since the imposed strain continuity increases the strains at all other integration points. The overall effect is that the formation of a crack in a large element results in the softening of a large portion of the structure. The difficulty stems from the fact that a crack represents a strain discontinuity which cannot be modeled correctly within a single finite element in which the strain varies continuously. Many research efforts have been devoted to the solution of this problem based, in particular, on fracture mechanics concepts (Hillerborg et al. 1976; Bazant and Cedolin 1980, 1983).

The success fracture mechanics theory (Broek 1974) had in solving different types of cracking problems in metals, ceramics and rocks has lead to its use in the finite element analysis of reinforced concrete structures. If it is accepted that concrete is a notch-sensitive material, it can be assumed that a cracking criterion which is based on tensile strength may be dangerously unconservative and only fracture mechanics theory provides a more rational approach to the solution of the problem. In its current state of development, however, the practical applicability of fracture mechanics to reinforced concrete is still in question and much remains to be done. Intensive research in this area is presently undertaken by several researchers (Hillerborg et al. 1976; Bazant and Cedolin 1980, 1983; Jenq and Shah 1986).

In order to define the strain softening branch of the tensile stress-strain relation of concrete by fracture mechanics concepts three important parameters need to be defined: (1) the tensile strength of concrete at which a fracture zone initiates; (2) the area under the stress-strain curve; and (3) the shape of the descending branch (Reinhardt 1986). Among these parameters, the first two can be considered as material constants, while the shape of the descending branch varies in the models that have been proposed (Bazant and Oh 1983). Before discussing two of the most prominent models, a relation between the area under the tensile stress-crack strain diagram in Fig. 2.9a and the fracture energy G_f is needed. This relation can be readily derived by the following procedure.

The area g_f under the curve in Fig. 2.9a can be expressed as:

$$g_f = \int \sigma_{nn} \cdot d\varepsilon_{nn}^{cr} \tag{2.8}$$

The fracture energy G_f is defined as the amount of energy required to crack one unit of area of a continuous crack and is considered a material property. This definition results in the following expression for the fracture energy G_f

$$G_f = \int \sigma_{nn} \cdot dw \tag{2.9}$$

where w represents the sum of the opening displacements of all microcracks within the fracture zone. Eq. 2.9 is schematically shown in Fig. 2.9b.

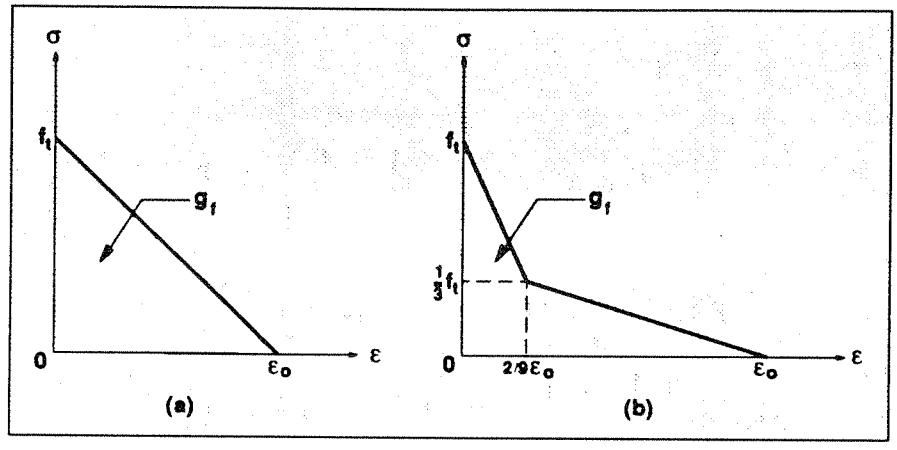

Fig. 2.10 *Typical Shapes of Softening Branch of Concrete*
(a) Bazant and Oh Model
(b) Hillerborg Model

In the smeared crack model w is represented by a crack strain which acts over a certain width within the finite element called the crack band width b. Since w is the accumulated crack strain, this is represented by the following relation

$$w = \int_b \varepsilon_{nn}^{cr} \cdot dn \tag{2.10}$$

Assuming that the microcracks are uniformly distributed across the crack band width, Eq. 2.10 reduces to:

$$w = b \cdot \varepsilon_{nn}^{cr} \tag{2.11}$$

The combination of Eq. 2.11 with Eqs. 2.8 and 2.9 yields the relation between g_f and G_f:

$$G_f = b \cdot g_f \tag{2.12}$$

The simplicity of Eq. 2.12 is misleading, because the actual size of the crack band width b depends on the selected element size, the element type, the element shape, the integration scheme and the problem type to be solved.

Two widely used models of the strain softening behavior of concrete in tension are those of Bazant and Hillerborg. Bazant and Oh (1983) introduced the "crack band theory" in the analysis of plain concrete panels. This model is one of the simplest fictitious crack models. The two basic assumptions of the model are that the width of the fracture zone w_c is equal to three times the maximum aggregate size (approximately 1 inch) and that the concrete strains are uniform within the band (Fig. 2.10a). In this case the final equation for determining the tensile fracture strain ε_o takes the form

$$\varepsilon_o = \frac{2 \cdot G_f}{f_t \cdot b} \tag{2.13}$$

where b is the element width and G_f is the fracture energy required to form a crack.

After an extensive experimental study Hillerborg et. al. (1976) proposed a bilinear descending branch for the tensile strain softening behavior of concrete (Fig. 2.10b). Using the assumption that the microcracks are uniformly distributed over the crack band width and combining the area g_f with the fracture energy G_f according to Eq. 2.12 the following equation is derived for the tensile fracture strain

$$\varepsilon_o = \frac{18}{5} \cdot \frac{G_f}{f_t \cdot b} \tag{2.14}$$

Both models have been extensively used in the analysis of RC members and yield very satisfactory results when the size of the finite element mesh is relatively small. The analytical results, however, differ significantly from the experimental data when the finite element mesh size becomes very large. This happens because both models assume a uniform distribution of microcracks over a significant portion of a relatively large finite element while the actual microcracks are concentrated in a much smaller cracked region of the element. Thus Eqs. 2.13 and 2.14 cannot be directly applied to the numerical analysis of RC structures with relatively large finite elements.

2.2.3.3 Proposed Model

Fracture and crack propagation in concrete depends to a large extent on the material properties in tension and the post-cracking behavior. Experimental studies (Welch and Haisman 1969; Bedard and Kotsovos 1986) indicate that the behavior of concrete after cracking is not completely brittle and that the cracked region exhibits some ductility. As the applied loads are increased the tensile stress

in the critical cross section of the member reaches the tensile strength f_t. At this stage microcracks develop and form a fracture zone. This process is characterized by the strain softening behavior of the section which ends when the microcracks coalesce to form one continuous macrocrack and stresses in the section reduce to zero.

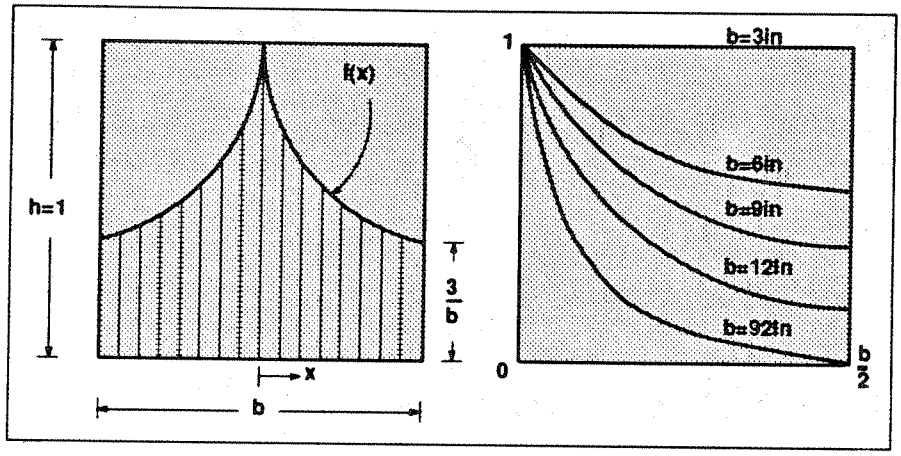

Fig. 2.11 Assumed Distribution of Microcracks in an Element

In order to account for the fact that microcracks are concentrated in a fracture process zone which may be small compared to the size of the finite element mesh a distribution function for the microcracks across the element width is introduced in this study. The distribution function is exponential, so that it can represent the concentration of microcracks near the crack tip when the finite element mesh size becomes fairly large (Fig. 2.11).

$$f(x) = \alpha \cdot e^{\beta x} \tag{2.15}$$

in which α and β are constants to be determined.

Using the boundary conditions that $f(0) = 1.0$ and $f(b/2) = 3/b$ into Eq. 2.10 yields the following equation for the distribution function

$$f(x) = e^{-2/b \cdot \ln b/3 \cdot x} \tag{2.16}$$

where b is the element width. The condition that $f(b/2) = 3/b$ ensures that, when the finite element mesh size is equal to 3 inches, i.e. three times the maximum aggregate size (Bazant and Oh 1983), the proposed distribution function reduces to Eq. 2.13 of the crack band theory. As shown in Fig. 2.12 the microcrack distribution $f(x)$ is uniform for a finite element mesh size smaller than 3 inches.

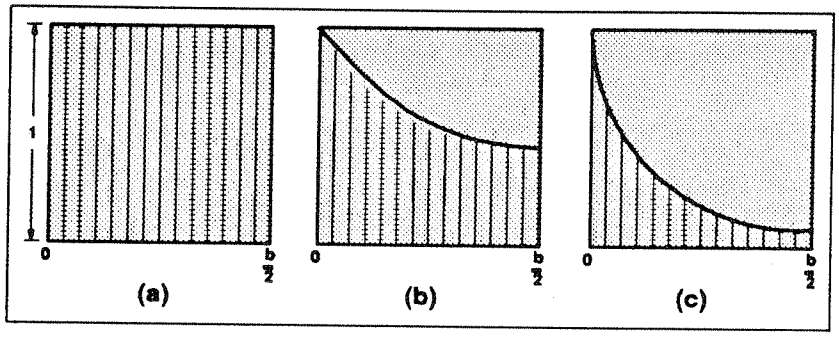

Fig. 2.12 Distribution Function of Microcracks Relative to Finite Element Mesh Size
(a) Small Finite Element Mesh Size
(b) Average Finite Element Mesh Size
(c) Large Finite Element Mesh Size

The fracture energy G_f is defined as the product of the area under the equivalent uniaxial stress-strain curve g_f and the fracture zone. It can, therefore, be expressed as:

$$G_f = \frac{1}{2}\varepsilon_o \cdot f_t \cdot 2 \cdot \int_0^{\frac{b}{2}} f(x)dx \qquad (2.17)$$

where f_t is the tensile strength of concrete, ε_o is the fracture tensile strain which characterizes the end of the strain softening process when the microcracks coalesce into a continuous crack and G_f is the fracture energy which is dissipated in the forming of a crack of unit length per unit thickness and is considered a material property.

The experimental study by Welch and Haisman (1969) indicates that for normal strength concrete the value of G_f/f_t is in the range of 0.005-0.01 mm. If G_f and f_t are known from measurements, then ε_o can be determined from

$$\varepsilon_o = \frac{G_f}{f_t \cdot \int_0^{\frac{b}{2}} f(x)dx} \tag{2.18}$$

After substituting the function $f(x)$ from Eq. 2.16 and integrating the following relation results

$$\varepsilon_o = \frac{2 \cdot G_f \cdot \ln(3/b)}{f_t \cdot (3-b)} \tag{2.19}$$

which clearly shows that ε_o depends on the finite element mesh size. This approach of defining ε_o renders the analytical solution insensitive to the mesh size and guarantees the objectivity of the results. At the same time this approach is capable of realistically representing the microcrack concentration near the tip of the crack in the case of large finite elements, in which case Eq. 2.13 yields unsatisfactory results. With this approach large finite elements can be used in the modeling of RC structures without loss of accuracy.

2.2.4 Concrete Material Matrix

In the analysis of reinforced concrete structures plane stress problems make up a large majority of practical cases. In the following the constitutive relation for plane stress problems is derived for the concrete model of this study.

For stress combinations inside the initial yield surface in Fig. 2.2 concrete is assumed to be a homogeneous, linear isotropic material. Thus, the stress-strain relation for plane stress problems has the simple form

$$\begin{Bmatrix} \sigma_x \\ \sigma_y \\ \tau_{xy} \end{Bmatrix} = \frac{E}{1-\nu^2} \cdot \begin{bmatrix} 1 & \nu & 0 \\ \nu & 1 & 0 \\ 0 & 0 & \frac{1-\nu}{2} \end{bmatrix} \cdot \begin{Bmatrix} \varepsilon_x \\ \varepsilon_y \\ \gamma_{xy} \end{Bmatrix} \tag{2.20}$$

where E is the initial elastic modulus of concrete and ν is Poisson's ratio.

Once the biaxial stress combination exceeds the initial yield surface in the compression-compression region of Fig. 2.2 concrete is assumed to behave as an orthotropic material. The same

assumption holds for stress combinations outside the ultimate loading surface indicating that the material has entered into the strain softening range. With reference to the principal axes of orthotropy the incremental constitutive relationship can be expressed (Desai and Siriwardance 1972; Chen 1976)

$$\begin{Bmatrix} d\sigma_1 \\ d\sigma_2 \\ d\tau_{12} \end{Bmatrix} = \frac{1}{1-\nu^2} \cdot \begin{bmatrix} E_1 & \nu\sqrt{E_1E_2} & 0 \\ \nu\sqrt{E_1E_2} & E_2 & 0 \\ 0 & 0 & (1-\nu^2)\cdot G \end{bmatrix} \cdot \begin{Bmatrix} d\varepsilon_1 \\ d\varepsilon_2 \\ d\gamma_{12} \end{Bmatrix} \tag{2.21}$$

where E_1 and E_2 are the secant moduli of elasticity in the direction of the axes of orthotropy which are oriented perpendicular and parallel to the crack direction, ν is Poisson's ratio and $(1-\nu^2)\cdot G = 0.25\cdot(E_1+E_2-2\nu\sqrt{E_1E_2})$

The main advantage of this model is its simplicity and ease of calibration with uniaxial concrete test data. Since the model is derived from the observation that the biaxial stress-strain relation is not very sensitive to the compression stress ratio, it is mainly applicable to plane stress problems such as beams, panels and thin shells where the stress field is predominantly biaxial. By contrast, it is well known from experimental evidence that hydrostatic pressure markedly influences the behavior of concrete under three-dimensional stress states.

The use of the incremental orthotropic model under general stress histories, in which the principal stress directions rotate during the loading process, has met with strong criticism, both, on physical and theoretical grounds. This aspect of the model does not, however, appear to affect its practical usefulness. The model was found capable of modeling satisfactorily the concrete behavior under cyclic as well as monotonic loads. This model and its adaptations have been applied to a wide variety of practical finite element problems with quite good agreement between theoretical and experimental results in most cases.

When the principal tensile strain exceeds ε_o in Fig. 2.4 a crack forms in a direction perpendicular to the principal strain. The stress normal to the crack is zero and the shear modulus needs to be reduced to account for the effect of cracking on shear transfer. In this case the incremental constitutive relation takes the form

$$\begin{Bmatrix} d\sigma_1 \\ d\sigma_2 \\ d\tau_{12} \end{Bmatrix} = \frac{1}{1-\nu^2} \cdot \begin{bmatrix} E_1 & 0 & 0 \\ 0 & 0 & 0 \\ 0 & 0 & \lambda(1-\nu^2)G \end{bmatrix} \cdot \begin{Bmatrix} d\varepsilon_1 \\ d\varepsilon_2 \\ d\gamma_{12} \end{Bmatrix} \tag{2.22}$$

where 1 and 2 are the directions parallel and perpendicular to the crack, respectively, and λ is a cracked shear constant.

The use of the cracked shear constant λ not only solves most of the numerical difficulties associated with a singular stiffness matrix, but also improves the representation of the concrete cracking phenomenon in finite element analysis. The shear factor may also be used as a way of suppressing the resulting singularity when all elements surrounding a particular node crack in the same direction. The value of λ has a lower bound, which is greater than zero and depends on the type of structure, the type of load and the accuracy of the numerical representation. The effect of dowel action of the reinforcement and the aggregate interlock tend to make the determination of an effective shear modulus rather complex. According to previous studies (ASCE 1982) a crack shear constant value of 0.5 was used in the analysis of shear panels and deep coupling beams, a value of 0.25 was used in the analysis of deep beams and a value of 0.125 in the analysis of shear walls and shear-wall frame systems. Hand, Pecknold and Schnobrich (1973) used a value of 0.4 in the analysis of RC plates and shells, Lin and Scordelis (1975) used a fixed value of 1.0 and Gilbert and Warner (1977) used a fixed value of 0.6 in their analysis of RC slabs. From these and other studies (Vebo and Ghali; Bashur and Darwin 1978; Barzegar and Schnobrich 1986) it appears that the value of λ is not critical to the accuracy of the final results. This fact is also corroborated by sensitivity analyses which are presented in Chapter 4, where it is shown that the value of the cracked shear constant does not affect the response of beams in bending. The cracked shear value λ in Eq. 2.22 is, consequently, fixed in the present study at a value of 0.4.

The use of the orthotropic constitutive relation in Eq. 2.21 to represent cracked concrete may not be totally realistic. In the case of a real crack the crack surface is rough and any sliding parallel to the crack will generate some local stresses or movement normal to the crack. To properly represent this type of behavior the off-diagonal terms of the material matrix which relate shear strain with normal stress should not be zero. The relative magnitude of these off-diagonal terms decreases as the crack widens. However, this effect may not be significant in a study which focuses attention on overall member behavior and most researchers have neglected it (Lin and Scordelis 1975; Bashur and Darwin 1978).

The proposed concrete model accounts for progressive cracking and changes in the crack direction by assuming that the crack is always normal to the principal strain direction. In contrast to the model used by Hand et. al. (1973) and Lin and Scordelis (1975), the material axes are not fixed after formation of the initial crack, but their orientation is determined from the direction of principal strains at the beginning of each iteration.

In developing a numerical algorithm for the rotating crack concept Gupta and Akbar (1983) obtained the rotating crack material matrix as the sum of the conventional fixed crack material matrix in Eq. 2.22 and a contribution which reflects the change in crack direction. This is expressed by the following Eq. 2.23

$$[D_{LO}]_c^* = [D_{LO}]_c + [G] \tag{2.23}$$

where $[D_{LO}]_c$ is given by Eq. 2.22 and $[G]$ reflects the change in the crack direction and is given by

$$[G] = -\frac{\sigma_1}{2\sqrt{\varepsilon_x - \varepsilon_y{}^2 + \gamma_{xy}^2}} \cdot \begin{bmatrix} \sin^2 2\theta & -\sin^2 2\theta & -\sin 2\theta \cos 2\theta \\ . & \sin^2 2\theta & \sin 2\theta \cos 2\theta \\ sym & . & \cos^2 2\theta \end{bmatrix} \tag{2.24}$$

While Eq. 2.24 is theoretically correct within the assumptions of the rotating crack model, any suitable incremental material stiffness matrix can be used in the context of an iterative nonlinear solution algorithm. It is, therefore, possible to neglect the rotating crack contribution $[G]$ provided that the change in crack direction is accounted for in the orientation of the material axes and in the transformation from material to element coordinate axes. Milford and Schnobrich (1984) found that neglecting the rotating crack contribution $[G]$ in Eq. 2.23 only rarely increased the number of iterations and did not introduce any numerical instabilities.

Since the material matrix is defined with reference to crack (principal strain) directions, it must be transformed to the global coordinate system before all element stiffness matrices can be assembled. This is accomplished by the following transformation.

$$[D_{GL}]_c = [T]^T \cdot [D_{LO}]_c \cdot [T] \tag{2.25}$$

where

$$[T] = \begin{bmatrix} \cos^2\theta & \sin^2\theta & \sin\theta\cos\theta \\ \sin^2\theta & \cos^2\theta & -\sin\theta\cos\theta \\ -2\sin\theta\cos\theta & 2\sin\theta\cos\theta & \cos^2\theta - \sin^2\theta \end{bmatrix} \tag{2.26}$$

and

$$\tan 2\theta = \frac{\gamma_{xy}}{\varepsilon_x - \varepsilon_y} \tag{2.27}$$

θ is the angle between the direction normal to the crack and the global x-axis.

During the state determination process the location of the present state in the biaxial principal stress and strain space needs to be determined. In this phase of the solution process the principal strains and stresses are obtained from the strains and stresses in the global coordinate system by the following relationships (Chia 1978):

$$\begin{Bmatrix} \varepsilon_1 \\ \varepsilon_2 \end{Bmatrix} = \begin{bmatrix} \cos^2\theta & \sin^2\theta & \sin\theta\cos\theta \\ \sin^2\theta & \cos^2\theta & -\sin\theta\cos\theta \end{bmatrix} \cdot \begin{Bmatrix} \varepsilon_x \\ \varepsilon_y \\ \gamma_{xy} \end{Bmatrix} \tag{2.28}$$

$$\begin{Bmatrix} \sigma_1 \\ \sigma_2 \end{Bmatrix} = \begin{bmatrix} \cos^2\theta & \sin^2\theta & 2\sin\theta\cos\theta \\ \sin^2\theta & \cos^2\theta & -2\sin\theta\cos\theta \end{bmatrix} \cdot \begin{Bmatrix} \sigma_x \\ \sigma_y \\ \tau_{xy} \end{Bmatrix} \tag{2.29}$$

2.3 Reinforcing Steel

2.3.1 Behavior of Reinforcing Steel

The properties of reinforcing steel, unlike concrete, are generally not dependent on environmental conditions or time. Thus, the specification of a single stress-strain relation is sufficient to define the material properties needed in the analysis of reinforced concrete structures.

Typical stress-strain curves for reinforcing steel bars used in concrete construction are obtained from coupon tests of bars loaded monotonically in tension. For all practical purposes steel exhibits the same stress-strain curve in compression as in tension. The steel stress-strain relation exhibits an initial linear elastic portion, a yield plateau, a strain-hardening range in which stress again increases with strain and, finally, a range in which the stress drops off until fracture occurs. The extent of the yield plateau is a function of the tensile strength of steel. High-strength, high-carbon steels, generally, have a much shorter yield plateau than relatively low-strength, low-carbon steels.

Since steel reinforcement is used in concrete construction in the form of reinforcing bars or wire, it is not necessary to introduce the complexities of three-dimensional constitutive relations for steel. For computational convenience it even often suffices to idealize the one dimensional stress-strain relation for steel. Three different idealizations, shown in Fig. 2.13, are commonly used depending on the desired level of accuracy (ASCE 1982; Cervenka et al. 1990).

The first idealization neglects the strength increase due to strain hardening and the reinforcing steel is modeled as a linear, perfectly plastic material, as shown in Fig. 2.13a. This assumption

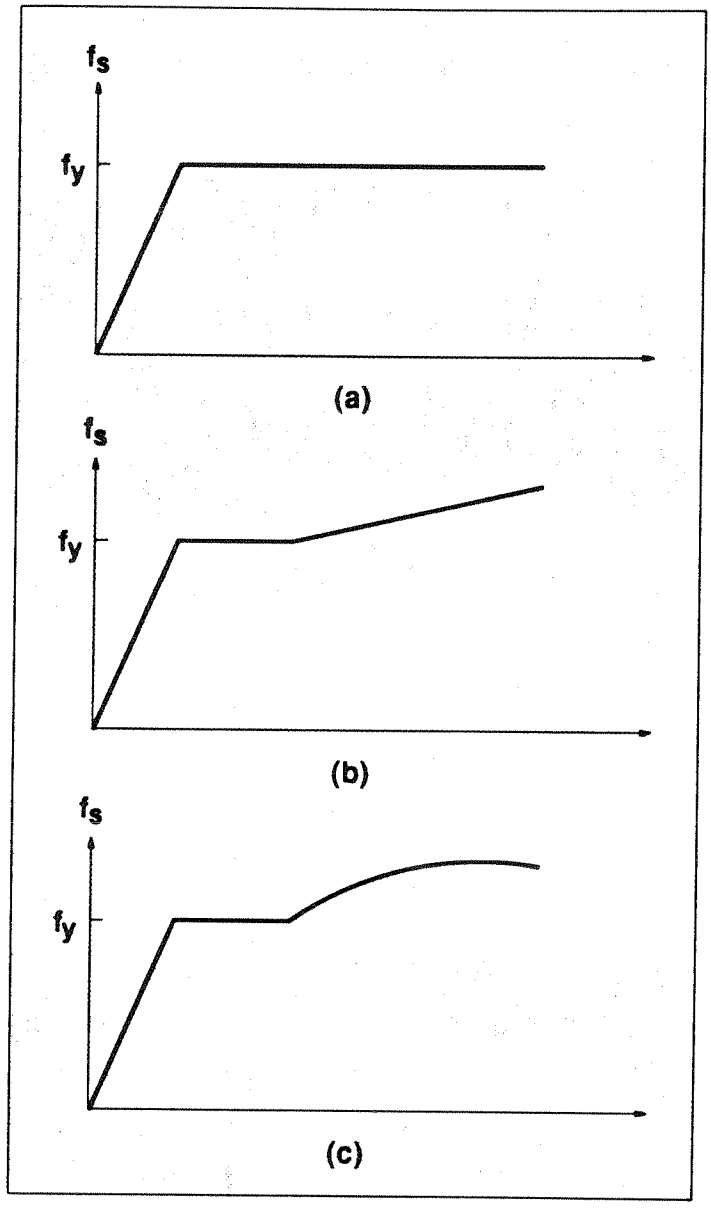

Fig. 2.13 Idealization of Steel Stress-Strain Relation

underlies the design equations of the ACI code. If the strain at the onset of strain hardening is much larger than the yield strain, this approximation yields very satisfactory results. This is the case for low-carbon steels with low yield strength.

If the steel hardens soon after the onset of yielding, this approximation underestimates the steel stress at high strains. In several instances it is necessary to evaluate the steel stress at strains higher than yield to more accurately assess the strength of members at large deformations. This is, particularly, true in seismic design, where assessing the available ductility of a member requires that

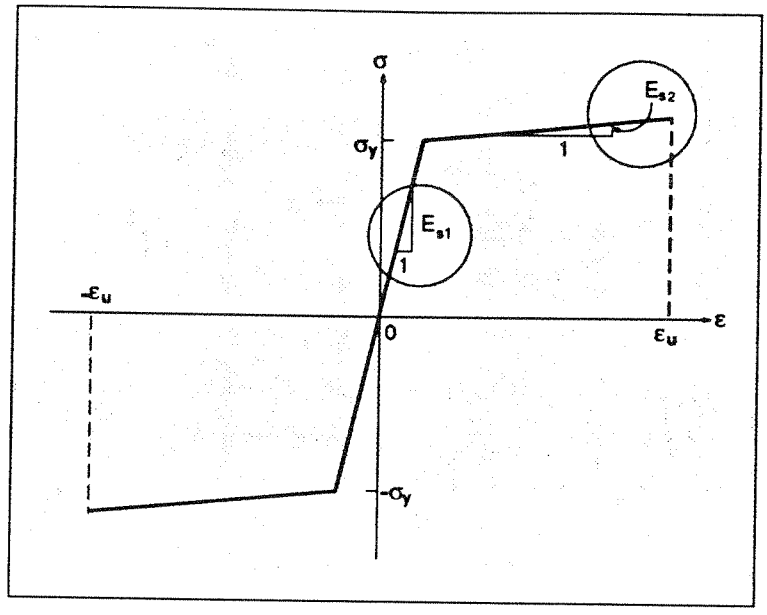

Fig. 2.14 Steel Stress-Strain Relation

the behavior be investigated under strains many times the yield strain. In this case more accurate idealizations which account for the strain hardening effect are required, as shown in Figs. 2.13b and 2.13c. The parameters of these models are the stress and strain at the onset of yield, the strain at the onset of strain hardening and the stress and strain at ultimate. These parameters can be derived from experimentally obtained stress-strain curves.

In this study the reinforcing steel is modeled as a linear elastic, linear strain hardening material with yield stress σ_y. The model is shown in Fig. 2.14. The reasons for this approximation are: (1) the computational convenience of the model; (2) the behavior of RC members is greatly affected by the yielding of reinforcing steel when the structure is subjected to monotonic bending moments. Yielding is accompanied by a sudden increase in the deformation of the member. In this case the use of the elastic-perfectly plastic model in Fig. 2.13a leads to numerical convergence problems near the ultimate member strength. It is, therefore, advisable to take advantage of the strain-hardening behavior of steel in improving the numerical stability of the solution. The assumption of a linear strain hardening behavior immediately after yielding of the reinforcement does not adversely affect the accuracy of the results, as long as the slope of the strain hardening branch is determined so that the strain energy of the model is equal to the strain energy of the experimental steel stress-strain relation (Fig. 2.14). Such a model has been successfully used in many analyses of reinforced concrete structures (Ngo and Scordelis 1967; Vebo and Ghali 1977; Bashur and Darwin 1978).

2.3.2 Steel Material Matrix

Three different approaches can be used in the modeling of reinforcing steel in a reinforced concrete structure: (1) the distributed or smeared model; (2) the embedded model; and (3) the discrete model (ASCE 1982).

In the distributed model the reinforcing steel is assumed to be distributed over the concrete element at a certain orientation angle θ. A composite concrete-steel constitutive relation is used in this case, which, however, requires that perfect bond be assumed between concrete and steel.

An embedded steel model is useful in connection with higher order isoparametric concrete elements. The reinforcing steel is considered as an axial member built into the isoparametric element such that its displacements are consistent with those of the element. Such a model again implies perfect bond between concrete and steel.

The most widely used model represents the reinforcement with discrete one-dimensional truss elements, which are assumed to be pin connected and possess two degrees of freedom at each node. Alternatively, beam elements can also be used, in which case, three degrees of freedom are allowed at each end of the bar element. In either case the one-dimensional reinforcing bar elements can be easily superimposed on the two-dimensional concrete element mesh. A significant advantage of the discrete representation, in addition to its simplicity, is that it can include the slip of reinforcing steel with respect to the surrounding concrete (Cervenka et al. 1990).

In this study a new discrete reinforcing steel model is used in the analysis of plane stress problems. The model is embedded in the concrete element, but includes the effect of bond-slip. In the analysis of slabs, where the effect of bond-slip is excluded from the model, it is computationally convenient to use the distributed model, in which the reinforcing mesh can be represented by an equivalent steel layer, as will be described later.

In the proposed discrete model the reinforcing steel is represented by a one-dimensional truss element which is embedded in the concrete element, as shown in Fig. 2.15. The nodes of the steel element do not need to coincide with the nodes of the concrete element. In this section the end displacements of the steel element are assumed to be compatible with the boundary displacements of the concrete element, so that perfect bond is implied. The discrete embedded steel element is then extended to include the effect of bond-slip between reinforcing steel and concrete in Section 2.5.

Even though the end displacements of the steel element are compatible with the concrete displacements, displacement compatibility within the concrete element is, generally, not satisfied when the two node steel element is embedded in the 8-node serendipity element. This fact, however, does not seem to affect the accuracy of results of the global behavior of RC structures.

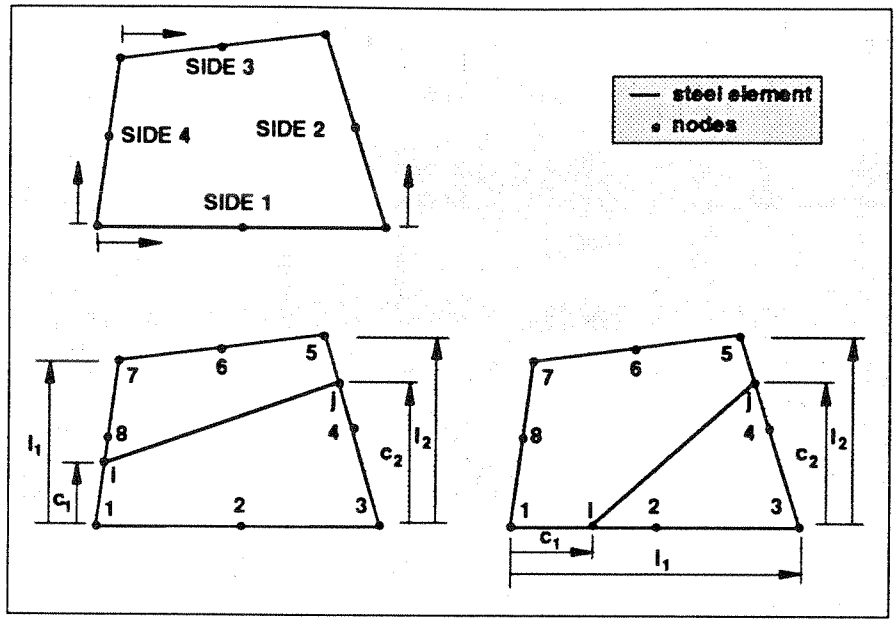

Fig. 2.15 Steel Element Embedded in Concrete Element

For the one-dimensional truss element with constant strain the stiffness matrix is given by

$$\begin{Bmatrix} P_1 \\ P_2 \end{Bmatrix} = \frac{AE}{L} \cdot \begin{bmatrix} 1 & -1 \\ -1 & 1 \end{bmatrix} \cdot \begin{Bmatrix} d_1 \\ d_2 \end{Bmatrix} \tag{2.30}$$

or

$$\{P\} = [K_{LO}]_s \cdot \{d\} \tag{2.31}$$

where E is the modulus of elasticity, A the cross-sectional area and L the length of the bar element. P_1 and P_2 are axial end forces and d_1 and d_2 are axial end displacements of the reinforcing bar. E is equal to E_{s1} before yielding of the reinforcement and equal to E_{s2} after yielding (Fig. 2.14). $[K_{LO}]$ denotes the local stiffness matrix of the axially loaded reinforcing bar.

Eq. 2.31 can also be expressed relative to the global coordinate system by applying a rotation with angle θ, which is the angle between the axis of the reinforcing bar and the global x-axis of the structure. This can be formally expressed by the following relation:

$$\begin{Bmatrix} P_{1x} \\ P_{1y} \\ P_{2x} \\ P_{2y} \end{Bmatrix} = [T_1]^T \cdot [K_{LO}]_s \cdot [T_1] \cdot \begin{Bmatrix} d_{1x} \\ d_{1y} \\ d_{2x} \\ d_{2y} \end{Bmatrix} \tag{2.32}$$

where

$$[T_1]=\begin{bmatrix}\cos\theta & \sin\theta & 0 & 0\\ 0 & 0 & \cos\theta & \sin\theta\end{bmatrix} \tag{2.33}$$

1 and 2 refer to the end points of the steel element and the subscripts x and y indicate that steel forces and displacements are defined with reference to the global coordinate system of the structure.

Since the end points of the reinforcing bar element do not generally coincide with the nodes of the concrete element in Fig. 2.15, Eq. 2.32 has to undergo another transformation before it can be assembled together with the concrete element stiffness matrix. This can be formally expressed by the following relation:

$$[K_{GL}]_s=[T_2]^T\cdot[T_1]^T\cdot[K_{LO}]_s\cdot[T_1]\cdot[T_2] \tag{2.34}$$

Transformation matrix $[T_2]$ can be derived with the procedure used to establish the consistent nodal forces of the finite element method. The consistent nodal forces for node i are:

$$P_\xi=\int_{-1}^{1}N_i\cdot\left(P_t\frac{\partial x}{\partial\xi}-P_n\frac{\partial y}{\partial\xi}\right)d\xi \tag{2.35}$$

$$P_{yi}=\int_{-1}^{1}N_i\cdot\left(P_n\frac{\partial x}{\partial\xi}-P_t\frac{\partial y}{\partial\xi}\right)d\xi \tag{2.36}$$

where N_i is the shape function for node i and P_n, P_t are the normal and tangential boundary loads, respectively. If a concentrated load acts at a point $\xi=\delta_i$, Eqs. 2.35 and 2.36 reduce to the following:

$$P_\xi=N_i(\delta_i)\cdot P_x \tag{2.37}$$

$$P_{yi}=N_i(\delta_i)\cdot P_y \tag{2.38}$$

When the 8-node isoparametric element is used in the two-dimensional mesh representation of the member, the shape functions for nodes i, j and k in Fig. 2.16 are:

$$N_i=\frac{1}{2}\xi\cdot(\xi-1) \tag{2.39}$$

$$N_j=(1-\xi)\cdot(1+\xi) \tag{2.40}$$

$$N_k=\frac{1}{2}\xi\cdot(\xi+1) \tag{2.41}$$

To obtain $N_i(\delta_i)$ in Eqs. 2.37 and 2.38 $\delta_i = (2c_i/l_i - 1)$ is substituted for ξ in Eqs. 2.39-2.41 where c_i characterizes the position of the steel node relative to the concrete element boundary, as shown in Figs. 2.15 and 2.16. By setting $c_i/l_i = r_i$ Eqs. 2.39-2.41 simplify to the following relations which are used to construct the transformation matrix $[T_2]$.

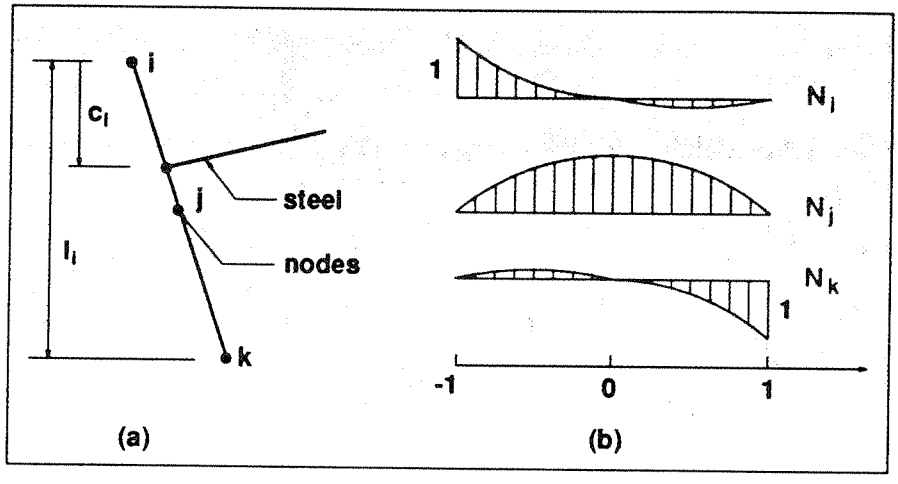

Fig. 2.16 ***Parameters and Shape Functions of Isoparametric Concrete and Embedded Steel Element***

$$N_i = (r_i - 1) \cdot (2r_i - 1) \tag{2.42}$$

$$N_j = 4r_i \cdot (1 - r_i) \tag{2.43}$$

$$N_k = r_i \cdot (2r_i - 1) \tag{2.44}$$

If the reinforcing bar element crosses the concrete element boundary on sides 2 and 4 in Fig. 2.15, nodes i, j and k correspond to node numbers 1, 8 and 7, on side 4, and node numbers 3, 4 and 5 on side 2, respectively. With the notation of Fig. 2.15 the transformation matrix $[T_2]$ has the following form:

$$[T_2] = \begin{bmatrix} \mathbf{A}_1 & \mathbf{0} & \mathbf{0} & \mathbf{0} & \mathbf{0} & \mathbf{0} & \mathbf{A}_3 & \mathbf{A}_2 \\ \mathbf{0} & \mathbf{0} & \mathbf{B}_1 & \mathbf{B}_2 & \mathbf{B}_3 & \mathbf{0} & \mathbf{0} & \mathbf{0} \end{bmatrix} \tag{2.45}$$

where

$$\mathbf{A}_1=\begin{bmatrix}2p^2-3p+1 & 0\\ 0 & 2p^2-3p+1\end{bmatrix}\quad \mathbf{A}_2=\begin{bmatrix}-4p^2+4p & 0\\ 0 & -4p^2+4p\end{bmatrix}\quad \mathbf{A}_3=\begin{bmatrix}2p^2-p & 0\\ 0 & 2p^2-p\end{bmatrix} \tag{2.46}$$

$$\mathbf{B}_1=\begin{bmatrix}2q^2-3q+1 & 0\\ 0 & 2q^2-3q+1\end{bmatrix}\quad \mathbf{B}_2=\begin{bmatrix}-4q^2+4q & 0\\ 0 & -4q^2+4q\end{bmatrix}\quad \mathbf{B}_3=\begin{bmatrix}2q^2-q & 0\\ 0 & 2q^2-q\end{bmatrix} \tag{2.47}$$

$p = c_1/l_1$, $q = c_2/l_2$ and $\mathbf{0}$ is the 2x2 null matrix.

In Eq. 2.45 the position of submatrices **A** and **B** within the transformation matrix $[T_2]$ is related to the side of the concrete element which the reinforcing bar element crosses. If the reinforcing bar element crosses the concrete element boundary on sides 1 and 2 in Fig. 2.15, the transformation matrix $[T_2]$ takes the form

$$[T_2]=\begin{bmatrix}\mathbf{A}_1 & \mathbf{A}_2 & \mathbf{A}_3 & \mathbf{0} & \mathbf{0} & \mathbf{0} & \mathbf{0} & \mathbf{0}\\ \mathbf{0} & \mathbf{0} & \mathbf{B}_1 & \mathbf{B}_2 & \mathbf{B}_3 & \mathbf{0} & \mathbf{0} & \mathbf{0}\end{bmatrix} \tag{2.48}$$

noting that the submatrices **A** and **B** are the same as before, but c_1 is now defined, as shown on the right hand side of Fig. 2.15.

When the 4-node isoparametric element is used in the two-dimensional mesh representation of the member, the shape functions for nodes i, and k change and the transformation matrix $[T_2]$ simplifies considerably. For example, if the reinforcing bar element crosses the concrete element boundary on sides 2 and 4 in Fig. 2.15, the transformation matrix $[T_2]$ takes the form

$$[T_2]=\begin{bmatrix}1-p & 0 & 0 & 0 & 0 & 0 & p & 0\\ 0 & 1-p & 0 & 0 & 0 & 0 & 0 & p\\ 0 & 0 & 1-q & 0 & q & 0 & 0 & 0\\ 0 & 0 & 0 & 1-q & 0 & q & 0 & 0\end{bmatrix} \tag{2.49}$$

where p and q are defined as in Eqs. 2.46 and 2.47.

The steel stiffness matrix $[K_{GL}]_s$ in Eq. 2.34 can now be assembled together with the concrete element stiffness matrix to form the total stiffness of the structure.

In the analysis of slabs with the layer model the effect of bond-slip is not taken into account. In this case it is computationally convenient to use the distributed steel model. In this model the reinforcing bars inside a concrete element are replaced by an equivalent steel element with distributed uniaxial material properties in each reinforcing direction. The equivalent steel element has the dimensions of the concrete element and thickness t_s which is determined from the following relation:

$$t_s = \frac{A_s}{b} = \rho_s \cdot d_e \tag{2.50}$$

where A_s is the cross sectional area of one reinforcing bar in the particular direction, b is the spacing of reinforcing bars, ρ_s is the reinforcing ratio and d_e is the effective depth of the member.

Since the equivalent steel element has uniaxial properties in the direction parallel to the axis of the reinforcing bars, the constitutive material model takes the simple form

$$\begin{Bmatrix} \sigma_1 \\ \sigma_2 \\ \tau_{12} \end{Bmatrix} = \begin{bmatrix} E_{s1} & 0 & 0 \\ 0 & 0 & 0 \\ 0 & 0 & 0 \end{bmatrix} \cdot \begin{Bmatrix} \varepsilon_1 \\ \varepsilon_2 \\ \gamma_{12} \end{Bmatrix} \tag{2.51}$$

where E_{s1} is Young's modulus of reinforcing steel. E_{s1} in Eq. 2.51 is replaced by the strain hardening modulus E_{s2}, when the reinforcing steel yields.

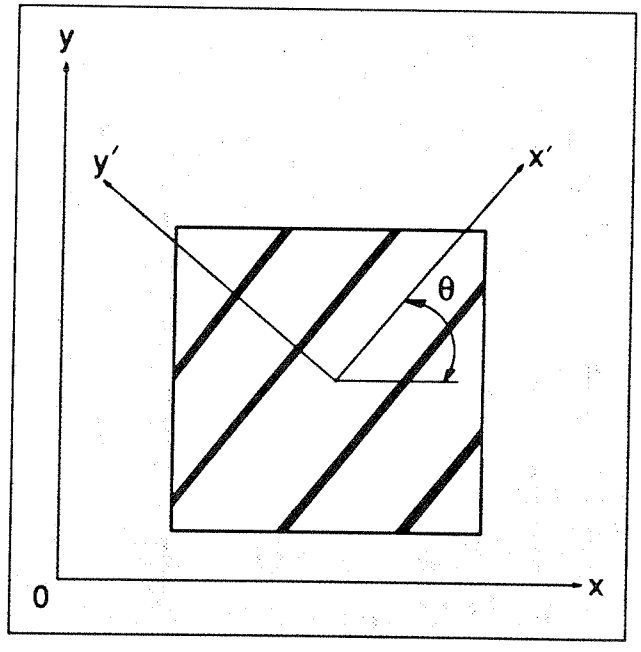

Fig. 2.17 Coordinate Transformation for Steel

The local stiffness matrix in Eq. 2.51 needs to be transformed to the global x-y coordinate system before it can be assembled into the structure stiffness matrix. This is accomplished exactly as in Eqs. 2.25 and 2.26 for concrete, where θ now represents the angle between the axis of the reinforcing bars and the global x-axis (Fig. 2.17).

2.4 Bond between Reinforcing Steel and Concrete

2.4.1 Bond Behavior

Bond is the interaction between reinforcing steel and surrounding concrete. The force transfer from steel to concrete can be attributed to three different phenomena: (1) chemical adhesion between mortar paste and bar surface; (2) friction and wedging action of small dislodged sand particles between the bar and the surrounding concrete; and (3) mechanical interaction between concrete and steel. Bond of plain bars derives primarily from the first two mechanisms, even though there is some mechanical interlocking caused by the roughness of the bar surface. Deformed bars have better bond than plain bars, because most of the steel force is transferred through the lugs to concrete. Friction and chemical adhesion forces are not negligible, but secondary and tend to decrease as the reinforcing bars start to slip.

Since bond stresses in reinforced concrete members arise from the change in the steel force along the length, the effect of bond becomes more pronounced at end anchorages of reinforcing bars and in the vicinity of cracks.

In the simplified analysis of reinforced concrete structures complete compatibility of strains between concrete and steel is usually assumed, which implies perfect bond. This assumption is realistic only in regions where negligible stress transfer between the two components takes place. In regions of high transfer stresses along the interface between reinforcing steel and surrounding concrete, such as near cracks, the bond stress is related to the relative displacement between reinforcing steel and concrete. The assumption of perfect bond near crack zones requires infinitely high strains to explain the existence of a finite crack width. In reality there is no strain compatibility between reinforcing steel and surrounding concrete near cracks. This incompatibility and the crack propagation give rise to relative displacements between steel and concrete, which are known as bond-slip.

Two types of experiments are used in the determination of the bond stress-slip relation. In an anchorage test, such as the standard ASTM pull-out test, the force is applied at the projecting end of a bar which is embedded in a concrete cylinder. This force is gradually transferred to the concrete. In the transfer test a self-equilibrating pair of forces are applied at the two ends of a bar projecting from a concentrically cast concrete block or cylinder. Tests of this type are intended to simulate conditions in the tension zone of a concrete beam between primary flexural cracks.

In either type of test the bond stress is determined from the change in steel stress over a certain measurement length, which is usually taken equal to five bar diameters, and the relative slip is determined externally or internally. It is, therefore, practically impossible to establish a "local" bond

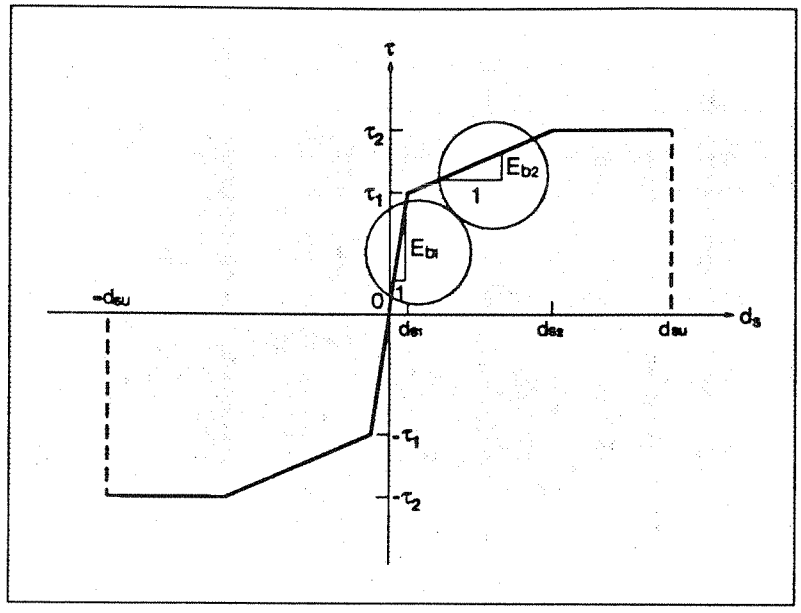

Fig. 2.18 Bond Stress-Slip Relation for Plane Stress Problems

stress-slip relation, since the measured bond stress-slip relation generally represents an average over the measurement length. Moreover, since the bond stress is derived from the change in steel stress, the result is very sensitive to experimental error. The bond-slip relation also depends on the position of the bars, the bar surface conditions, the loading state, the boundary conditions and the anchorage length of bars. In spite of these difficulties, several experimental bond-stress slip relations have been proposed (ASCE 1982; Eligehausen et al. 1983; Hayashi and Kokusho 1985).

In this study the simple trilinear bond stress-slip model in Fig. 2.18 is adopted in the finite element analysis of plane stress problems. The parameters of the model are derived from the material properties of each specimen in the correlation studies of Chapter 4. This model is a good approximation of the actual behavior in cases, which do not exhibit significant bond-slip and associated bond damage. Under monotonic loading this holds true in all RC members which do not experience anchorage failure.

Since it is the objective of this study to investigate the bond-slip behavior of reinforcing steel in more detail, a more sophisticated bond-slip model is used in the correlation studies of anchored reinforcing bars under monotonic and cyclic loading in Chapter 4. A brief description of this model follows, while more details are given elsewhere (Eligehausen et al. 1983; Zulfiqar and Filippou 1990).

The bond stress-slip relation between reinforcing bars and surrounding concrete consists of the following parts:

1. Two monotonic envelopes, one in tension and one in compression, which are updated at each slip reversal to reflect incurred damage (curves (a) and (b) in Fig. 2.19).

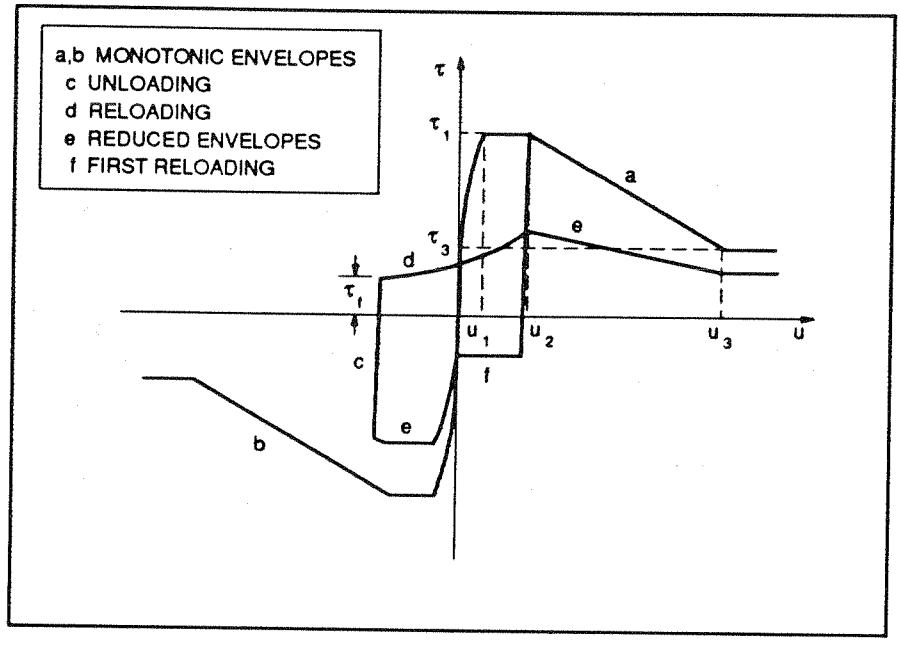

Fig. 2.19 Bond Stress-Slip Relation for Anchorage Problems

2. A typical unloading-reloading path described by the unloading curve (c), the current frictional bond resistance τ_f and a reloading curve (d), along with a set of rules for unloading and reloading for incomplete cycles (Fig. 2.19).

3. A set of relations for updating the monotonic envelope values and the frictional bond resistance as a function of incurred damage.

The monotonic envelope consists of an initial nonlinear relation $\tau = \tau_1(u/u_1)^\alpha$, valid for $u \le u_1$, followed by a plateau $\tau = \tau_1$ for $u_1 \le u \le u_2$. For $u \ge u_2$, τ decreases linearly to the value of ultimate frictional bond resistance τ_3 at a slip value of u_3 which is assumed to be equal to the clear distance between the lugs of deformed bars.

When the load is reversed at some slip value, unloading takes place along a steep straight line until the frictional bond resistance τ_f is reached (curve c Fig. 2.19).

The reloading curve is described by a fourth degree polynomial (curve *d* in Fig. 2.19) starting from the frictional bond resistance value and leading to the intersection between reduced envelope and previous unloading curve. In case that no slip has been previously imposed in the same loading direction, reloading takes place along a horizontal line until reaching the reduced envelope (curve *f* in Fig. 2.19).

During each half cycle following the first unloading, the monotonic envelopes are updated (curve e Fig. 2.19) by reducing the characteristic bond stress values τ_1 and τ_3 by a factor, which is a function of the "damage parameter" d. The damage parameter has the form (Eligehausen et al. 1983)

$$\tau_1(N) = \tau_1(1-d) \tag{2.52}$$

where τ_1 is the characteristic value of the virgin envelope curve and $\tau_1(N)$ is the corresponding value after N cycles. The damage parameter depends on the total energy dissipated by the bond-slip process and is given by

$$d = 1 - e^{-1.2(E/E_0)^{1.1}} \tag{2.53}$$

where E is the total dissipated energy. E_0 is the energy absorbed under monotonically increasing slip up to the value u_3 and is used as a normalization parameter.

The frictional bond resistance τ_f depends on the maximum value of previous slip u_{max} in either direction of loading and the ultimate bond resistance $\tau_3(N)$ of the corresponding reduced envelope curve. If cyclic reversals are performed under fixed values of slip, τ_f is further reduced by multiplying its initial value with a factor which depends on the energy dissipated by friction alone. Explicit expressions for these relations are presented by Eligehausen et al. (1983).

In the nonlinear bond stress-slip model all expressions are cast in dimensionless form except for the characteristic values of the monotonic envelope curve. The model can thus be readily extended to describe the local bond stress-slip relation of reinforcing bars under different bond and loading conditions by only changing the characteristic values of the monotonic envelope curve. These characteristic values depend on several parameters such as bar diameter, concrete strength, bar deformation pattern, clear spacing between bars and transverse pressure due to loading or confinement. Ideally, the characteristic values should be derived from experiments which simulate the actual geometric and loading conditions of the structure under investigation. In the absence of experimental data the characteristic values of the envelope curve can be derived from the material properties of the structure based on recommendations of Eligehausen et al. (1983).

2.4.2 Bond Stiffness Matrix

Two basically different elements have been proposed to date for including the bond-slip effect in the finite element analysis of RC structures. The first is the bond link element by Ngo and Scordelis (1967) shown in Fig. 2.20. It consists of two orthogonal springs which connect and transmit shear

and normal forces between a reinforcing steel node and an adjacent concrete node. Since the link element has no physical dimensions, the two connected nodes occupy the same location in the finite element mesh.

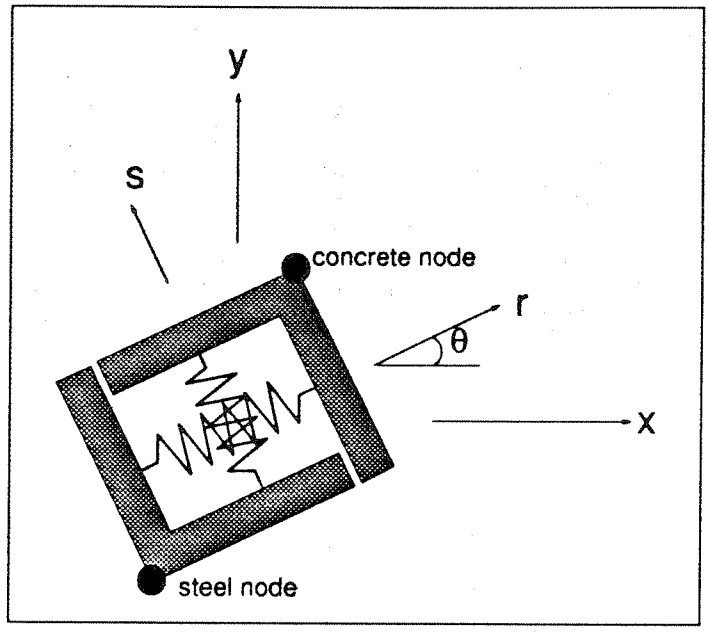

Fig. 2.20 Bond Link Element

The second bond-slip element, called the bond zone element, is significantly different from the bond link element, the most important difference being its finite dimension. In the bond zone element by de Groot et al. (1981) the contact surface between reinforcing steel and concrete and the concrete in the immediate vicinity of the reinforcing bar are modeled by a material law, which represents the special properties of the bond zone. In this model, which is shown in Fig. 2.21, the bond stress is the sum of the slip resistance and the stress due to mechanical interlocking and can be determined from

$$\tau = \tau_o + \tau_k = S \cdot \Delta u - k \cdot \sigma_r \tag{2.54}$$

where S is the slip modulus, Δu is the relative slip, k is the rib factor which represents the effect of the bar deformations and σ_r is the radial stress.

The contact element describes the behavior of the layer between reinforcing steel and concrete and provides a continuous connection between the reinforcing steel and the surrounding concrete element, if a linear or higher order displacement field is used in the discretization scheme. A simpler but similar element was proposed by Keuser and Mehlhorn (1987). They introduced higher order displacement interpolation functions and showed through energy considerations that the bond link

element cannot adequately represent the stiffness of the steel-concrete interface. Finally, Yankelevsky (1985) derived closed form solutions of the stiffness matrix of a reinforcing bar element on the assumption that the steel remains linear elastic and the local bond-stress slip relation is approximated with a piecewise linear curve.

In studies where detailed local behavior is of interest, the continuous bond models are most appropriate. In cases, however, where the overall structural behavior is of primary interest, the bond link element provides a reasonable compromise between accuracy and computational efficiency. It is, therefore, selected for representing the bond-slip effect in this study.

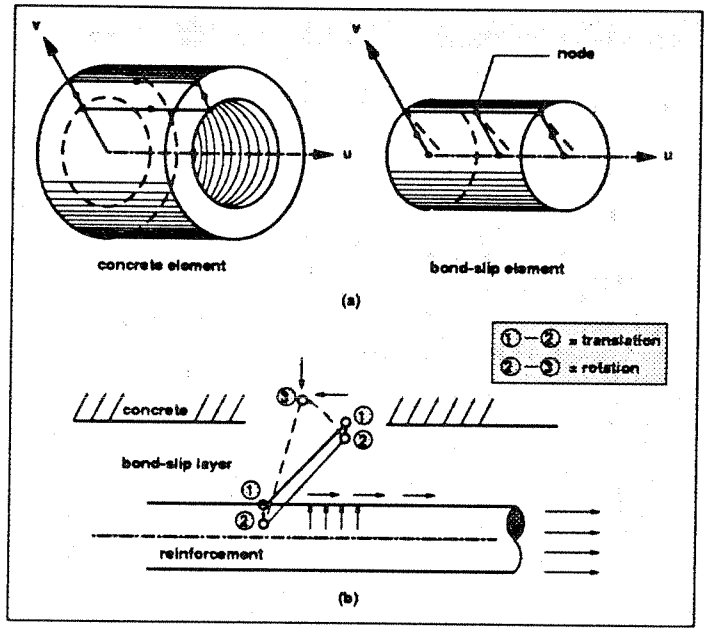

Fig. 2.21 Bond Zone Element

The element stiffness matrix relates shear and normal force to the corresponding nodal displacements by the following relation (ASCE 1982):

$$\begin{Bmatrix} F_r \\ F_s \end{Bmatrix} = \begin{bmatrix} K_r & 0 \\ 0 & K_s \end{bmatrix} \cdot \begin{Bmatrix} d_r \\ d_s \end{Bmatrix} \tag{2.55}$$

where K_r represents the stiffness due to dowel action and may be assigned a very low value, if dowel action is not accounted for. K_s is the shear stiffness of the interface and can be derived from the measured bond stress-slip relation according to the following equation

$$K_s = E_{bl} \cdot A \tag{2.56}$$

where E_{b1} is the initial slip modulus and is replaced by E_{b2} when the bond-slip d_s exceeds the value d_{s1} (Fig. 2.18). A is the bar circumferential area tributary to one bond link and is determined from the following relation:

$$A = \frac{m\pi d_b l}{2b} \tag{2.57}$$

where m is the number of bars of diameter d_b in the cross section of the member, l is the spacing of the bond links along the reinforcing bar and b is the width of the member cross section. The factor 2 appears in the denominator to account for the fact that it is usually convenient to place bond link elements at, both, the top and the bottom of the reinforcing bar element.

The local stiffness matrix of the bond link element in Eq. 2.55 is transformed to global coordinates by a rotation matrix. This can be expressed formally as

$$[K_{GL}]_B = [T]^T \cdot [K_{LO}]_B \cdot [T] \tag{2.58}$$

where

$$[K_{LO}]_B = \begin{bmatrix} K_r & 0 & -K_r & 0 \\ 0 & K_s & 0 & -K_s \\ -K_r & 0 & K_r & 0 \\ 0 & -K_s & 0 & K_s \end{bmatrix} \tag{2.59}$$

and

$$[T] = \begin{bmatrix} c & s & 0 & 0 \\ -s & c & 0 & 0 \\ 0 & 0 & c & s \\ 0 & 0 & -s & c \end{bmatrix} \tag{2.60}$$

with $c = \cos\theta$, $s = \sin\theta$ and θ as defined in Fig. 2.20.

The global bond link stiffness matrix in Eq. 2.59 takes the following explicit form

$$[K_{GL}]_B = \begin{bmatrix} K_r c^2 + K_s s^2 & K_r sc - K_s sc & -K_r c^2 - K_s s^2 & -K_r sc + K_s sc \\ & K_r s^2 + K_s c^2 & -K_r sc + K_s sc & -K_r s^2 - K_s c^2 \\ & & K_r c^2 + K_s s^2 & K_r sc - K_s sc \\ Sym. & & & K_r s^2 + K_s c^2 \end{bmatrix} \tag{2.61}$$

2.5 Discrete Reinforcing Steel Model with Bond-Slip

The bond link element connects one steel node with a corresponding concrete node which occupies the same physical location in the undeformed configuration of the structure. Consequently, the use of this element in the finite element analysis of RC structures imposes the following restrictions: (a) the finite element mesh must be arranged so, that a reinforcing bar is located along the edge of a concrete element and (b) a double node is required to represent the relative slip between reinforcing steel and concrete. These restrictions arise from the fact that the stiffness of the bond link element is associated with the relative displacement between steel and concrete. Consequently, the total displacement of both reinforcing steel and concrete is required at each node of the finite element mesh, so that the relative displacement and, consequently, the bond stress between steel and concrete can be determined. In a complex structure, particularly in the case of three-dimensional models, these requirements lead to a considerable increase in the number of degrees of freedom, not only because of the doubling of the number of nodes along the reinforcing steel bars, but also because the mesh has to be refined, so that the bars pass along the edges of concrete elements. The complexity of mesh definition and the large number of degrees of freedom has discouraged researchers from including the bond-slip effect in many studies to date.

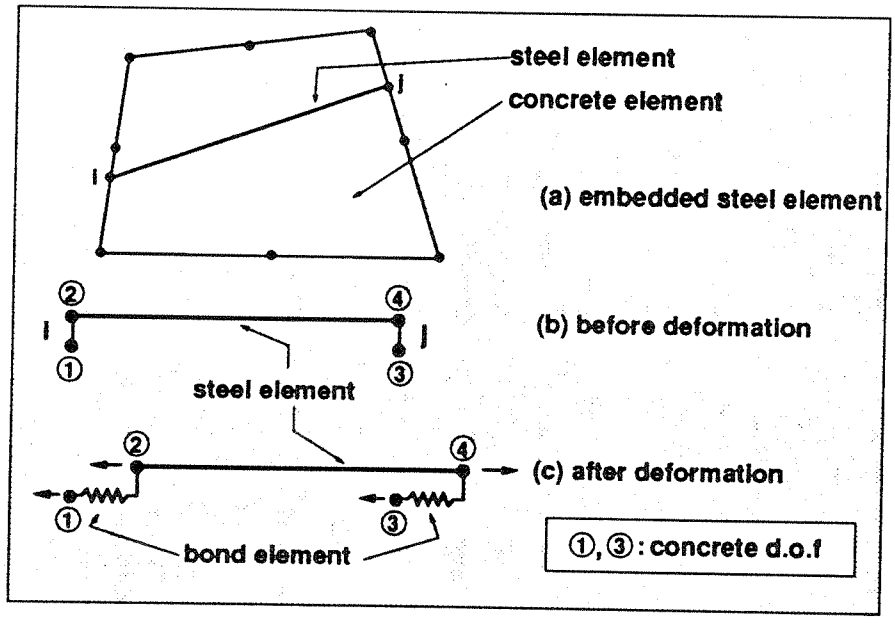

Fig. 2.22 Discrete Reinforcing Steel Element with Bond-Slip

To address some of these limitations of the bond link element a new discrete reinforcing steel model which includes the bond-slip deformation is proposed in this study. In this model the reinforcing bar is assumed to be embedded inside the concrete element, as shown in Fig. 2.22a, so that the analyst

can choose the finite element mesh configuration independently of the location of the reinforcing bars. At the same time the relative slip between reinforcing steel and concrete is explicitly taken into account in the model. Since the finite element model only includes the concrete displacement degrees of freedom, the degrees of freedom which are associated with the reinforcing steel need to be condensed out from the element stiffness matrix, before it is assembled into the structure stiffness matrix. A second pass, however, is now required in order to satisfy the equilibrium of each reinforcing bar and determine the steel forces. The formal derivation of this model is presented in the following, while the numerical implementation is deferred to Chapter 3.

A reinforcing steel element which is embedded in a concrete element is shown in Fig. 2.22a. A convenient free body diagram is selected which isolates the steel element with the bond link elements attached at its end points. Fig. 2.22b shows this element before and Fig. 2.22c after deformation. i and j denote the end points of the element, points 1 and 3 are associated with the concrete and points 2 and 4 are associated with the reinforcing steel at ends i and j, respectively. The corresponding degrees of freedom of the reinforcing steel and concrete at each end are connected by the bond link element whose stiffness depends on the relative displacement between steel and concrete. With this assumption the stiffness matrix which relates the end displacements along the axis of the reinforcing bar with the corresponding forces is given by

$$\begin{Bmatrix} P_1 \\ P_2 \\ P_3 \\ P_4 \end{Bmatrix} = \begin{bmatrix} k_{bi} & -k_{bi} & 0 & 0 \\ -k_{bi} & k_s + k_{bi} & 0 & -k_s \\ 0 & 0 & k_{bj} & -k_{bj} \\ 0 & -k_s & -k_{bj} & k_s + k_{bj} \end{bmatrix} \cdot \begin{Bmatrix} d_1 \\ d_2 \\ d_3 \\ d_4 \end{Bmatrix} \tag{2.62}$$

where $k_s = A \cdot E/L$ is the steel bar stiffness, k_b is the stiffness of the bond link parallel to the bar axis at the corresponding end of the steel element and the dowel action is neglected in Eq. 2.62 so that term k_r in Eq. 2.59 is equal to zero. In order to include the effect of dowel action Eq. 2.62 has to be expanded to a relation between eight displacement degrees of freedom and the corresponding forces. Since the following derivation procedure is not affected by this change, the dowel action is neglected here for the sake of simplicity.

By rearranging rows and columns in Eq. 2.62 the following relation results

$$\begin{Bmatrix} P_1 \\ P_3 \\ P_2 \\ P_4 \end{Bmatrix} = \begin{bmatrix} k_{bi} & 0 & -k_{bi} & 0 \\ 0 & k_{bj} & 0 & -k_{bj} \\ -k_{bi} & 0 & k_s + k_{bi} & -k_s \\ 0 & -k_{bj} & -k_s & k_s + k_{bj} \end{bmatrix} \cdot \begin{Bmatrix} d_1 \\ d_3 \\ d_2 \\ d_4 \end{Bmatrix} \tag{2.63}$$

or

$$\begin{Bmatrix} \mathbf{P}_c \\ \mathbf{P}_s \end{Bmatrix} = \begin{bmatrix} \mathbf{K}_{cc} & \mathbf{K}_{cs} \\ \mathbf{K}_{cs} & \mathbf{K}_{ss} \end{bmatrix} \cdot \begin{Bmatrix} \mathbf{d}_c \\ \mathbf{d}_s \end{Bmatrix} \tag{2.64}$$

where the subscript c stands for concrete and s stands for reinforcing steel.

Since the finite element model only includes the concrete displacement degrees of freedom, the degrees of freedom which are associated with the reinforcing steel need to be condensed out from the element stiffness matrix, before it is assembled into the structure stiffness matrix. By applying static condensation of the steel degrees of freedom in Eq. 2.64 the following relation between concrete displacements and corresponding forces results

$$\{P_c^*\} = [K_{cc}^*] \cdot \{d_c\} \tag{2.65}$$

where

$$\{P_c^*\} = \{P_c\} - [K_{cs}] \cdot [K_{ss}]^{-1} \cdot \{P_s\} \tag{2.66}$$

$$[K_{cc}^*] = [K_{cc}] - [K_{cs}] \cdot [K_{ss}]^{-1} \cdot [K_{cs}] \tag{2.67}$$

After some calculations for evaluating the inverse and carrying out the multiplications Eq. 2.67 reduces to:

$$[K_{cc}^*] = \frac{k_s \cdot k_{bi} \cdot k_{bj}}{k_s \cdot (k_{bi} + k_{bj}) + k_{bi} \cdot k_{bj}} \cdot \begin{bmatrix} 1 & -1 \\ -1 & 1 \end{bmatrix} = [K_{eq}]_s \tag{2.68}$$

which is the local stiffness matrix of the reinforcing steel element including the effect of bond slip and is equivalent to the local stiffness matrix in Eq. 2.30. The coefficient of the equivalent stiffness matrix can be rewritten as

$$\frac{k_s \cdot k_{bi} \cdot k_{bj}}{k_s \cdot (k_{bi} + k_{bj}) + k_{bi} \cdot k_{bj}} = \frac{k_s}{1 + k_s \cdot \left(\frac{1}{k_{bi}} + \frac{1}{k_{bj}} \right)} \tag{2.69}$$

It is now readily apparent from Eq. 2.69 that bond slip reduces the stiffness of the reinforcing steel element. In case of perfect bond the bond stiffness terms k_{bi} and k_{bj} become infinitely large and the expression in Eq. 2.69 reduces to k_s. In this case the stiffness matrix in Eq. 2.68 reduces to the local stiffness matrix of the embedded steel model with perfect bond in Eq. 2.30.

The process of transforming the local stiffness matrix of the reinforcing steel element to the global coordinate system is identical to that presented in Section 2.3.2 for the embedded steel element with perfect bond. Since the end points of the reinforcing steel element do not coincide with the nodes of the concrete element mesh, two transformation matrices are needed. By replacing $[K_{LO}]_s$ in Eq. 2.34 with $[K_{eq}]_s$ the transformation to global coordinates of the local stiffness matrix of the reinforcing steel element with bond slip takes the form

$$[K_{GL}]_s = [T_2]^T \cdot [T_1]^T \cdot [K_{eq}]_s \cdot [T_1] \cdot [T_2] \tag{2.70}$$

The steel stiffness matrix $[K_{GL}]_s$ in Eq. 2.70 can now be assembled together with the concrete element stiffness matrix to form the total stiffness of the structure.

Since the degrees of freedom associated with the reinforcing steel are condensed out of the stiffness matrix in Eq. 2.70, an additional step now becomes necessary for determining the deformations and forces in the reinforcing steel. Once the displacement increments at the nodes of the concrete finite elements are determined for the current load increment, they can be transformed by matrices $[T_1]$ and $[T_2]$ to yield the concrete displacements $\{d_c\}$ at the ends of the steel element. The vector $\{d_c\}$ has only two components which are the end displacements parallel to the axis of the bar. Using the second row of the matrix relation in Eq. 2.64

$$\{P_s\} = [K_{cs}] \cdot \{d_c\} + [K_{ss}] \cdot \{d_s\} \tag{2.71}$$

and solving for $\{d_s\}$ yields

$$[K_{ss}] \cdot \{d_s\} = (\{P_s\} - [K_{cs}] \cdot \{d_c\}) \tag{2.72}$$

Eq. 2.72 expresses the equilibrium of the reinforcing bar element. After assembling the steel element stiffness matrices on the left hand side and the forces on the right hand side of the equation and imposing appropriate boundary conditions at the ends of the reinforcing bar the simultaneous solution of the equations of equilibrium yields the steel deformations and forces. Alternatively, it is possible to rewrite Eq. 2.72 so as to yield the steel force and deformation at one end of the steel element as a function of the force and deformation at the other end. The successive application of this relation along with appropriate conditions for the transition from one element to the next results in a transfer matrix solution method, which offers certain computational advantages over the direct solution method. The numerical implementation of these methods and their advantages and disadvantages will be discussed in the following chapter.

CHAPTER 3
FINITE ELEMENT MODELING OF RC BEAMS AND SLABS

3.1 General

The finite element method is a general method of structural analysis in which the solution of a problem in continuum mechanics is approximated by the analysis of an assemblage of finite elements which are interconnected at a finite number of nodal points and represent the solution domain of the problem.

The finite element method is now well accepted as the most powerful general technique for the numerical solution of a variety of engineering problems. Applications range from the stress analysis of solids to the solution of acoustical phenomena, neutron physics and fluid dynamic problems. Indeed the finite element method is now established as a general numerical method for the solution of partial differential equations subject to known boundary and initial conditions.

In the realm of linear analysis the finite element method is now widely used as a design tool. A similar acceptance in nonlinear analysis problems depends on two major factors. First, the increase in computational effort which is required for nonlinear problems necessitates that considerable computing power be available at low cost to the designer. Developments in the last two decades have ensured that high-speed digital computers have gradually become available to the average designer and indications are that reductions in unit computing costs will continue at an accelerating pace.

The second major factor is related to the level of complexity of nonlinear analysis. Before application of nonlinear methods can become commonplace in design situations, the accuracy and reliability of the proposed models has to be established beyond doubt. The development of improved element characteristics and more efficient nonlinear solution algorithms as well as the experience gained in their application to engineering problems have ensured that nonlinear finite element analysis can now be performed with some confidence. Thus, barriers to the wide use of nonlinear finite element techniques are gradually removed. Nevertheless, difficulties still abound whose solution will require much effort on the part of researchers and designers.

The behavior of RC structures is distinctly nonlinear, because of several factors: (1) nonlinear material behavior of concrete and steel and their interaction through bond and dowel action; (2)

cracking of concrete; and (3) time dependent effects such as creep, shrinkage, temperature and load history. In dealing with these problems in an analytical setting several nonlinear solution algorithms are now available.

This chapter first presents the underlying theoretical assumptions of the RC beam and slab model used in this study. This is followed by the solution of the problem in the finite element context. Following a brief description of nonlinear solution algorithm a detailed step-by-step organization of the nonlinear solution strategy is presented.

3.2 Theoretical Considerations

For the analysis of RC beams the Timoshenko beam theory is used in the present study. Since this theory is well established and widely used in the analysis of beams, attention is focused below on some theoretical aspects of the plate bending problem followed by the finite element implementation of the material models of Chapter 2 in the analysis of RC beams and slabs.

In the analysis of thin plates it is generally assumed that the plate thickness is small relative to the dimensions in the x-y plane, which is the plane of the plate. When plates are subjected to in-plane loads the resulting stresses are assumed to be constant through the thickness of the plate and stresses σ_z, τ_{xz} and τ_{yz} are ignored. For out-of-plane loading the Mindlin plate bending theory, which includes the effect of transverse shear deformations, is adopted in this study (Owen and Hinton 1978). The main assumptions of the theory are:

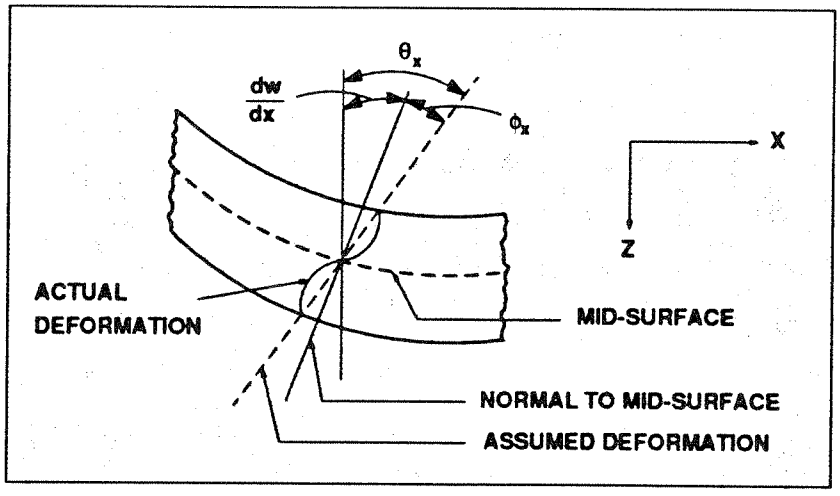

Fig. 3.1 Assumed Deformation of Mindlin Plate Theory

(1) transverse displacements are small relative to the plate thickness,

(2) the stress normal to the mid-surface of the plate is negligible, and

(3) normals to the mid-surface of the slab before deformation remain straight, but not necessary normal to the mid-surface after deformation, as shown in Fig. 3.1. The force resultants and corresponding deformations of a typical Mindlin plate are shown in Fig. 3.2.

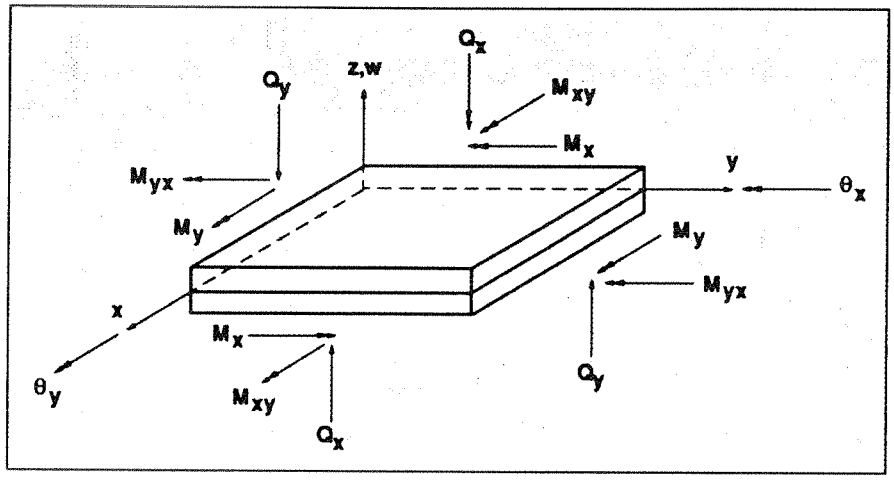

Fig. 3.2 Typical Mindlin Plate

The deformation field of the problem consists of three components:

$$\{d\} = \{w, \theta_x, \theta_y\}^T \tag{3.1}$$

where w is the transverse plate displacement normal to the xy plane and θ_x and θ_y are the rotations about the y-and the x-axis, respectively (Fig. 3.2). Under the assumptions of the Mindlin plate theory it holds that

$$\theta_x = \frac{\partial w}{\partial x} - \phi_x \tag{3.2}$$

$$\theta_y = \frac{\partial w}{\partial y} - \phi_y \tag{3.3}$$

where φ_x and φ_y are transverse shear rotations (Fig. 3.1).

Making use of the basic assumptions of the theory the displacements of any point in the plate can be expressed by:

$$u(x,y,z) = u_o(x,y) + [\, d_{nx}(x,y) - z \,] \cdot \theta_x \tag{3.4}$$

$$v(x,y,z) = v_o(x,y) + [\, d_{ny}(x,y) - z \,] \cdot \theta_y \tag{3.5}$$

$$w(x,y,z) = w_o(x,y) \tag{3.6}$$

where d_{nx} and d_{ny} is the distance from the top surface of the plate to a point in the plate with in-plane deformations of u_o and v_o, respectively. It should be noted that d_{nx} and d_{ny} are not necessarily equal.

The bending strains ε_x, ε_y and γ_{xy} vary linearly through the plate thickness and can be derived by taking derivatives of Eqs. 3.4-3.6:

$$\varepsilon_x = \frac{\partial u}{\partial x} = \frac{\partial u_o}{\partial x} + (d_{nx} - z) \cdot \frac{\partial \theta_x}{\partial_x} = \varepsilon_{ox} + (d_{nx} - z) \cdot \frac{\partial \theta_x}{\partial x} \tag{3.7}$$

$$\varepsilon_y = \frac{\partial v}{\partial y} = \frac{\partial v_o}{\partial y} + (d_{ny} - z) \cdot \frac{\partial \theta_y}{\partial_y} = \varepsilon_{oy} + (d_{ny} - z) \cdot \frac{\partial \theta_y}{\partial y} \tag{3.8}$$

$$\gamma_{xy} = \frac{\partial u}{\partial y} + \frac{\partial v}{\partial x} = \frac{\partial u_o}{\partial y} + \frac{\partial v_o}{\partial x} + (d_{nx} - z) \cdot \frac{\partial \theta_x}{\partial_y} + (d_{ny} - z) \cdot \frac{\partial \theta_y}{\partial_x}$$

$$= \gamma_{oxy} + (d_{nx} - z) \cdot \frac{\partial \theta_x}{\partial y} + (d_{ny} - z) \cdot \frac{\partial \theta_y}{\partial x} \tag{3.9}$$

or

$$\{\varepsilon_x, \varepsilon_y, \gamma_{xy}\} = \{\varepsilon_p\}^T \tag{3.10}$$

Since γ_{xy} varies linearly with distance z, Eq. 3.9 can be simplified to the following relation

$$\gamma_{xy} = \gamma_{oxy} - (z - d_{nxy}) \cdot \left(\frac{\partial \theta_x}{\partial y} + \frac{\partial \theta_y}{\partial x} \right) \tag{3.11}$$

The transverse shear strains, on the other hand, are constant through the thickness and can be expressed as follows:

$$\gamma_{zx} = \frac{\partial w}{\partial x} - \theta_x \tag{3.12}$$

$$\gamma_{yz} = \frac{\partial w}{\partial y} - \theta_y \tag{3.13}$$

or

$$\{\gamma_{zx}, \gamma_{yz}\} = \{\varepsilon_t\}^T \tag{3.14}$$

Finally, d_{nx}, d_{ny} and d_{nxy}, which represent the arbitrary depths of ε_{ox} , ε_{oy}, and γ_{oxy} respectively, (Fig. 3.3) can be determined from the condition that $\int \sigma_x dz = \int \sigma_y dz = \int \tau_{xy} dz = 0$, which decouples the in-plane from the out-of-plane forces. Assuming that the shear modulus G is constant through the depth of the slab leads to the conclusion that d_{nxy} is equal to $d/2$, where d is the slab thickness.

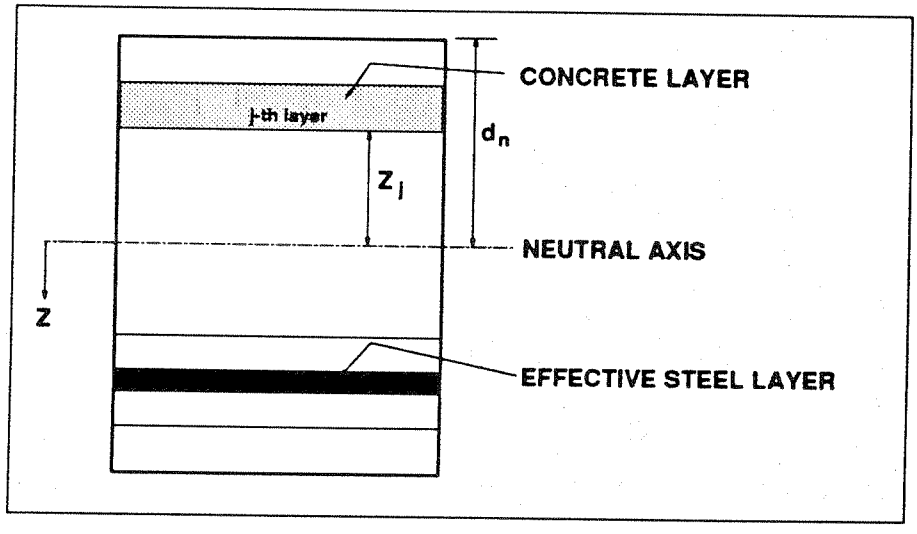

Fig. 3.3 Layer Section

The bending strain components of Eqs. 3.7-3.9 can be expressed as follows:

$$\{\varepsilon_p\} = \begin{Bmatrix} \varepsilon_x \\ \varepsilon_y \\ \gamma_{xy} \end{Bmatrix} = \begin{Bmatrix} (d_{nx} - z) \cdot \dfrac{\partial \theta_x}{\partial x} \\ (d_{ny} - z) \cdot \dfrac{\partial \theta_y}{\partial y} \\ (\gamma_{nxy} - z) \cdot \left(\dfrac{\partial \theta_x}{\partial y} + \dfrac{\partial \theta_y}{\partial x} \right) \end{Bmatrix} \tag{3.15}$$

The effect of τ_{zx} and τ_{yz} was ignored in this derivation. This is a reasonable approximation, since, in the absence of in-plane forces, the in-plane stresses reach a maximum at the extreme fibers, where the transverse shear stresses are at their lowest value, and reach a minimum at mid-depth of the slab, where the transverse shear stresses are highest. Thus, in the absence of in-plane forces the interaction between transverse shear stresses and in-plane stresses is relatively small and can be neglected.

3.3 Finite Element Representation

The finite element analysis of a continuum starts with the subdivision of the physical system into an assemblage of discrete elements. The displacement vector $\{d\}$ at any point within a particular structure is approximated by interpolating functions associated with generalized coordinates d_i, which are the displacements of the nodes of the finite element discretization of the structure. For a finite element this approximation can be formally written as

$$\{d\} = [N] \cdot \{d\}^{ele} = [N_1 \ldots N_i \ldots] \cdot \begin{Bmatrix} d_1 \\ \cdot \\ \cdot \\ \cdot \\ d_i \\ \cdot \\ \cdot \\ \cdot \end{Bmatrix} \tag{3.16}$$

where the components of $[N]$ are, in general, functions of position and $\{d\}^{ele}$ is the vector of the node displacements of a particular element. Once the displacements are known at any point within the element, the strains can be determined from the strain-displacement relation. In the discrete problem this can be formally written as

$$\{\varepsilon\} = [B] \cdot \{d\}^{ele} \tag{3.17}$$

The matrix $[B]$ will be derived later for beams and slabs separately. The stresses can now be determined from the material constitutive law

$$\{\sigma\} = [D] \cdot (\{\varepsilon\} - \{\varepsilon_o\}) + \{\sigma_o\} \tag{3.18}$$

where $[D]$ is the element material matrix, $\{\varepsilon_o\}$ is the initial strain vector and $\{\sigma_o\}$ is the initial stress vector.

By applying the virtual work principle or the theorem of minimum potential energy to the assemblage of discrete elements the following equilibrium equations result

$$[K]\cdot\{d\}+\{F\}_p+\{F\}_g+\{F\}_{\varepsilon_o}+\{F\}_{\sigma_o}-\{R\}=0 \tag{3.19}$$

The terms in Eq. 3.19 are derived as follows:

the stiffness matrix [K],

$$[K]=\sum_{ele}\int[B]^T\cdot[D]\cdot[B]\,dV \tag{3.20}$$

the nodal forces due to surface traction,

$$\{F\}_p=-\sum_{ele}\int[N]^T\cdot\{p\}\,dA \tag{3.21}$$

the nodal forces due to body forces,

$$\{F\}_g=-\sum_{ele}\int[N]^T\cdot\{g\}\,dV \tag{3.22}$$

the nodal forces due to initial strains,

$$\{F\}_{\varepsilon_o}=-\sum_{ele}\int[B]^T\cdot[D]\cdot\{\varepsilon_o\}\,dV \tag{3.23}$$

and the nodal forces due to initial stresses

$$\{F\}_{\sigma_o}=-\sum_{ele}\int[B]^T\cdot\{\sigma_o\}\,dV \tag{3.24}$$

In Eqs. 3.19-3.24 $\{d\}$ is the vector of node displacements, $\{R\}$ is the vector of applied nodal forces, $\{p\}$ is the vector of surface forces and $\{g\}$ is the vector of body forces.

The node displacements $\{d\}$ can be determined from the solution of the system of simultaneous algebraic equations in Eq. 3.19, whereupon the strains and stresses at any point of the structure can be obtained from Eqs. 3.17 and 3.18. In a nonlinear problem the stiffness matrix $[K]$ depends on the displacement vector $\{d\}$ and the nonlinear system of algebraic equations in Eq. 3.19 has to be solved by one of the nonlinear solution methods in Section 3.4.

3.3.1 Reinforced Concrete Beams

The finite element idealization of reinforced concrete beams is accomplished by two-dimensional elements which lie in the x-y plane of the beam elevation. Following the assumptions

of the Timoshenko beam theory the resulting stresses are assumed to be constant through the thickness of each element and stresses σ_z, τ_{xz} and τ_{yz} are ignored. These assumptions lead to a plane stress field. The displacement field is described by u and v, which represent the node displacements in the x and y-direction, respectively and are in general functions of x and y. These functions must satisfy C^0 continuity. The process of the finite element discretization of this displacement field can be formally written as

$$\{d\} = \begin{Bmatrix} u \\ v \end{Bmatrix} = \sum_{j=1}^{n} \begin{bmatrix} N_j & 0 \\ 0 & N_j \end{bmatrix} \cdot \begin{Bmatrix} u \\ v \end{Bmatrix}_j \tag{3.25}$$

where n is the number of nodes of the finite element discretization of the structure and N_j is the shape function for j-th node.

The application of the strain-displacement relation leads to

$$\begin{Bmatrix} \varepsilon_x \\ \varepsilon_y \\ \gamma_{xy} \end{Bmatrix} = \begin{bmatrix} \dfrac{\partial N}{\partial x} & 0 \\ 0 & \dfrac{\partial N}{\partial y} \\ \dfrac{\partial N}{\partial y} & \dfrac{\partial N}{\partial x} \end{bmatrix} \cdot \begin{Bmatrix} u \\ v \end{Bmatrix}^{ele} \tag{3.26}$$

or, in compact form to

$$\{\varepsilon_p\} = [B] \cdot \{d\}^{ele} \tag{3.27}$$

The stiffness matrix of the composite reinforced concrete finite element is arrived at by superposition of the concrete and reinforcing steel stiffness matrices derived in Chapter 2. The steel stiffness matrix of the discrete element also includes the effect of bond-slip, as described in Section 2.5. This process can be formally expressed as

$$[K]_{ele} = [K]_c + \sum_{i=1}^{n} \left([K_{GL}]_s \right)_i \tag{3.28}$$

n is the number of steel elements embedded in the concrete element and $[K_{GL}]_s$ is the global stiffness matrix of the discrete steel element without bond-slip (Eq. 2.34) or with bond-slip (Eq. 2.70). The concrete element stiffness $[K]_c$ is determined from

$$[K]_c = \int_V [B]^T \cdot [D_{GL}]_c \cdot [B] \, dV \tag{3.29}$$

where $[D_{GL}]_c$ is the concrete material matrix in global coordinates in Eq. 2.25. The assembly of the element stiffness matrices $[K]_{ele}$ results in the structural stiffness matrix $[K]$.

3.3.2 Reinforced Concrete Slabs

The Mindlin plate element requires only C^0 continuity of the transverse displacement function w and the two independent rotation functions θ_x and θ_y. By contrast, the plate element which is based on the classical Kirchhoff thin plate theory requires C^1 continuity, since the derivatives $\partial w/\partial x$ and $\partial w/\partial y$ of the displacement function w as well as w itself must be continuous across the element interfaces. The proposed Mindlin plate element, therefore, not only accounts for the transverse shear deformations, but is also simpler to formulate.

Based on the assumptions of the Mindlin plate theory and the continuity requirements of the finite element method the displacement field in Eq. 3.1 can be expressed in the following matrix form

$$\{d\} = \begin{Bmatrix} w \\ \theta_x \\ \theta_y \end{Bmatrix} = \sum_{j=1}^{n} \begin{bmatrix} N_j & 0 & 0 \\ 0 & N_j & 0 \\ 0 & 0 & N_j \end{bmatrix} \cdot \begin{Bmatrix} w \\ \theta_x \\ \theta_y \end{Bmatrix}_j \tag{3.30}$$

where n is the number of nodes of the finite element discretization of the structure and N_j is the shape function for j-th node.

Using Eq. 3.15 the relation between in-plane strains and displacements becomes

$$\begin{Bmatrix} \varepsilon_x \\ \varepsilon_y \\ \gamma_{xy} \end{Bmatrix} = \begin{bmatrix} (z-d_{nx}) & 0 & 0 \\ 0 & (z-d_{ny}) & 0 \\ 0 & 0 & (z-d_{nxy}) \end{bmatrix} \cdot \begin{bmatrix} 0 & -\dfrac{\partial N}{\partial x} & 0 \\ 0 & 0 & -\dfrac{\partial N}{\partial y} \\ 0 & -\dfrac{\partial N}{\partial y} & -\dfrac{\partial N}{\partial x} \end{bmatrix} \cdot \begin{Bmatrix} w \\ \theta_x \\ \theta_y \end{Bmatrix}^{ele} \tag{3.31}$$

or, in compact form

$$\{\varepsilon_p\} = [d_n] \cdot [B_p] \cdot \{d\}^{ele} \tag{3.32}$$

From Eqs. 3.12 and 3.13 the relation between transverse shear strains and displacements becomes

$$\begin{Bmatrix} \gamma_{zx} \\ \gamma_{yz} \end{Bmatrix} = \begin{bmatrix} \dfrac{\partial N}{\partial x} & -N & 0 \\ \dfrac{\partial N}{\partial x} & 0 & -N \end{bmatrix} \cdot \begin{Bmatrix} w \\ \theta_x \\ \theta_y \end{Bmatrix}^{ele} \tag{3.33}$$

or, in compact form

$$\{\varepsilon_t\} = [B_t] \cdot \{d\}^{ele} \tag{3.34}$$

The strain vector results from the combination of Eq. 3.33 with Eq. 3.34

$$\{\varepsilon\} = \begin{Bmatrix} \{\varepsilon_p\} \\ \{\varepsilon_t\} \end{Bmatrix} = \begin{bmatrix} [d_n] \cdot [B_p] \\ [B_t] \end{bmatrix} \cdot \begin{Bmatrix} w \\ \theta_x \\ \theta_y \end{Bmatrix}^{ele} \tag{3.35}$$

With the decomposition of the strain field in Eq. 3.35 the Mindlin plate element stiffness matrix consists of two parts

$$\begin{aligned} [K] &= \int_V [B_p]^T \cdot [d_n]^T \cdot [D_p] \cdot [d_n] \cdot [B_p]\, dV + \int_V [B_t]^T \cdot [D_t] \cdot [B_t]\, dV \\ &= [K_p] + [K_t] \end{aligned} \tag{3.36}$$

where

$$\begin{aligned} [K_p] &= \int_V [B_p]^T \cdot [d_n]^T \cdot [D_p] \cdot [d_n] \cdot [B_p]\, dV \\ &= \int_A [B_p]^T \cdot \left(\int [d_n]^T \cdot [D_p] \cdot [d_n]\, dz \right) \cdot [B_p]\, dA \\ &= \int_A [B_p]^T \cdot [\bar{D}_p] \cdot [B_p]\, dA \end{aligned} \tag{3.37}$$

and

$$\begin{aligned} [K_t] &= \int_V [B_t]^T \cdot [D_t] \cdot [B_t]\, dV \\ &= \int_A [B_t]^T \cdot \left(\int [D_t]\, dz \right) \cdot [B_t]\, dA = \int_A [B_t]^T \cdot [\bar{D}_t] \cdot [B_t]\, dA \end{aligned} \tag{3.38}$$

In Eqs. 3.36-3.38 $[D_p]$ is the bending and $[D_t]$ is the shear component of the material matrix, respectively.

The integration through the depth of the slab, which is placed in parentheses in Eqs. 3.37 and 3.38, is performed by subdividing the slab into imaginary steel and concrete layers, as shown in Fig. 3.3. The transverse displacement field is assumed to be continuous in each slab element so that

there are no gaps between layers. Each layer can have different material properties, which are, however, assumed to be constant through the thickness of the layer. The integrals through the depth of the slab can be evaluated by summation over all layers

$$[\bar{D}_p] = \int [d_n]^T \cdot [D_p] \cdot [d_n]\, d\bar{z} \tag{3.39}$$

$$= \sum_{j=1}^{n_c} \int_{\bar{z}_j}^{\bar{z}_{j+1}} \bar{z}^2 \cdot [D_{pc}]_j \, d\bar{z} + \sum_{i=1}^{n_s} \bar{z}^2 \cdot [D_s]_i \cdot t_i$$

$$= \frac{1}{3} \cdot \sum_{j=1}^{n_c} (\bar{z}_{j+1}^3 - \bar{z}_j^3) \cdot [D_{pc}]_j + \sum_{i=1}^{n_s} \bar{z}^2 \cdot [D_s]_i \cdot t_i$$

and

$$[\bar{D}_t] = \int [D_t]\, d\bar{z} = \sum_{j=1}^{n_c} (\bar{z}_{j+1} - \bar{z}_j) \cdot [D_{tc}]_j \tag{3.40}$$

where $\bar{z} = z - (d_{nx} + d_{ny})/2$ for simplicity and n_c and n_s is the total number of concrete and steel layers, respectively. $[D_{pc}]_j$ is the plane stress material matrix of the j-th concrete layer, $[D_{tc}]_j$ is the transverse shear material matrix of the j-th concrete layer and $[D_s]_i$ is the material matrix of the i-th steel layer whose thickness is established from Eq. 2.50 based on the distributed steel model. The reinforcing steel only contributes to the in-plane stiffness of the slab, since the dowel action of the reinforcement is neglected in this study.

Once the node displacements of the finite element model are determined, Eqs. 3.31 and 3.33 yield the in-plane and the transverse shear strains of each layer, respectively. These relations are summarized below

$$\{\varepsilon_c\}_j = \begin{cases} \varepsilon_{xj} = \left[d_{nx} - \frac{1}{2}(z_{j+1} + z_j) \right] \cdot \frac{\partial \theta_x}{\partial x} \\ \varepsilon_{yj} = \left[d_{ny} - \frac{1}{2}(z_{j+1} + z_j) \right] \cdot \frac{\partial \theta_y}{\partial y} \\ \gamma_{xyj} = \left[\frac{d}{2} - \frac{1}{2}(z_{j+1} + z_j) \right] \cdot \left(\frac{\partial \theta_x}{\partial y} + \frac{\partial \theta_y}{\partial x} \right) \\ \gamma_{xzj} = \frac{\partial w}{\partial x} - \theta_x \\ \gamma_{yzj} = \frac{\partial w}{\partial y} - \theta_y \end{cases} \tag{3.41}$$

$$\{\varepsilon_s\}_i = \begin{cases} \varepsilon_{xi} = (d_{nx} - z_i) \cdot \dfrac{\partial \theta_x}{\partial x} \\ \varepsilon_{yi} = (d_{ny} - z_i) \cdot \dfrac{\partial \theta_y}{\partial y} \end{cases} \tag{3.42}$$

The stresses of each layer are determined from the corresponding material stress-strain relation

$$\{\sigma_c\}_j = [D_c]_j \cdot \{\varepsilon_c\}_j \tag{3.43}$$

$$\{\sigma_s\}_i = [D_s]_i \cdot \{\varepsilon_s\}_i \tag{3.44}$$

where $\{\sigma_s\}_i$ and $\{\varepsilon_s\}_i$ denote the stress and strain at mid-depth z_i of the i-th steel layer, and $\{\sigma_c\}_j$ and $\{\varepsilon_c\}_j$ denote the stress and strain at mid-depth of the j-th concrete layer, respectively.

In the nonlinear analysis algorithm used in this study, the nonlinear constitutive relations are satisfied by iterative successive corrections. In each iteration the stresses are determined from the corresponding strain increments at the end of the previous iteration step, while the material properties are only updated at the beginning of the next load step.

Since in a nonlinear problem the stresses which are determined during the iterative phase of the algorithm are not, generally, in equilibrium with the applied loads, unbalanced nodal forces result. These are corrected during the subsequent iteration until a specified tolerance is satisfied. The unbalanced nodal forces are the difference between applied and resisting or equivalent forces

$$\{R\}_{unbalanced} = \{R\}_{applied} - \{R\}_{equivalent} \tag{3.45}$$

The resisting nodal forces are statically equivalent to the stress field which results from the current deformation state of the finite element model. The resisting nodal forces are determined from

$$\begin{aligned} \{R\}_{equivalent} &= \int_V [B]^T \cdot \{\sigma\}\, dV = \int_V [B_p]^T \cdot [d_n]^T \cdot \{\sigma_p\}\, dV + \int_V [B_t]^T \cdot \{\sigma_t\}\, dV \\ &= \int [B_p]^T \cdot \left(\int [d_n]^T \cdot \{\sigma_p\}\, dz \right) dA + \int [B_t]^T \cdot \left(\int \{\sigma_t\}\, dz \right) dA \\ &= \int [B_p]^T \cdot \{\tilde{\sigma}_p\}\, dA + \int [B_t]^T \cdot \{\tilde{\sigma}_t\}\, dA \end{aligned} \tag{3.46}$$

and the integration through the depth of the slab is performed by summation over all imaginary concrete and steel layers

$$\{\tilde{\sigma}_p\} = \begin{cases} \tilde{\sigma}_x = \sum_{j=1}^{n_c} \frac{1}{2} \cdot [(z_{j+1} - d_{nx})^2 - (z_j - d_{nx})^2] \cdot \sigma_x + \sum_{i=1}^{n_s} (z_i - d_{nx}) \cdot \sigma_x \cdot t_i \\ \tilde{\sigma}_y = \sum_{j=1}^{n_c} \frac{1}{2} \cdot [(z_{j+1} - d_{ny})^2 - (z_j - d_{ny})^2] \cdot \sigma_y + \sum_{i=1}^{n_s} (z_i - d_{ny}) \cdot \sigma_y \cdot t_i \\ \tilde{\tau}_{xy} = \sum_{j=1}^{n_c} \frac{1}{2} \cdot \left[\left(z_{j+1} - \frac{d}{2} \right)^2 - \left(z_j - \frac{d}{2} \right)^2 \right] \cdot \tau_{xy} \end{cases} \tag{3.47}$$

$$\{\tilde{\sigma}_t\} = \begin{cases} \tilde{\tau}_{xx} = \sum_{j=1}^{n_c} (z_{j+1} - z_j) \cdot \tau_{xx} \\ \tilde{\tau}_{yz} = \sum_{j=1}^{n_c} (z_{j+1} - z_j) \cdot \tau_{yz} \end{cases} \tag{3.48}$$

Details of the numerical implementation along with a summary of the algorithm and a discussion of the convergence criterion are presented in the following section.

3.4 Numerical Implementation

3.4.1 Iteration Method

The numerical implementation of the finite element model requires the solution of Eq. 3.19. This is a system of simultaneous nonlinear equations, since the stiffness matrix [*K*], in general, depends on the displacement vector {*d*}. The solution of this system of nonlinear equations is typically accomplished with an iterative method. The load vector {*R*} is subdivided into a number of sufficiently small load increments, which are successively applied (Fig. 3.4).

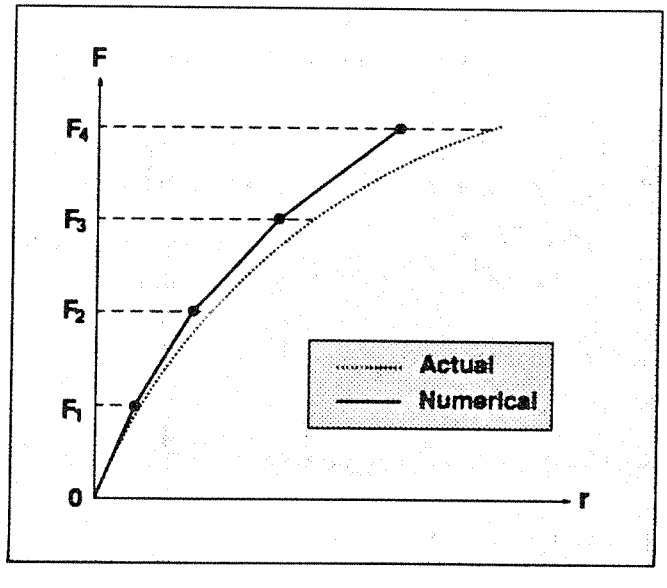

Fig. 3.4 Incremental Load Method without Correction

At each load step a linear approximation of the stiffness matrix [K] is established and the resulting system of linear equilibrium equations is solved for the displacement increments which correspond to the applied load increments. Since the stiffness matrix [K] changes under these displacement increments, the resisting forces of the structure do not equilibrate the applied loads and unbalanced loads result (Eq. 3.45). In the subsequent correction phase the displacement increments are iteratively improved, until a specified convergence criterion is satisfied. If no correction phase is included in the nonlinear analysis algorithm, the numerical error grows from one load step to the next and the numerical solution drifts away from the actual response, as shown in Fig. 3.4.

Depending on how the stiffness matrix [K] is updated during the correction phase, the iterative method can be classified into three broad categories even though variations of these schemes are also possible: the initial or constant stiffness method, the tangent stiffness method and the secant stiffness method (Taylor and Hinton 1980).

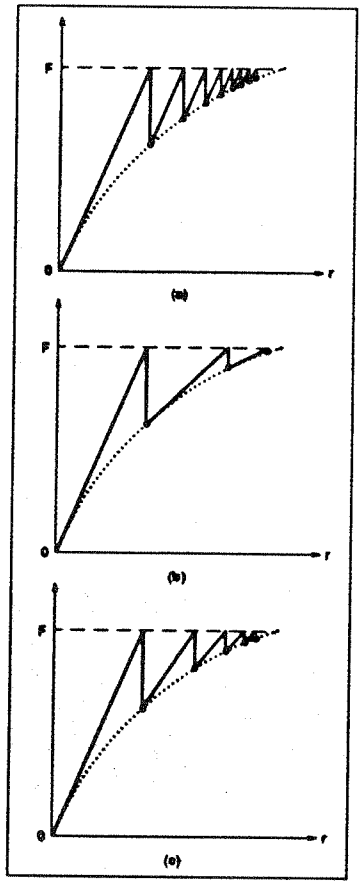

The tangent stiffness method requires the smallest number of iterations to arrive at the solution, but has the disadvantage that the stiffness matrix [K] needs to be reformed and triangularized at each iteration. The initial stiffness method, on the other extreme, requires the largest number of iterations, but the stiffness matrix [K] is only formed and triangularized once at the beginning of the load step. Generally, the tangent stiffness method is more efficient than the initial stiffness method for models with a small number of degrees of freedom, even though the selection of one method over another often depends on numerical stability considerations. The secant method, for example, is well suited for structures which exhibit softening response.

Fig. 3.5 ***Iterative Method***
(a) Initial Stiffness Method
(b) Tangent Stiffness Method
(c) Secant Stiffness Method

Even though it is possible to use any stiffness matrix in the first iteration of a new load increment, which constitutes the advancing phase of the solution algorithm, it is quite common to use the tangent stiffness matrix for this purpose. The nonlinear solution scheme selected in this study uses the tangent stiffness matrix at the beginning of the load step in combination with a constant stiffness matrix during the subsequent correction phase, as shown in Fig. 3.6.

3.4.2 Solution Algorithm

Every nonlinear analysis algorithm consists of four basic steps: the formation of the current stiffness matrix, the solution of the equilibrium equations for the displacement increments, the state determination of all elements in the model and the convergence check. These steps are presented in some detail in the flow diagram of Fig. 3.7 for the plane stress and the plate bending problem.

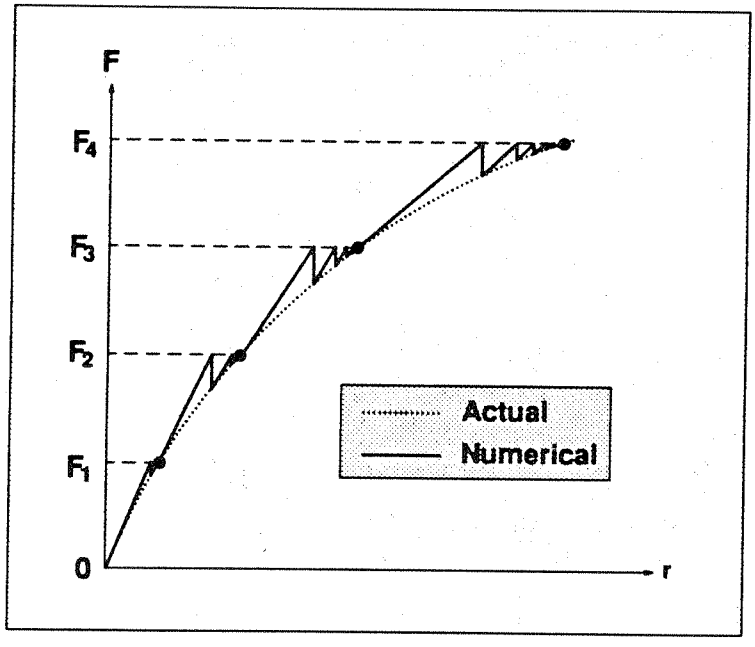

Fig. 3.6 Modified Newton-Raphson algorithm

A summary of the steps of the nonlinear solution algorithm along with the corresponding operations is presented below and is also identified in Fig. 3.7.

1. Form the tangent stiffness matrix [*K*] at the current displacement state of the finite element model.

   (a) In the case of RC beams use Eqs. 3.28 and 3.29 and 2.34

   (b) In the case of RC slabs use Eqs. 3.36-3.38

2. Given the current load increment $\{\Delta R\}$ calculate the node displacement increments from Eq. 3.19, which is recast in incremental form

$$[K]\cdot\{\Delta d\}+\{F\}_p+\{F\}_g+\{F\}_{\varepsilon_o}+\{F\}_{\sigma_o}-\{\Delta R\}=0$$

and determine the current displacement increments $\{\Delta d\}$ and displacements $\{d\}$.

3. Apply the strain-displacement relation to determine the **concrete** strains.

   (a) In the case of RC beams use Eq. 3.27.

$$\{\varepsilon_p\}=[B]\cdot\{d\}^{ele}$$

   (b) In the case of RC slabs use Eq. 3.41

$$\{\varepsilon_c\}_j=\begin{cases}\varepsilon_{xj}=\left[d_{nx}-\dfrac{1}{2}(z_{j+1}+z_j)\right]\cdot\dfrac{\partial\theta_x}{\partial x}\\ \varepsilon_{yj}=\left[d_{ny}-\dfrac{1}{2}(z_{j+1}+z_j)\right]\cdot\dfrac{\partial\theta_y}{\partial y}\\ \gamma_{xyj}=\left[\dfrac{d}{2}-\dfrac{1}{2}(z_{j+1}+z_j)\right]\cdot\left(\dfrac{\partial\theta_x}{\partial y}+\dfrac{\partial\theta_y}{\partial x}\right)\\ \gamma_{zxj}=\dfrac{\partial w}{\partial x}-\theta_x\\ \gamma_{yzj}=\dfrac{\partial w}{\partial y}-\theta_y\end{cases}\qquad(3.41)$$

4. Determine the new crack direction (Eq. 2.27)

$$\tan 2\theta=\frac{\gamma_{xy}}{\varepsilon_x-\varepsilon_y}$$

5. Calculate the principal concrete strains (Eq. 2.28)

$$\begin{Bmatrix}\varepsilon_1\\ \varepsilon_2\end{Bmatrix}=\begin{bmatrix}\cos^2\theta & \sin^2\theta & \sin\theta\cos\theta\\ \sin^2\theta & \cos^2\theta & -\sin\theta\cos\theta\end{bmatrix}\cdot\begin{Bmatrix}\varepsilon_x\\ \varepsilon_y\\ \gamma_{xy}\end{Bmatrix}$$

6. Use the concrete stress-strain relation to calculate the stresses in the global coordinate system

   (a) In the case of RC beams use the following equation.

$$\begin{Bmatrix}\sigma_x\\ \sigma_y\\ \tau_{xy}\end{Bmatrix} = [D_{GL}]_c \cdot \begin{Bmatrix}\varepsilon_x\\ \varepsilon_y\\ \gamma_{xy}\end{Bmatrix}$$

(b) In the case of RC slabs use Eq. 3.43.

$$\{\sigma_c\}_j = [D_c]_j \cdot \{\varepsilon_c\}_j$$

7. Determine the principal stresses from the stresses in the global coordinate system using Eq. 2.29.

$$\begin{Bmatrix}\sigma_1\\ \sigma_2\end{Bmatrix} = \begin{bmatrix}\cos^2\theta & \sin^2\theta & 2\sin\theta\cos\theta\\ \sin^2\theta & \cos^2\theta & -2\sin\theta\cos\theta\end{bmatrix} \cdot \begin{Bmatrix}\sigma_x\\ \sigma_y\\ \tau_{xy}\end{Bmatrix}$$

8. Use the principal stresses to locate the present state of concrete in the biaxial principal stress space of Fig. 2.2 and, if required, determine new principal stress values from the principal strain values of Step 5. The process of state determination is different in each region of the principal stress space.

(a) In the compression-compression region:

(1) Unless concrete remains inside the initial yield surface, in which case the stresses are those of Steps 6 and 7, determine the principal stress ratio α from Eq. 2.3.

$$\alpha = \frac{\sigma_1}{\sigma_2} \qquad \text{where} \qquad (\ |\sigma_1| \geq |\sigma_2| \ )$$

(2) The ultimate strengths σ_{1p}, σ_{2p} and the corresponding strains $\varepsilon_{1p}, \varepsilon_{2p}$ of the stress-strain relations in the principal strain directions are recalculated with Eqs. 2.4-2.7.

$$\sigma_{2p} = \frac{1+3.65\alpha}{(1+\alpha)^2} \cdot f_c$$

$$\varepsilon_{2p} = \varepsilon_{co} \cdot \left(3\frac{\sigma_{2p}}{f_c} - 2\right)$$

$$\sigma_{1p} = \alpha \cdot \sigma_{2p}$$

$$\varepsilon_{1p} = \varepsilon_{co} \cdot \left[-1.6 \cdot \left(\frac{\sigma_{1p}}{f_c} \right)^3 + 2.25 \cdot \left(\frac{\sigma_{1p}}{f_c} \right)^2 + 0.35 \cdot \left(\frac{\sigma_{1p}}{f_c} \right) \right]$$

(3) The principal stresses are determined from the corresponding principal strains using the modified uniaxial stress-strain relation in Fig. 2.4. If the principal strain exceeds the crushing strain, the corresponding stress is set equal to zero.

(b) In the compression-tension and the tension-tension region:

(1) The principal stresses can be directly determined from the uniaxial stress-strain relation in Fig. 2.4. It is assumed that the presence of a tensile stress does not modify the uniaxial stress-strain relation in compression. The maximum tensile strength f_{eq} is reduced in accordance with the stress failure envelope in Fig. 2.2.

9. Determine the new stresses in the global coordinate system from the principal stresses.

$$\begin{Bmatrix} \sigma_x \\ \sigma_y \\ \tau_{xy} \end{Bmatrix} = \begin{bmatrix} \cos^2\theta & \sin^2\theta \\ \sin^2\theta & \cos^2\theta \\ \sin\theta\cos\theta & -\sin\theta\cos\theta \end{bmatrix} \cdot \begin{Bmatrix} \sigma_1 \\ \sigma_2 \end{Bmatrix}$$

10. Determine the equivalent nodal forces.

11. For RC slabs repeat Steps 3-10 for each concrete layer.

12. Repeat steps 3-11 for each integration point.

13. The calculations for the **reinforcing steel** depend on the type of reinforcing steel model used in the analysis.

(a) In the analysis of RC slabs with the distributed steel model:

(1) Determine the steel strains from the strain-displacement relation with Eq. 3.42

$$\{\varepsilon_s\}_i = \begin{cases} \varepsilon_{xi} = (d_{nx} - z_i) \cdot \dfrac{\partial \theta_x}{\partial x} \\ \varepsilon_{yi} = (d_{ny} - z_i) \cdot \dfrac{\partial \theta_y}{\partial y} \end{cases}$$

(2) Determine the new stress for the distributed steel model (Eq. 2.51).

(3) Transform the local steel stress to the global coordinate system.

(4) Determine the equivalent nodal forces.

(5) Repeat Steps (1)-(4) for each steel layer.

(6) Repeat steps (1)-(5) for each integration point.

(b) In the analysis of RC beams with a reinforcing steel model with perfect bond:

(1) Determine the displacement increments at the ends of the reinforcing bar element (Eq. 3.49).

$$\begin{Bmatrix} \Delta d_1 \\ \Delta d_2 \end{Bmatrix} = [T_1] \cdot [T_2] \cdot \{\Delta d\}^{ele}$$

(2) Calculate the steel forces according to the discrete reinforcing steel model with perfect bond with Eq. 2.30.

(3) Transform the local steel forces to the global coordinate system to obtain the contribution of the steel model to the equivalent nodal forces.

(4) Repeat steps (1)-(3) for each embedded reinforcing steel element.

(c) In the analysis of RC beams with a reinforcing steel model with bond-slip a special procedure is implemented which is described in detail in the following section. This procedure determines the contribution of steel and bond to the equivalent nodal forces at the concrete degrees of freedom from Eq. 2.66.

$$\{P_c^*\} = \{P_c\} - [K_{cs}] \cdot [K_{ss}]^{-1} \cdot \{P_s\}$$

This process is repeated for each embedded reinforcing steel element.

14. For RC slabs only calculate the new neutral axis location using the conditions:

$$\int \sigma_x dz = \int \sigma_y dz = \int \tau_{xy} dz = 0$$

Repeat for each integration point. The new neutral axis location is only used in the next load increment.

15. Assemble the equivalent nodal forces.

16. Repeat Steps 3-15 for all elements.

17. Calculate the unbalanced nodal forces from Eq. 3.45

$$\{R\}_{unbalanced} = \{R\}_{applied} - \{R\}_{equivalent}$$

18. Repeat Steps 2-17 until convergence occurs.

19. Increment the load and go back to Step 1.

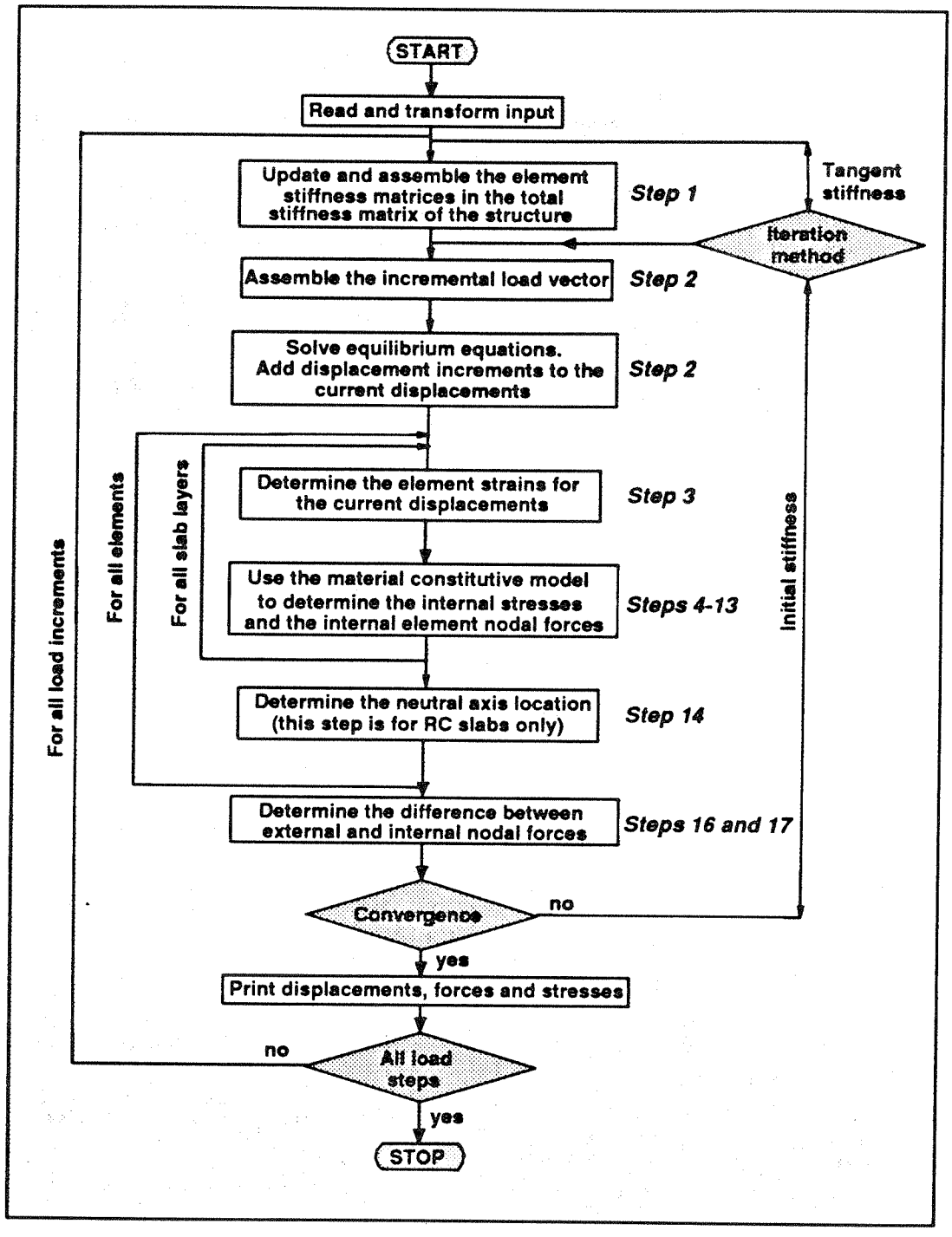

Fig. 3.7 Outline of Solution Algorithm

3.4.3 Solution Algorithm for Reinforcing Bar with Bond-Slip

In Step 2 of the solution algorithm the concrete displacement increments at the nodes of the finite element mesh are determined. If a reinforcing steel model with perfect bond is used, the displacement increments at the ends of the bar element are equal to the corresponding displacement increments of the quadrilateral concrete element, in which the bar element is embedded. In this case the displacement increments at the end of the reinforcing bar element can be determined from

$$\{\Delta d_s\} = [T_1] \cdot [T_2] \cdot \{\Delta d\}^{ele} \tag{3.49}$$

where the transformation matrices $[T_1]$ and $[T_2]$ are given by Eqs. 2.33 and 2.45 or 2.49, respectively. $\{\Delta d\}^{ele}$ is the vector of concrete displacement increments and $\{\Delta d_s\}$ is the vector of displacement increments at the ends of the reinforcing element parallel to the axis of the bar.

If the reinforcing steel model with bond-slip is used in the finite element analysis, then the relation between displacement increments at the ends of the reinforcing bar element and the corresponding concrete displacement increments is provided by Eq. 2.64. Since the terms of the stiffness matrix in Eq. 2.64 which correspond to the steel degrees of freedom are removed by static condensation before assembly into the structure stiffness matrix, the determination of the steel displacements and the corresponding forces now requires an additional step.

Once the displacement increments at the nodes of the concrete finite elements $\{\Delta d\}^{ele}$ are determined for the current load increment, they can be transformed by matrices $[T_1]$ and $[T_2]$ to yield the concrete displacement increments $\{\Delta d_c\}$ at the ends of the steel element and parallel to the axis of the bar

$$\{\Delta d_c\} = [T_1] \cdot [T_2] \cdot \{\Delta d\}^{ele} \tag{3.50}$$

Using the second row of the matrix relation in Eq. 2.64, which is rewritten in terms of displacement increments

$$\{\Delta P_s\} = [K_{cs}] \cdot \{\Delta d_c\} + [K_{ss}] \cdot \{\Delta d_s\} \tag{3.51}$$

and solving for $[\Delta d_s]$ yields

$$[K_{ss}] \cdot \{\Delta d_s\} = (\{\Delta P_s\} - [K_{cs}] \cdot \{\Delta d_c\}) \tag{3.52}$$

Eq. 3.52 expresses the condition of equilibrium of the reinforcing bar element. The steel force and deformation increments can now be determined by assembling the steel element matrices on the left hand side and the forces on the right hand side of the equation and imposing appropriate boundary conditions at the ends of the entire reinforcing bar. It should be noted that the only forces acting on

the reinforcing bar are the bond (transfer) forces and any applied end forces, so that upon completion of the assembly process only the term $-[K_{cs}] \cdot \{\Delta d_c\}$ and one concentrated force at each end remain on the right hand side of Eq. 3.52. Since the concrete displacement increments $\{\Delta d_c\}$ are known from Eq. 3.50, this system of linear equations can now be solved for the unknown steel displacement increments $\{\Delta d_s\}$. Once the steel displacement increments are determined, the state determination of the steel and bond elements is performed and the corresponding forces are determined. These are substituted into Eq. 2.66 to yield the contribution of the reinforcing steel model to the equivalent nodal forces at the global degrees of freedom. These forces are assembled for all steel and concrete elements (Step 16) and subtracted from the applied load increments (Step 16) to yield the unbalanced forces. The process continues until the convergence criterion is satisfied, as described previously. It should be noted that the bond and steel stiffness is not updated at every iteration, but only at the beginning of a new load increment, in accordance with the initial stiffness method which is used in this study. Consequently, the equilibrium of the reinforcing bar and the calculation of the equivalent nodal forces requires that the stiffness matrix of the entire reinforcing bar be triangularized only once at the beginning of a new load step.

An alternative solution to the direct stiffness method is the transfer matrix method. This method was already used by Ciampi et al. (1982), Filippou et al. (1983) and Filippou (1985) in the solution of the hysteretic behavior of anchored reinforcing bars. In the transfer matrix method the solution process starts at one end of the reinforcing bar where one boundary condition is known. The second condition is assumed, so that the solution can advance from one element to the next until reaching the far end of the reinforcing bar. The boundary condition which is known at the far end of the reinforcing bar provides the equation for determining the assumed boundary condition at the starting end. The implementation of the transfer matrix method in the solution of the equilibrium of the embedded reinforcing bar with bond-slip offers certain computational advantages over the direct stiffness method, as will be discussed in more detail later. Details of the implementation are presented in the following.

The reinforcing bar is subdivided into n-elements, as shown in Fig. 3.8. Eq. 2.64 represents the equilibrium equations of a steel element. Focusing attention on the k-th element Eq. 3.51 yields

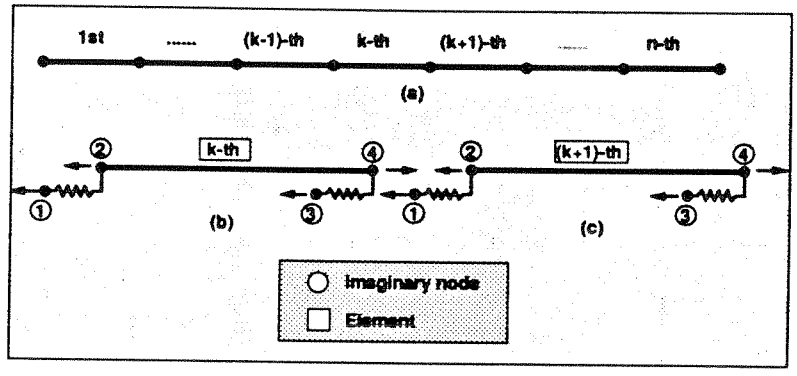

Fig. 3.8 Modeling of Reinforcing Bar for Transfer Matrix Method

$$\{\Delta P_s\}^k = [K_{cs}]^k \cdot \{\Delta d_c\}^k + [K_{ss}]^k \cdot \{\Delta d_s\}^k \tag{3.53}$$

with reference to Eq. 2.63 in incremental form Eq. 3.53 can be explicitly written (Fig. 3.8)

$$\begin{Bmatrix} \Delta P_2 \\ \Delta P_4 \end{Bmatrix}^k = \begin{bmatrix} k_s + k_{bi} & -k_s \\ -k_s & k_s + k_{bj} \end{bmatrix}^k \cdot \begin{Bmatrix} \Delta d_2 \\ \Delta d_4 \end{Bmatrix}^k - \begin{Bmatrix} k_{bi} \cdot \Delta d_1 \\ k_{bj} \cdot \Delta d_3 \end{Bmatrix} \tag{3.54}$$

where it should be noted that the concrete displacement increments Δd_1 and Δd_3 are known from Eq. 3.50 and Step 2 of the global solution algorithm. Solving Eq. 3.54 for the force and displacement increment at node 4 yields

$$\begin{Bmatrix} \Delta P_4 \\ \Delta d_4 \end{Bmatrix}^k = \frac{1}{k_s} \begin{bmatrix} -(k_s + k_{bi}) & k_s \cdot (k_{bi} + k_{bj}) + k_{bi} \cdot k_{bj} \\ -1 & k_s + k_{bi} \end{bmatrix}^k \cdot \begin{Bmatrix} \Delta d_2 \\ \Delta d_4 \end{Bmatrix}^k - \begin{bmatrix} k_i \cdot \dfrac{k_s + k_{bj}}{k_s} & k_j \\ k_i & 0 \end{bmatrix} \cdot \begin{Bmatrix} \Delta d_1 \\ \Delta d_3 \end{Bmatrix} \tag{3.55}$$

which is written in compact form

$$\begin{Bmatrix} \Delta P_4 \\ \Delta d_4 \end{Bmatrix}^k = [Q]^k \cdot \begin{Bmatrix} \Delta d_2 \\ \Delta d_4 \end{Bmatrix}^k - [R]^k \cdot \begin{Bmatrix} \Delta d_1 \\ \Delta d_3 \end{Bmatrix} \tag{3.56}$$

For the transition from the k-th to the $(k+1)$-th element the following relations hold (Fig. 3.8)

$$\begin{Bmatrix} \Delta P_2 \\ \Delta d_2 \end{Bmatrix}^{k+1} = \begin{Bmatrix} -\Delta P_4 \\ \Delta d_4 \end{Bmatrix}^k = \begin{bmatrix} -1 & 0 \\ 0 & 1 \end{bmatrix} \cdot \begin{Bmatrix} \Delta P_4 \\ \Delta d_4 \end{Bmatrix} = [S] \cdot \begin{Bmatrix} \Delta P_4 \\ \Delta d_4 \end{Bmatrix} \tag{3.57}$$

The substitution of Eq. 3.56 into Eq. 3.57 yields

$$\begin{Bmatrix}\Delta P_2\\ \Delta d_2\end{Bmatrix}^{k+1} = [S]\cdot[Q]^k\cdot\begin{Bmatrix}\Delta d_2\\ \Delta d_4\end{Bmatrix}^k - [S]\cdot[R]^k\cdot\begin{Bmatrix}\Delta d_1\\ \Delta d_3\end{Bmatrix}^k \tag{3.58}$$

After realizing that the multiplication by matrix $[S]$ amounts to changing the signs of the first column of matrices $[Q]$ and $[R]$ Eq. 3.58 is simplified to

$$\begin{Bmatrix}\Delta P_2\\ \Delta d_2\end{Bmatrix}^{k+1} = [\overline{Q}]^k\cdot\begin{Bmatrix}\Delta P_2\\ \Delta d_2\end{Bmatrix}^k - [\overline{R}]^k\cdot\begin{Bmatrix}\Delta d_1\\ \Delta d_3\end{Bmatrix}^k \tag{3.59}$$

where the change of sign of the first column of $[Q]$ and $[R]$ results in $[\overline{Q}]$ and $[\overline{R}]$, respectively.

Eq. 3.59 relates the force and displacement increment at the beginning of steel element k+1 with the force and displacement increment at the beginning of steel element k. By applying Eq. 3.58 successively to elements k-1,k-2, ...,2,1 and combining the results the following transfer matrix relation results

$$\begin{aligned}\begin{Bmatrix}\Delta P_2\\ \Delta d_2\end{Bmatrix}^{k+1} &= [\overline{Q}]^k\cdot\begin{Bmatrix}\Delta P_2\\ \Delta d_2\end{Bmatrix}^k - [\overline{R}]^k\cdot\begin{Bmatrix}\Delta d_1\\ \Delta d_3\end{Bmatrix}^k\\ &= [\overline{Q}]^k\cdot[\overline{Q}]^{k-1}\cdot\begin{Bmatrix}\Delta P_2\\ \Delta d_2\end{Bmatrix}^{k-1} - [\overline{Q}]^k\cdot[\overline{R}]^{k-1}\cdot\begin{Bmatrix}\Delta d_1\\ \Delta d_3\end{Bmatrix}^{k-1} - [\overline{R}]^k\cdot\begin{Bmatrix}\Delta d_1\\ \Delta d_3\end{Bmatrix}^k\\ &= [\overline{Q}]^k\cdot[\overline{Q}]^{k-1}\ldots[\overline{Q}]^1\cdot\begin{Bmatrix}\Delta P_2\\ \Delta d_2\end{Bmatrix}^1 - [\overline{Q}]^k\cdot[\overline{Q}]^{k-1}\ldots[\overline{Q}]^2\cdot[\overline{R}]^1\cdot\begin{Bmatrix}\Delta d_1\\ \Delta d_3\end{Bmatrix}^1 - \ldots - [\overline{R}]^k\cdot\begin{Bmatrix}\Delta d_1\\ \Delta d_3\end{Bmatrix}^k\end{aligned} \tag{3.60}$$

After replacing k+1 with n in Eq. 3.60 and applying Eq. 3.56 for element n the following relation between the forces and displacements at the two ends of the reinforcing bar results

$$\begin{Bmatrix}\Delta P_4\\ \Delta d_4\end{Bmatrix}^n = [Q]^n\cdot[\overline{Q}]^{n-1}\ldots[\overline{Q}]^1\cdot\begin{Bmatrix}\Delta P_2\\ \Delta d_2\end{Bmatrix}^1 - [Q]^n\cdot[\overline{Q}]^{n-1}\ldots[\overline{Q}]^2\cdot[\overline{R}]^1\cdot\begin{Bmatrix}\Delta d_1\\ \Delta d_3\end{Bmatrix}^1 - \ldots - [\overline{R}]^n\cdot\begin{Bmatrix}\Delta d_1\\ \Delta d_3\end{Bmatrix}^n \tag{3.61}$$

In Eq. 3.61 the concrete displacement increments are known from Eq. 3.50.

One boundary condition is known at each end of the reinforcing bar. After assuming the second boundary condition at the starting end, Eq. 3.61 yields the force and displacement increment at the other end of the reinforcing bar. Since one condition is known at that end, the initial assumption needs to be corrected until the known boundary condition at the far end is satisfied.

It should be noted that the transfer matrix method is applied during the correction phase of the global solution algorithm. Consequently, the transfer matrix relations in Eq. 3.61 are linear, since no updating of the bond and steel stiffness takes place during the correction phase which is based on the initial stiffness method. Thus, Eq. 3.61 can be solved very rapidly through a series of multiplications and no iterations are required. An advantage of the transfer matrix method is its numerical stability in connection with the cyclic bond-slip model of Section 2.4.1. This will be discussed further in the correlation studies of Chapter 4.

The satisfaction of equilibrium of the reinforcing bar by the transfer matrix method of Eq. 3.61 yields the steel displacement increments. Since the concrete displacement increments at the ends of the bar are also known from Eq. 3.50, the relative displacements can be readily determined. The state determination of the steel and bond elements can now be undertaken yielding the new steel and bond forces and the updated stiffness matrices. The latter are only needed at the beginning of a new load step, when the stiffness matrix of the structure is updated. The substitution of the new steel and bond forces in Eq. 2.66 yields the equivalent nodal forces at the global degrees of freedom. These forces are subtracted from the applied load increments to yield the unbalanced forces. The process continues until the convergence criterion is satisfied.

3.4.4 Convergence Criterion

The criterion for measuring the convergence of the iterative solution is based on the accuracy of satisfying the global equilibrium equations or on the accuracy of determining the total displacements. The accuracy of satisfying the global equilibrium equations is controlled by the magnitude of the unbalanced nodal forces. The accuracy of the node displacements depends on the magnitude of the additional displacement increment after each iteration. The latter convergence criterion is used in this study. This can be expressed as

$$E_d = \frac{\left[\sum_j (\Delta d_j^i)^2\right]^{\frac{1}{2}}}{\left[\sum_j (d_j^i)^2\right]^{\frac{1}{2}}} \leq \text{TOLER} \tag{3.62}$$

where the summation extends over all degrees of freedom j, d_j is the displacement of degree of freedom j, Δd_j^i is the corresponding increment after iteration i and TOLER is the specified tolerance.

In the nonlinear analysis of RC structures the load step size must be small enough so that unrealistic "numerical cracking" does not take place. These spurious cracks can artificially alter the load transfer path within the structure and result in incorrect modes of failure. Crisfield (1982) has shown that such numerical disturbance of the load transfer path after initiation of cracking can give rise to alternative equilibrium states and, hence, lead to false ultimate strength predictions. In order to avoid such problems after crack initiation the load is increased in steps of 2.5-5.0% of the ultimate load of the member.

The failure load is assumed to occur at a load level for which a large number of iterations are required for convergence. This means that very large strain increments take place during this step and that equilibrium cannot be satisfied under the applied loads. Obviously, the maximum number of iterations depends on the problem and the specified tolerance, but a maximum of 30 iterations seems adequate for a tolerance of 1%. This is the limit in the number of iterations selected in this study.

CHAPTER 4
APPLICATIONS

4.1 Introduction

A number of correlation studies are conducted in this chapter with the objective of establishing the ability of the proposed model to simulate the response of reinforced concrete beams, slabs and beam-column joint subassemblages. In order to independently test the reinforcing steel model with bond-slip, the response of anchored reinforcing bars under monotonic pull-out and cyclic push-pull loads is also studied. Even though cyclic loading is outside the scope of this study, the cyclic behavior of reinforcing bars is presented in order to demonstrate the capabilities of the proposed numerical solution scheme and in order to highlight the pronounced effect of cyclic bond-deterioration on the hysteretic response of RC members, which is the subject of a follow-up study.

4.2 Anchored Reinforcing Bar Under Monotonic and Cyclic Loads

Viwathanatepa, Popov and Bertero (1979b) tested several anchored reinforcing bars simulating anchorage and loading conditions in interior beam-column joints of moment resisting frames which are subjected to a combination of gravity and high lateral loads. #6, #8 and #10 reinforcing bars were anchored in well confined concrete blocks and were subjected to monotonic pull-out at one end, monotonic pull-out at one end with simultaneous push-in at the other (called push-pull) and cyclic push-pull.

Two specimens are selected for comparison with the proposed reinforcing steel model with bond-slip. The first specimen is an anchored #8 bar in a well confined block of 25 in. width, which corresponds to an anchorage length of 25 bar diameters. This specimen was subjected to a monotonic pull-out under displacement control at one end only. The second specimen also involves a #8 reinforcing bar with identical dimensions which was subjected to a cyclic push-pull loading with gradually increasing end slip value. Both specimens have been the subject of earlier analytical correlation studies by Viwathanatepa et al. (1979b), Ciampi et al. (1982), Yankelevky (1985) and Filippou (1986). The material properties of concrete and reinforcing steel, as reported in Table 2.1 of the report by Viwathanatepa et al. (1979b), are as follows: the concrete cylinder strength is 4,700 psi for the specimen under monotonic pull-out and 4,740 psi for the specimen under cyclic push-pull. The yield strength of the reinforcing steel is 68 ksi and the yield strain is 0.23%.

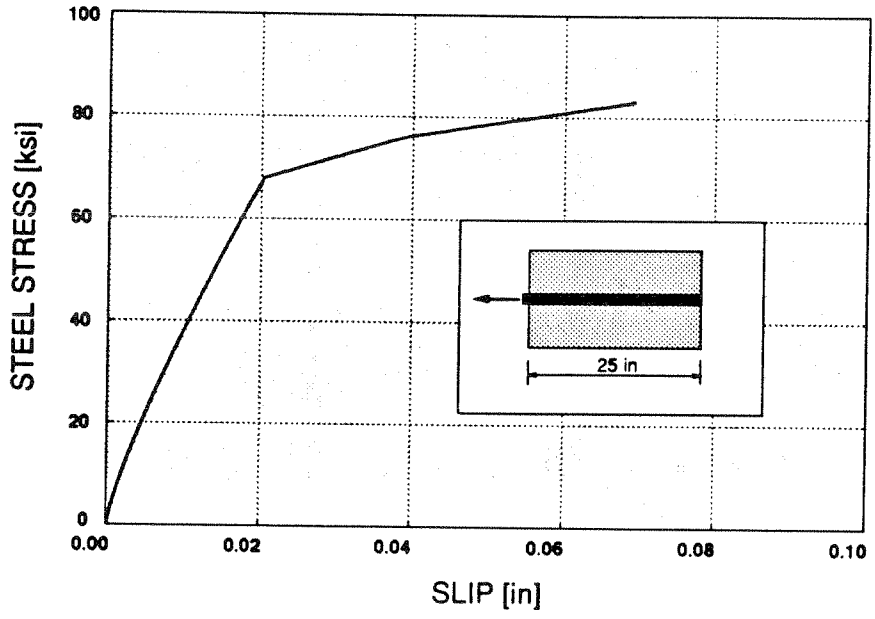

Fig. 4.1 ***Stress-Slip Response of Anchored Reinforcing Bar Under Monotonic Pull-Out Loading***

In the monotonic pull-out test the bilinear steel model in Fig. 2.14 of Section 2.3 is used. The strain hardening modulus is equal to 411 ksi, which corresponds to 1.4% of Young's modulus. In the cyclic push-pull test the model of Menegotto-Pinto, as modified by Filippou et al. (1983), is used. In both specimens the refined bond-slip model in Fig. 2.19 of Section 2.4 is used. The parameters of the model are equal to those used by Filippou et al. (1983) and Filippou (1986) in earlier investigations, namely: $u_1 = 0.02756$in, $u_2 = 0.07874$in, $u_3 = 0.2756$in, $\tau_1 = 2350$psi and $\tau_3 = 870$psi (Fig. 2.19). In the study by Ciampi et al. (1982) the bond-slip relation was modified in the outer unconfined portions of the anchorage length. By contrast, in the present study the same bond stress-slip relation is used along the entire anchorage length for the sake of simplicity, since the hysteretic behavior is not the focus of the present study. Under cyclic loading conditions this assumption leads to underestimation of the bond resistance at the push-in end of the reinforcing bar. 25 steel elements of 1 in length each were used in modeling the anchored reinforcing bar.

Fig. 4.1 shows the relation between pull-out slip and steel stress at one end of the reinforcing bar under monotonic pull-out loading. Figs. 4.2a-d show the distribution of steel stresses along the anchorage length of the reinforcing bar at different loading stages. The experimental results are compared with the analytical results of Viwathanatepa et al. (1979b), Yankelevsky (1985) and those of the present study. The result of the present study show the best agreement, particularly, with

increasing load. It should be noted that the model of Yankelevsky (1985) does not allow for yielding of the reinforcing steel. The results by Viwathanatepa et al. (1979b) are from a linear finite element analysis, since no stress distributions are presented for the nonlinear model proposed in that study.

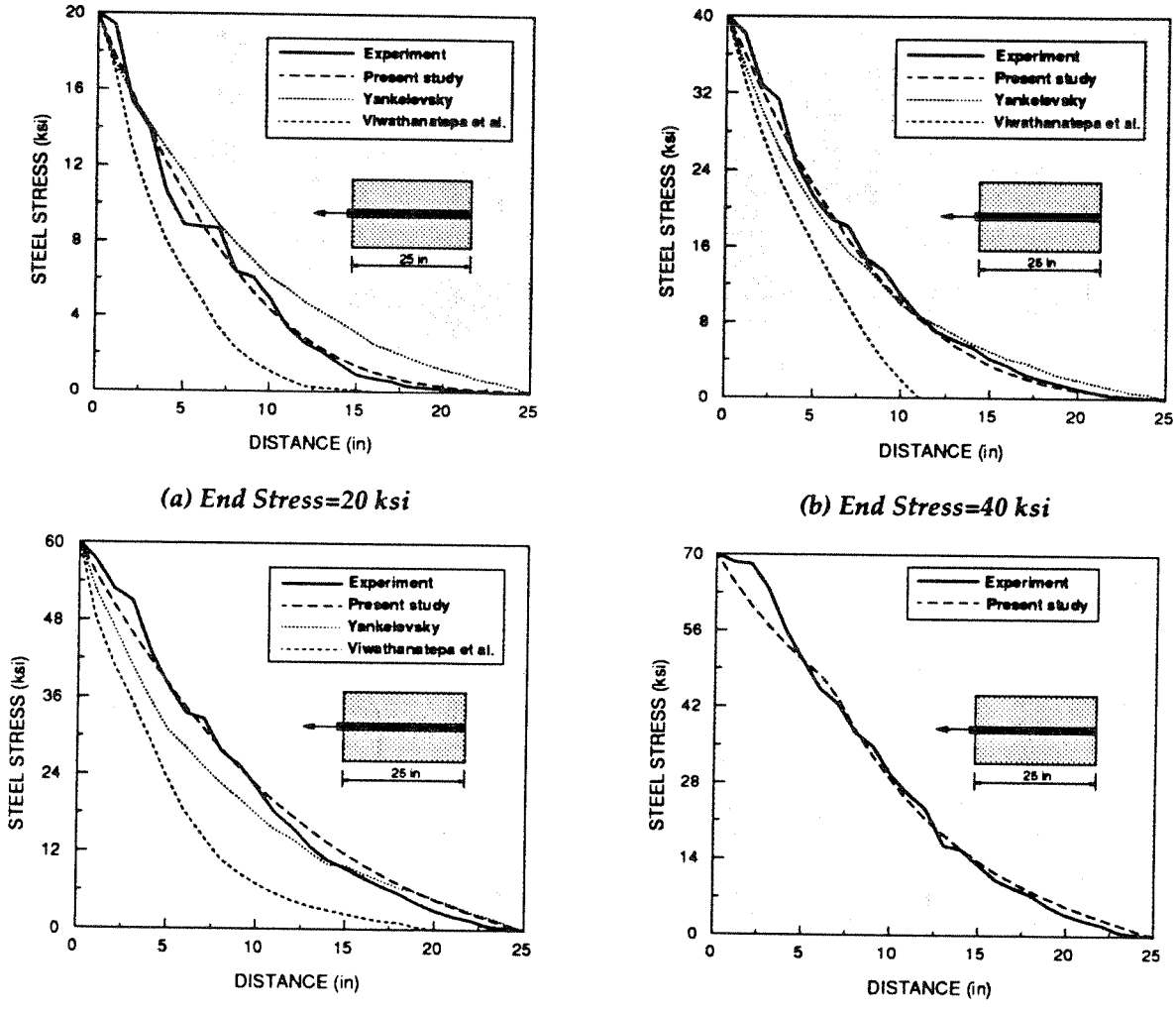

(a) End Stress=20 ksi

(b) End Stress=40 ksi

(c) End Stress=60 ksi

(d) End Stress=70 ksi

Fig. 4.2 Stress Distribution Along Anchored Reinforcing Bar

Figs. 4.3a and b show the end stress-slip relation of the reinforcing bar under cyclic push-pull loading. Fig. 4.3a shows the cycles before yielding of the reinforcement and Fig. 4.3b shows the entire response. The corresponding experimental data are shown in Figs. 4.4a and b. The steel stress distributions along the anchorage length of the reinforcing bar are shown in Figs. 4.5a-f. The experimental results are compared with the analytical results of Viwathanatepa et al. (1979b), Yankelevsky (1985) and those of the present study. The results of the proposed model show excellent agreement in the early cycles in Figs. 4.5a-f. However, the comparison of the overall response in Figs. 4.3 and 4.4 shows discrepancies between the present model and the experimental data as the

loading increases. Two factors contribute to this: (a) the model is tested under load controlled conditions, while the specimen was subjected to displacement controlled testing, and (b) the assumption that the bond stress-slip relation is the same along the anchorage length of the bar is not reasonable for cycles which induce significant bond damage.

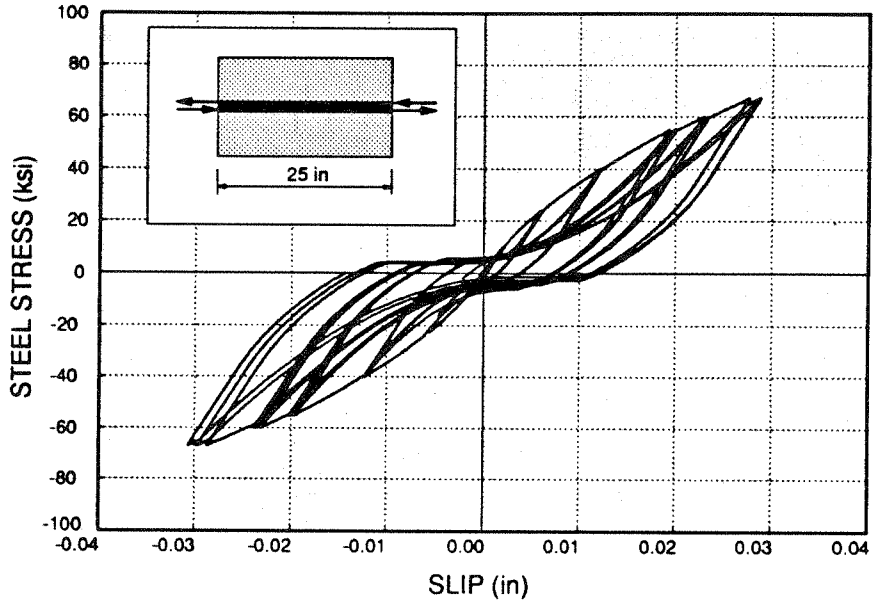

(a) Load Cycles Before Yielding of Reinforcing Steel

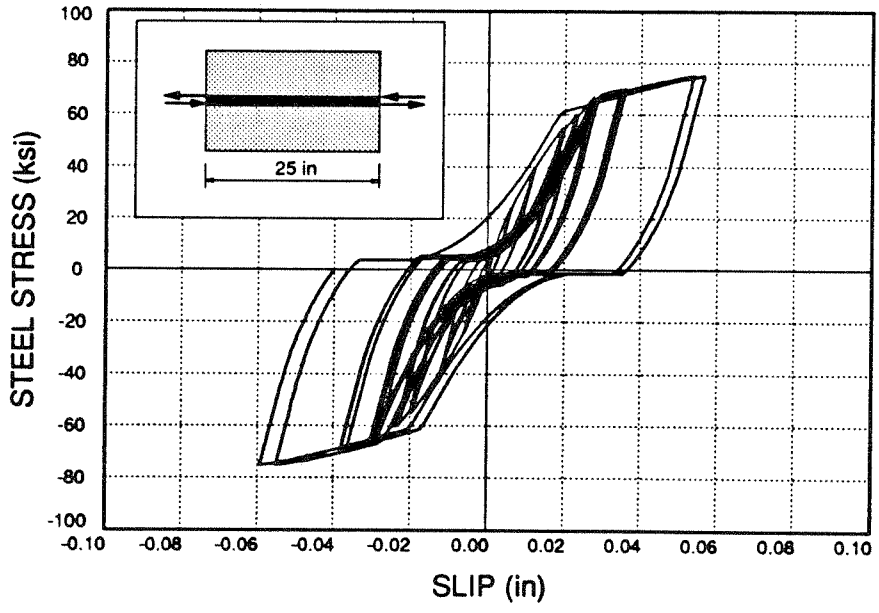

(b) Load Cycles After Yielding of Reinforcing Steel

Fig. 4.3 Stress-Slip Response of Anchored Reinforcing Bar Under Cyclic Push-Pull. Analytical Results.

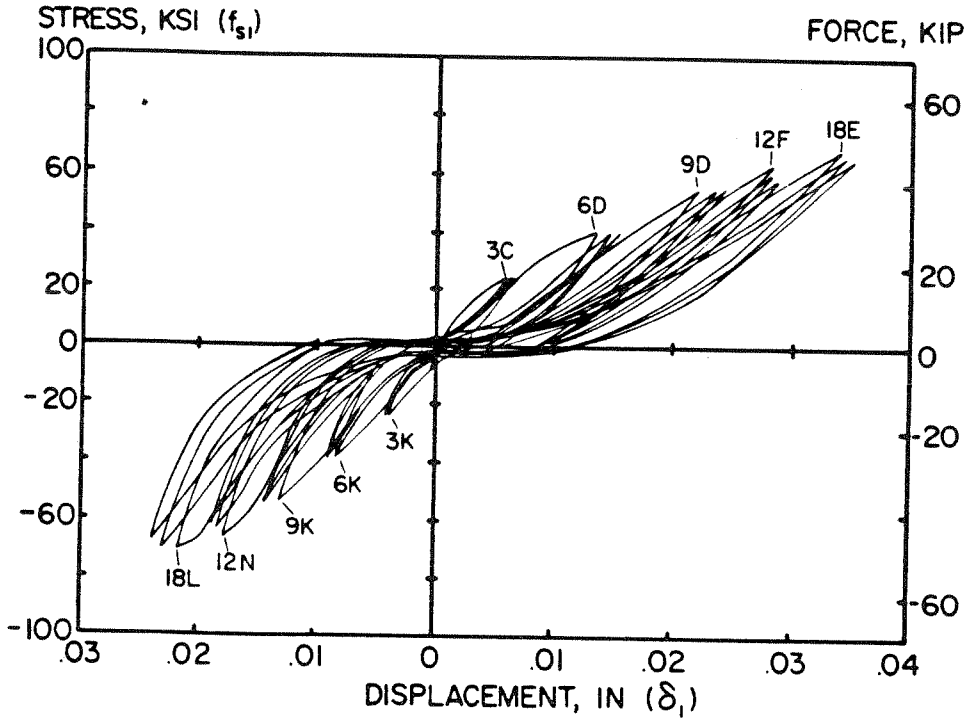

(a) Load Cycles Before Yielding of Reinforcing Steel

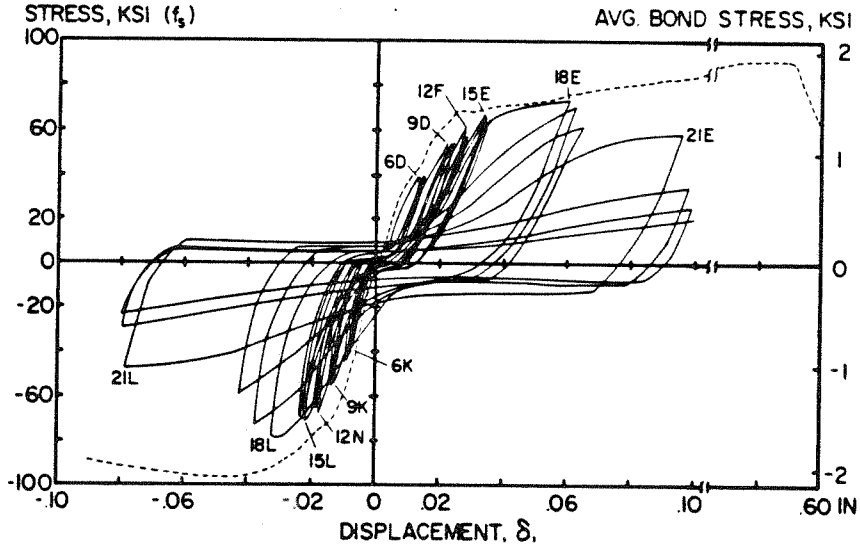

(b) Load Cycles After Yielding of Reinforcing Steel

Fig. 4.4 Stress-Slip Response of Anchored Reinforcing Bar Under Cyclic Push-Pull. Experimental Results.

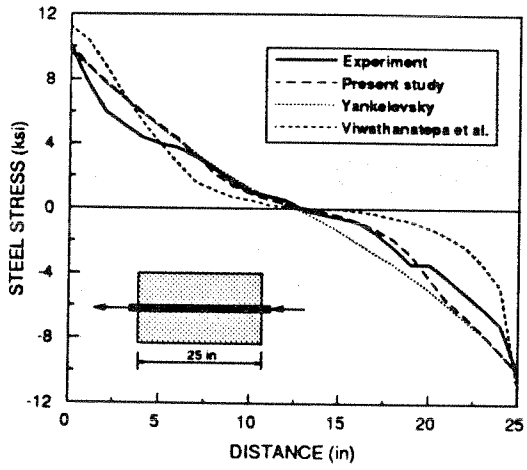

(a) First Cycle

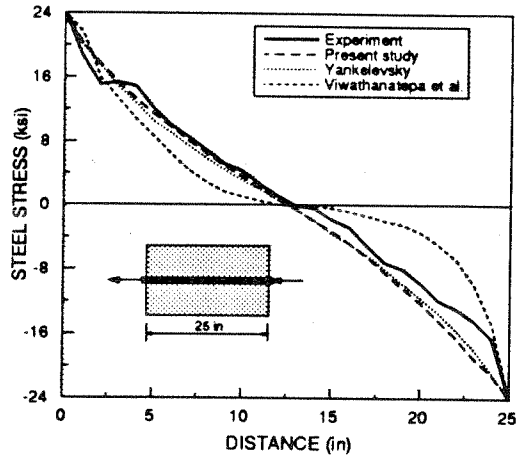

(b) Fourth Cycle

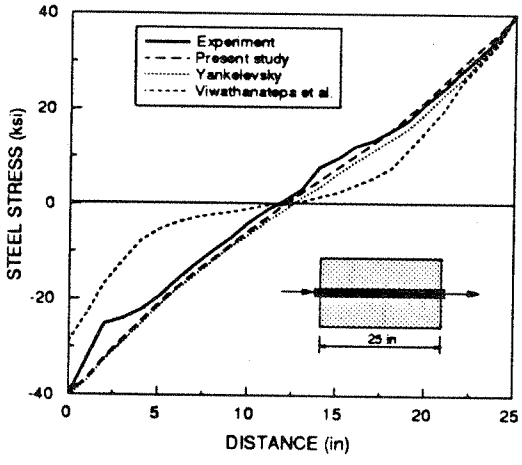

(c) Seventh Cycle

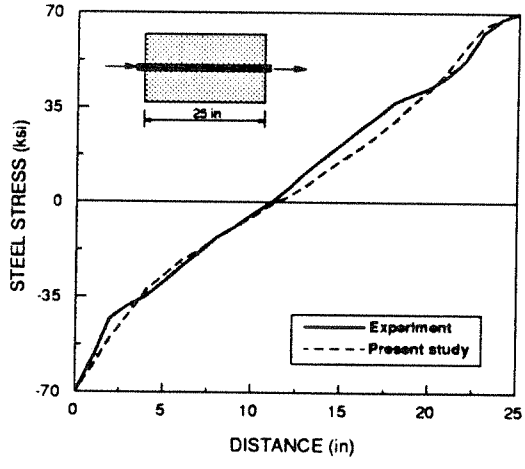

(d) First Post-Yield Cycle

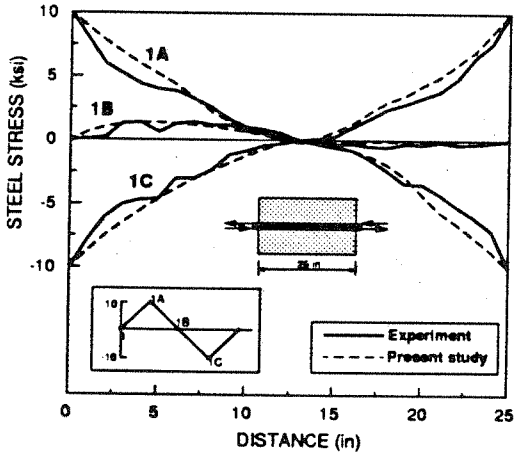

(e) Complete First Cycle

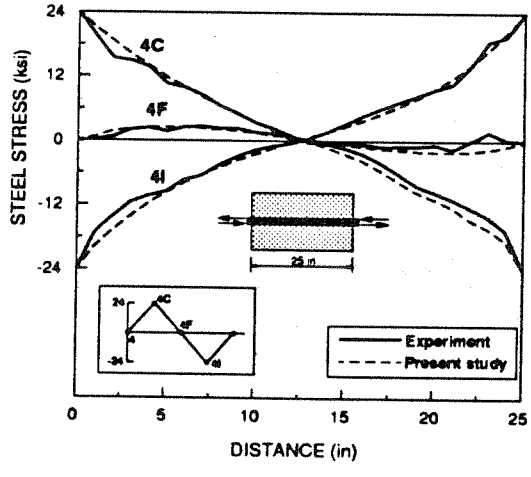

(f) Complete Fourth Cycle

Fig. 4.5 Stress Distribution Along Anchored Reinforcing Bar Under Cyclic Push-Pull Loading

It is concluded that the proposed reinforcing steel model with bond-slip can describe quite well the response of anchored reinforcing bars under monotonic and cyclic loading conditions. It should be noted that the analytical results of the proposed model in Figs. 4.1 are obtained with both solution methods of Chapter 2, namely, the direct solution method and the transfer matrix method. The direct solution method is, in general, more economical, particularly, is advantage is taken of the tridiagonal stiffness matrix of the reinforcing bar with bond-slip. The load step size required for convergence is, however, larger in the transfer matrix method, so that both methods seem to require about the same amount of time for determining the entire load-displacement response of Fig. 4.4. Further comparison studies of the computer time of these two methods are needed, before a definitive statement can be made.

EXAMPLES		MATERIAL PROPERTIES				
		E_c [ksi]	E_s [ksi]	f_c [ksi]	f_y [ksi]	ρ [%]
BEAMS	J-4	3800	29500	4.82	44.9	0.99
	A-1	3367	31600	3.49	80.5	1.53
	T1MA	3860	28200	4.60	46.0	0.62
BEAM-COLUMN JOINT		3900	28770	4.97	71.4	1.22
SLABS	McNeice	4150	29000	5.50	40.0	0.85
	B7	4000	30000	5.15	50.0	1.00

Note: The material properties of the reinforcing steel for beam A-1 and for the beam-column joint are for #9 and #6 bars, respectively. Other material properties are as follows: $G_f = 0.5$ lb/in, $f_t = 5\sqrt{f_c}$, $\nu_c = 0.167$ and $\nu_s = 0.333$.

Table 4.1 Material Properties Used in Applications

4.3 Reinforced Concrete Beams

Three simply supported reinforced concrete beams have been investigated. These beams are specimen J-4 tested by Burns and Siess (1962), specimen A-1 tested by Bresler and Scordelis (1963) and specimen T1MA tested by Gaston, Siess and Newmark (1972). In these case studies the concrete was modeled by 8-node serendipity plane stress elements with 3x3 Gauss integration and the reinforcement was modeled by the 2-node truss element described in Section 2.3. In all studies the bond-slip effect is taken into account with the bond link element described in Section 2.4. The material properties of the three test specimens are summarized in Table 4.1

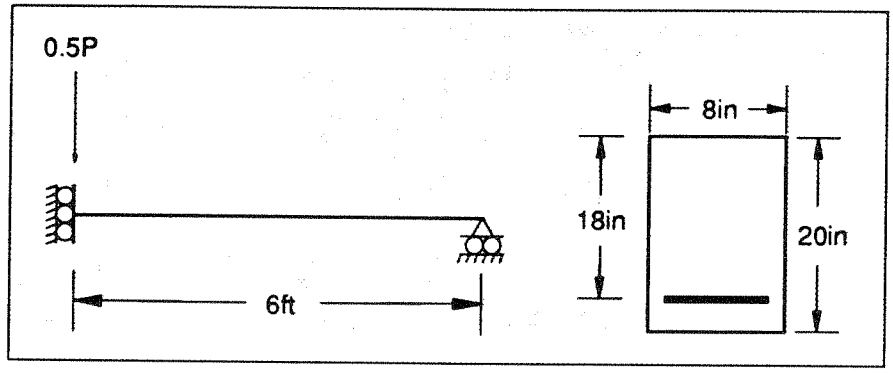

Fig. 4.1 Configuration of Beam J-4

Specimen J-4 consists of a simply supported beam with a span of 12 ft (3.7 m) which was subjected to a concentrated load at midspan. The geometry and the cross section of beam J-4 are shown in Fig. 4.1 and the material properties are summarized in Table 4.1.

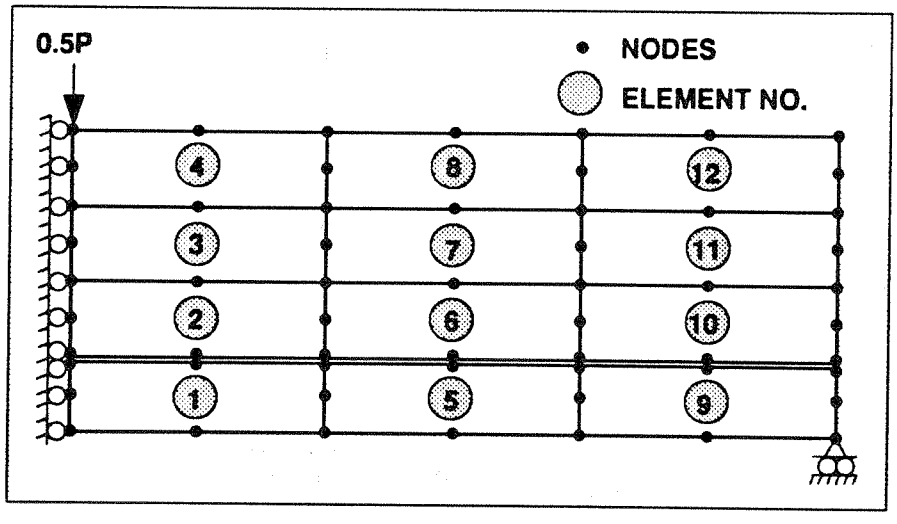

Fig. 4.2 Finite Element Idealization of Beam J-4

The finite element model in Fig. 4.2 represents only half of the structure taking advantage of the symmetry in geometry and loading. The finite element discretization, the arrangement of the reinforcement, the loading and support conditions are shown in Fig. 4.2. The parameters of the bond stress-slip relation in Fig. 2.17 are assumed as follows: $d_{s1} = 0.0007854$in, $d_{s2} = 0.00589$in, $\tau_1 = 286$psi and $\tau_2 = 572$psi. These values are derived from the material properties in Table 4.1 based on the recommendations of Eligehausen et al. (1983). The tension stiffening effect is taken into account by the model proposed in Section 2.2.3.3. The correlation between the measured load-displacement curve of the beam and the analytical results which include the effects of tension stiffening and bond-slip is shown in Fig. 4.3. The results are also compared with those of an earlier study by Barzegar and Schnobrich (1986), who included only the tension stiffening effect by determining the slope of the strain softening region according to Hillerborg's model (Hillerborg et al. 1976).

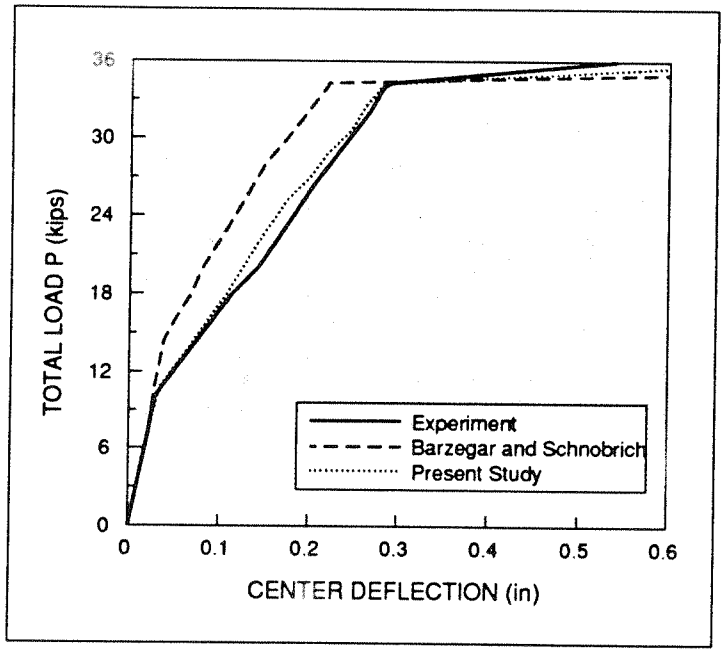

Fig. 4.3 Load-Deflection Relationships of Beam J-4

In order to establish the contribution of the tension stiffening and the bond-slip effect to the structural response a series of studies on beam J-4 were conducted. These studies also aim at identifying the effect, if any, of finite element mesh size, tensile strength of concrete and the cracked shear constant value. The results of these studies are discussed below.

In order to study the effect of finite element mesh size on the analytical results three different mesh configurations were investigated, as shown in Fig. 4.4. In all configurations the number of elements through the depth of the member remained the same and only the element size in the span direction was progressively reduced.

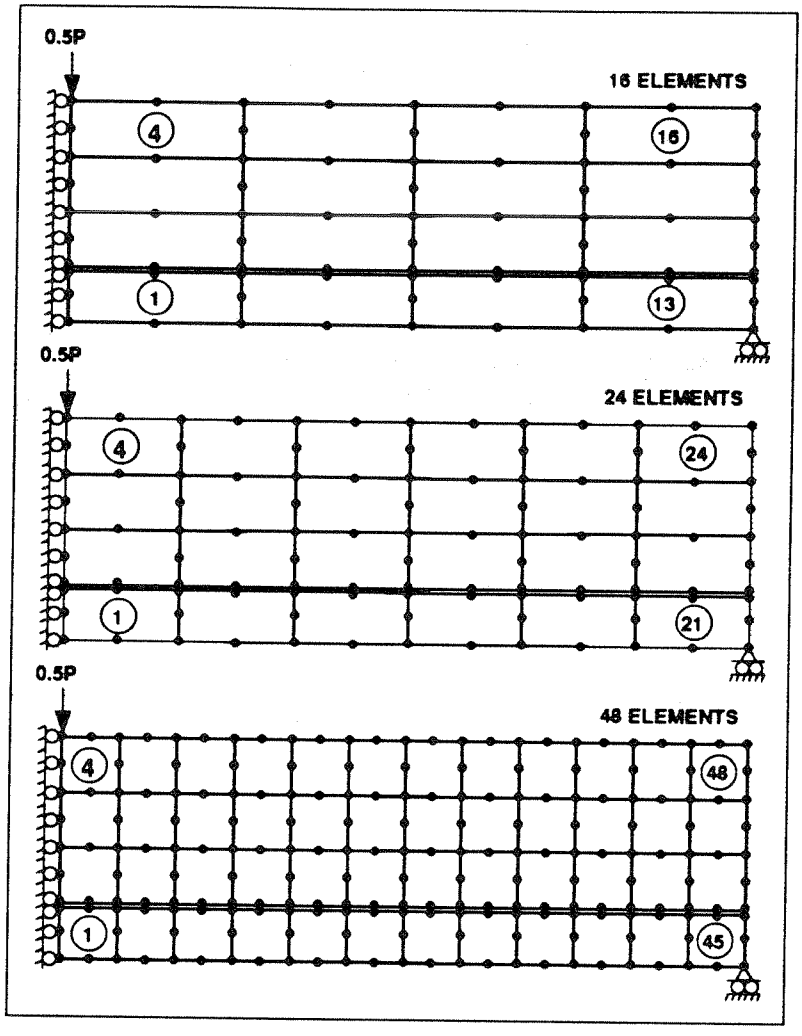

Fig. 4.4 Finite Element Mesh Configurations Used

The effect of finite element mesh size is studied for the three tension-stiffening models discussed in Section 2.2.3.2. The results in Figs. 4.5a-c indicate that all tension-stiffening models exhibit satisfactory behavior and lead to response predictions which are essentially independent from the finite element mesh size. The size dependence is more pronounced in Hillerborg's model, while the crack band theory and the model proposed in this study show a very satisfactory objectivity of the results. When comparing, however, the results of the crack band theory and Hillerborg's model with those of the tension-stiffening model proposed in this study, it is concluded that the load-deflection behavior of the former models is stiffer than that of the present model, which as shown in Fig. 4.3, matches the experimental behavior very well. This can be attributed to the assumption of those models that the microcracks are uniformly distributed over the entire finite element.

If the tension stiffening effect is not included in the model, there is a marked dependence of the analytical results on the finite element mesh size (Fig. 4.5d). The load-deflection curves exhibit more flexible response with increasing grid refinement. Thus finite element models which are based on the tensile strength of concrete and not on a fracture energy criterion produce results which strongly depend on the analyst's choice of mesh configuration and can lead to erroneous estimates of structural stiffness. This fact corroborates earlier findings by several investigators (Bazant and Cedolin 1983; Reinhardt 1986).

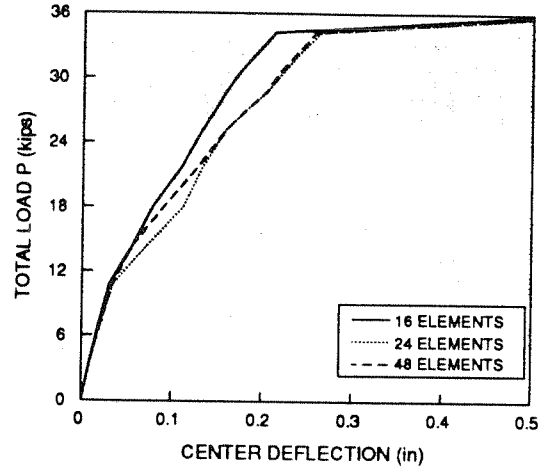

Fig. 4.5a Mesh Size Effect (Hillerborg's Model)

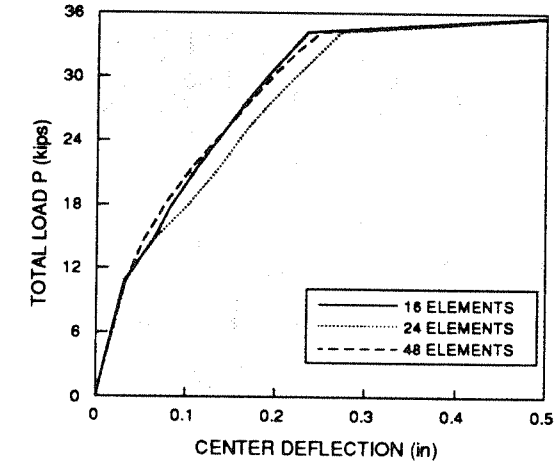

Fig. 4.5b Mesh Size Effect (Crack Band Model)

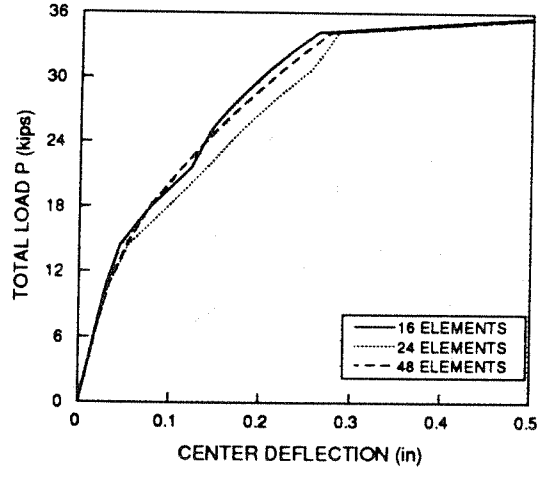

Fig. 4.5c Mesh Size Effect (Proposed Model)

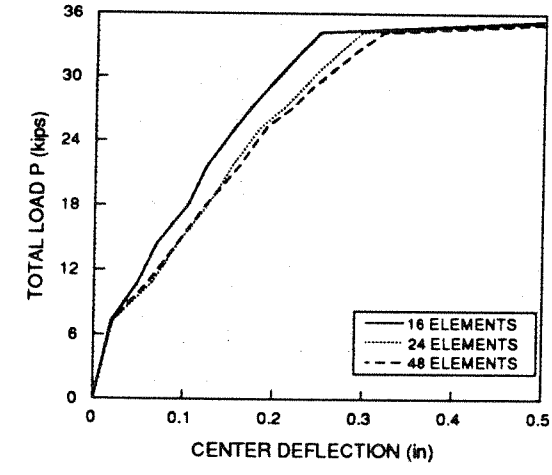

Fig. 4.5d Mesh Size Effect (no Tension Stiffening)

The models of tension-stiffening and bond slip described in Chapter 2 reveal that tension-stiffening has the opposite effect than bond-slip on the load-displacement response of the finite element model of the structure. One way of including the effect of tension-stiffening between cracks is to **increase** the stiffness of the reinforcing steel model. On the other hand bond slip **reduces** the stiffness of the reinforcing steel model, as is clearly reflected in the coefficient of the steel stiffness

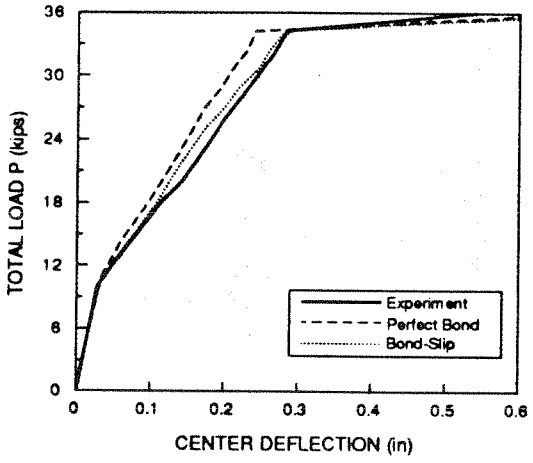

Fig. 4.6a Tension Stiffening Effect of Beam J-4

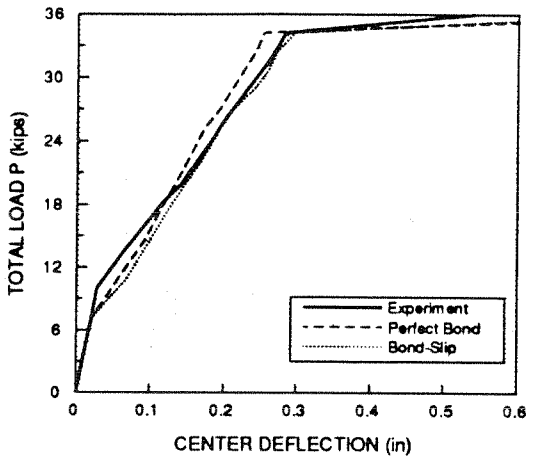

Fig. 4.6b Bond-Slip Effect of Beam J-4

matrix in Eqs. 2.68 and 2.69. To identify the relative contribution of each effect four different analyses are performed. In Fig. 4.6a the effect of tension stiffening is included in both analytical results. The response which is depicted by the long-dash line excludes the effect of bond-slip, while the response depicted with the dotted line includes this effect. It is clear from the comparison of these results with the experimental data shown by the solid line that the inclusion of both effects yields a very satisfactory agreement of the model with reality. Fig. 4.6b shows two analytical results which exclude the effect of tension-stiffening. In this case the inclusion of bond-slip (dotted line) produces a slightly more flexible response than the experiment, while the exclusion of bond-slip produces a slighter stiffer response. The comparison of Fig. 4.6a with Fig. 4.6b illustrates why some investigators have concluded that neither tension-stiffening nor bond-slip is important in the analysis, provided that the right size of finite element mesh is used.

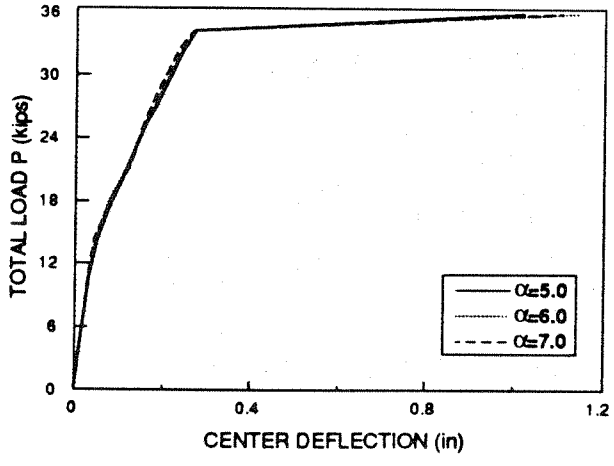

Fig. 4.7 Effect of Tensile Strength of Concrete

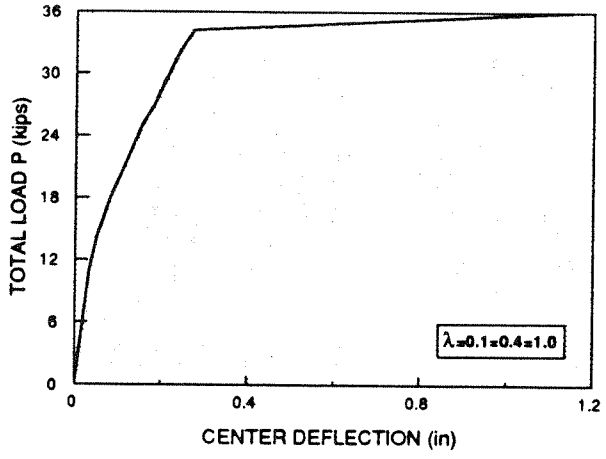

Fig. 4.8 Effect of Cracked Shear Constant

Fig. 4.7 shows the influence of the tensile strength of concrete on the response of the beam specimen. In Fig. 4.7 the tensile strength of concrete, which is determined from the relation $f_t = \alpha \cdot \sqrt{f_c}$, is varied between $f_t = 5\sqrt{f_c}$ and $f_t = 7\sqrt{f_c}$. It is apparent that the tensile strength only affects the load magnitude at initial cracking and the load magnitude at the formation of a stable crack configuration. Since, the load magnitude at initial cracking is relatively low, the effect of tensile strength on the overall response is negligible. Moreover, if the tensile fracture strain ε_o is adjusted to yield the same fracture energy according to Eq. 2.14 of the proposed model, then the effect of tensile strength on the response is reduced even further.

Fig. 4.8 shows that the effect of the cracked shear constant λ is negligible in the case of slender members subjected to bending, since most of the member is in the stress state of compression-compression or tension-tension and only a small portion of the structure near the supports is in a stress state of tension-compression. It is only in the tension-compression region of the biaxial stress space in Fig. 2.2 that the coupling between normal and shear strains, which is represented by the cracked shear constant λ, plays an important role. While this coupling effect is negligible in the case of slender beams in bending, it becomes significant in the analysis of shear walls and deep beams.

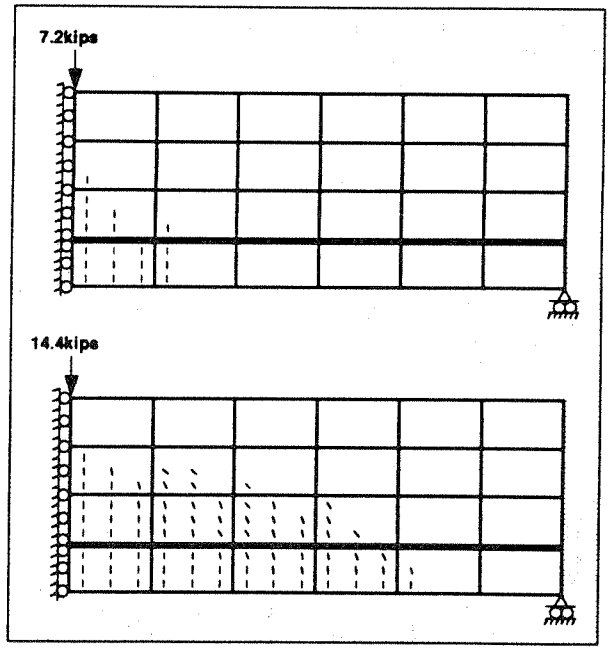

Fig. 4.9 Crack Propagation in Beam J-4

The crack prediction and crack propagation in beam J-4 at two load stages is shown in Fig. 4.9. It is evident that the response of this specimen is dominated by diagonal tension cracking in good agreement with the experimental evidence.

The next specimen which is investigated is beam A-1 tested by Bresler and Scordelis (1963). The geometry and cross section dimensions of beam A-1 are presented in Fig. 4.10, while Fig. 4.11 shows the finite element model of this structure. The material properties of concrete and steel are summarized in Table 4.1. The bond stress-slip relation and any other material properties not specifically mentioned in Table 4.1 are the same as those used in the analysis of beam J-4, since the concrete composition and strength of the two specimens is not much different. Since Table 4.1 only contains the steel properties of the bottom longitudinal steel of specimen A-1 (#9 bars), the following steel properties are assumed for the top steel and the transverse reinforcement: $E_s = 29200$ ksi and $f_y = 50.1$ ksi for #4 bars as top longitudinal steel and $E_s = 27500$ ksi and $f_y = 47.2$ ksi for #2 bars as transverse reinforcement.

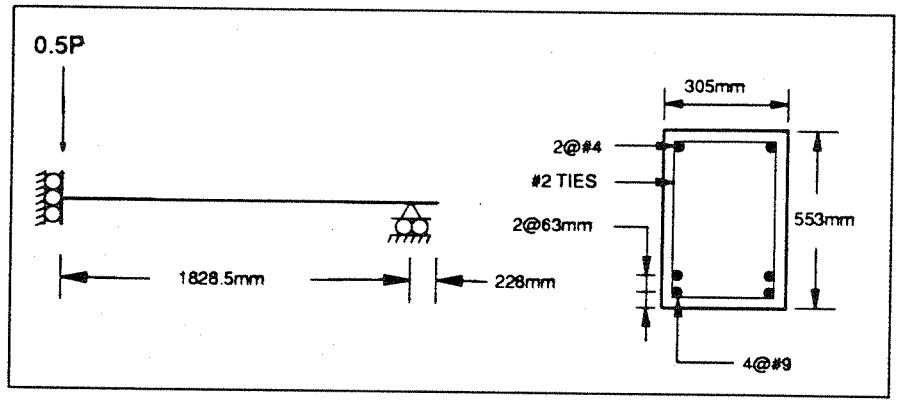

Fig. 4.10 Configuration of Beam A-1

Fig. 4.12 compares the analytical results with the measured load-displacement response of beam A-1. Very satisfactory agreement between analysis and experiment is observed. The analytical results by Adeghe and Collins (1986) are also shown in Fig. 4.12. Since Adeghe and Collins did not account for the effect of bond slip in their study, the comparison of analytical predictions demonstrates the significance of this effect in the load-displacement response of a heavily reinforced specimen, such as beam A-1.

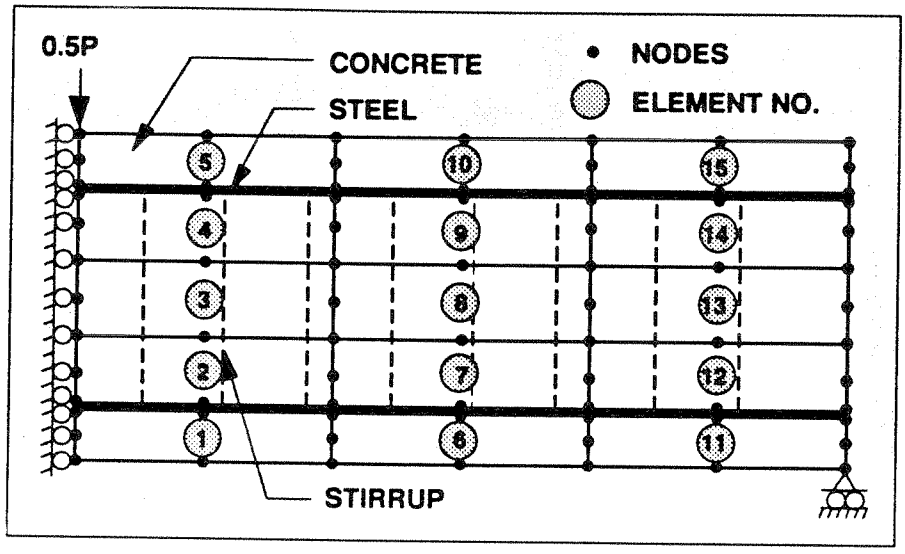

Fig. 4.11 Finite Element Idealization of Beam A-1

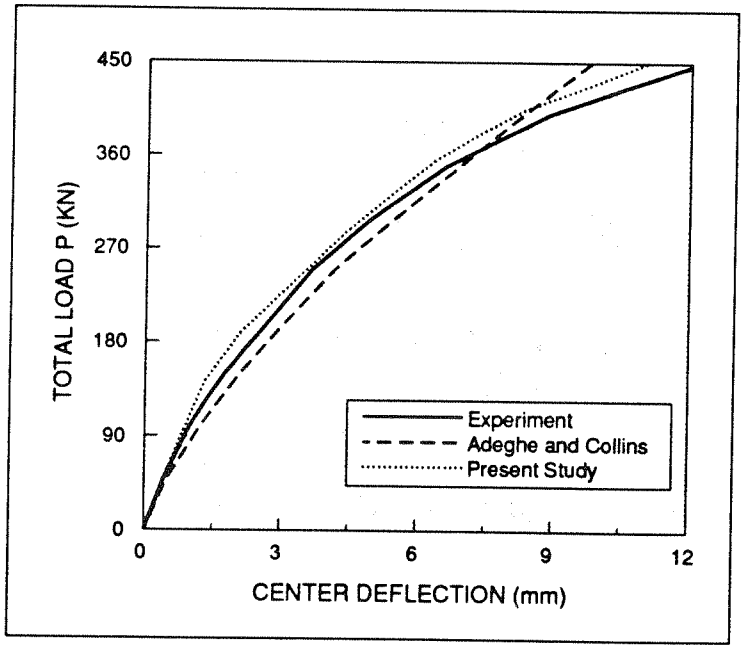

Fig. 4.12 Load-Deflection Relationships of Beam A-1

To identify the relative contribution of each effect four different analyses are also performed for this specimen. In Fig. 4.13a the effect of tension stiffening is included in both analytical results. The response which is depicted by the long-dash line excludes the effect of bond-slip, while the response depicted with the dotted line includes this effect. It is clear from the comparison of these

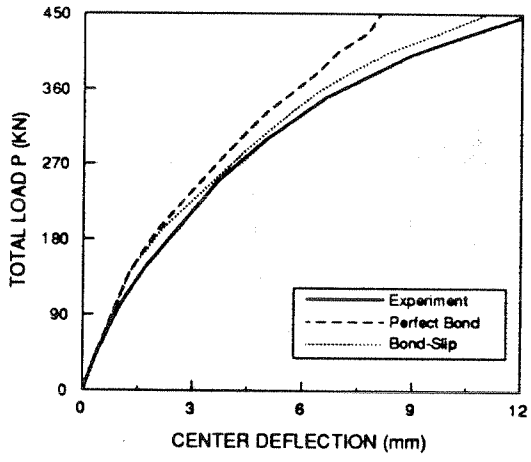

Fig. 4.13a Tension Stiffening and Bond-Slip Effect in Beam A-1

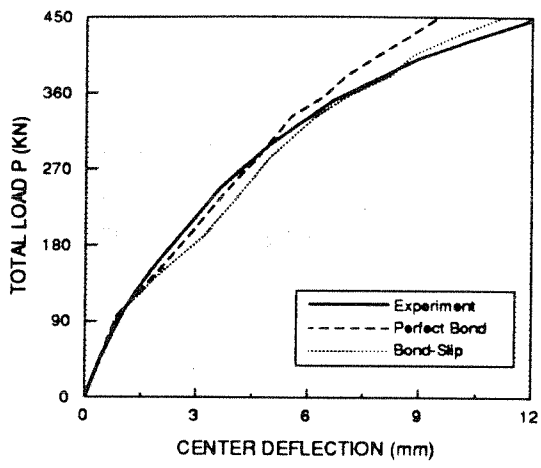

Fig. 4.13b Bond-Slip Effect without Tension Stiffening in Beam A-1

results with the experimental data shown by the solid line that the inclusion of both effects yields a very satisfactory agreement of the model with reality. Fig. 4.13b shows two analytical results which exclude the effect of tension-stiffening. In this case the inclusion of bond-slip (dotted line) produces a slightly more flexible response than the experiment, while the exclusion of bond-slip produces a slighter stiffer response. Figs. 4.13a and b show that the contribution of bond-slip to the load-displacement response of the specimen increases with the load. Near the ultimate strength of the beam the magnitude of the bond-slip contribution to the load-displacement response is almost twice that of the tension-stiffening effect, which is of opposite sign. By contrast, in the lightly reinforced beam specimen J-4 in Figs. 4.6a and b the magnitude of the bond-slip contribution to the load-displacement response is comparable to that of the tension-stiffening effect, so that these two effects practically cancel each other (long-dashed line in Fig. 4.6b).

The studies of beam specimens J-4 and A-1 show that the inclusion of, both, tension-stiffening and bond-slip effect, yields excellent agreement of the analytical results with the experiments. In lightly reinforced beams these two effects are of comparable importance and can cancel each other at certain stages of the load history. This does not happen over the entire response, since gradual bond damage leads to an increasing bond-slip contribution with increasing load. The bond-slip effect is more marked in heavily reinforced beams, such as specimen A-1, where it outweighs the effect of tension-stiffening.

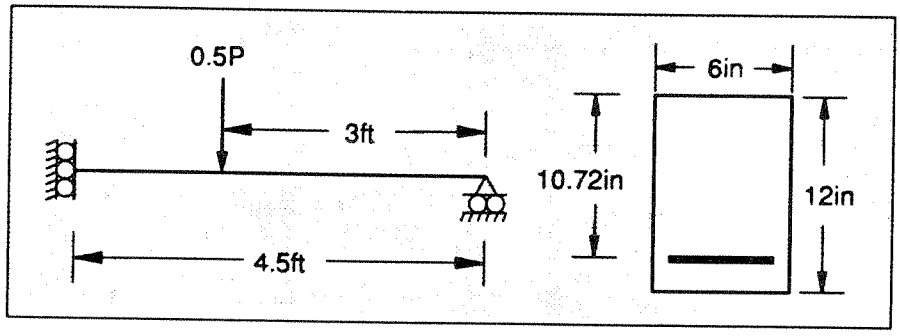

Fig. 4.14 Configuration of Beam T1MA

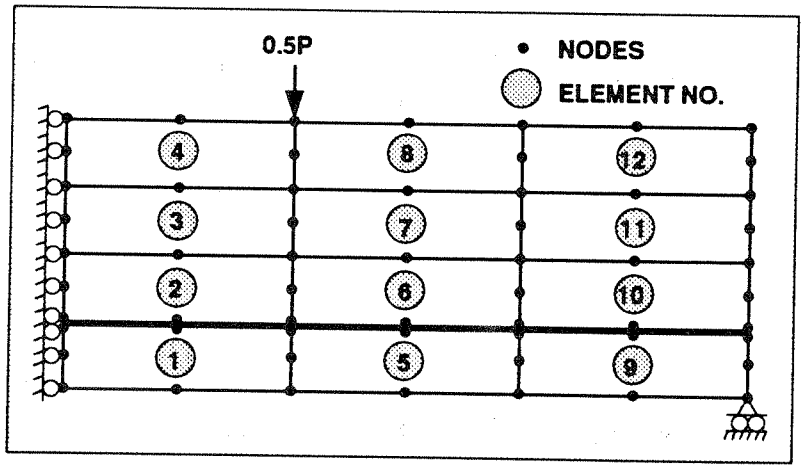

Fig. 4.15 Finite Element Idealization of Beam T1MA

Finally, the predictions of the model are compared with the measured response of specimen T1MA tested by Gaston et. al (1972). This specimen is also under-reinforced. Fig. 4.14 shows the geometry, the dimensions of the cross section, the boundary conditions and the loading arrangement of the specimen. Fig. 4.15 shows the finite element model of the structure. As with the previous test specimens only half of the structure needs to be modeled, because of symmetry in geometry and loading arrangement. The material properties are summarized in Table 4.1. The bond stress-slip

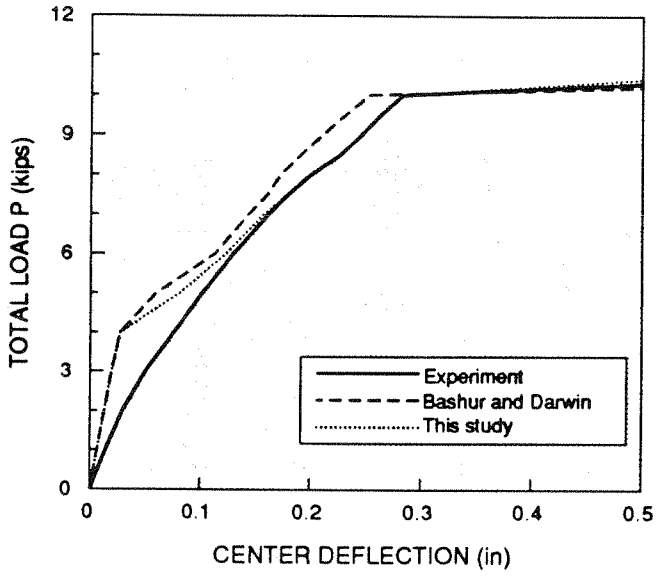

Fig. 4.16 Load-Deflection Relationship of Beam T1MA

relation and any other material properties not specifically mentioned in Table 4.1 are the same as those used in the analysis of beam J-4, since the concrete composition and strength of the two specimens is not much different.

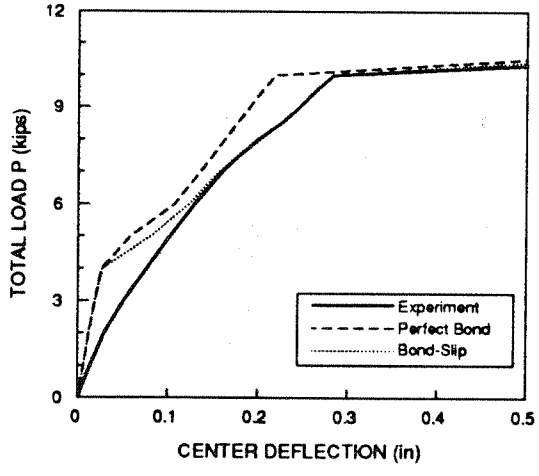

Fig. 4.17a Bond-Slip and Tension Stiffening Effect of Beam T1MA

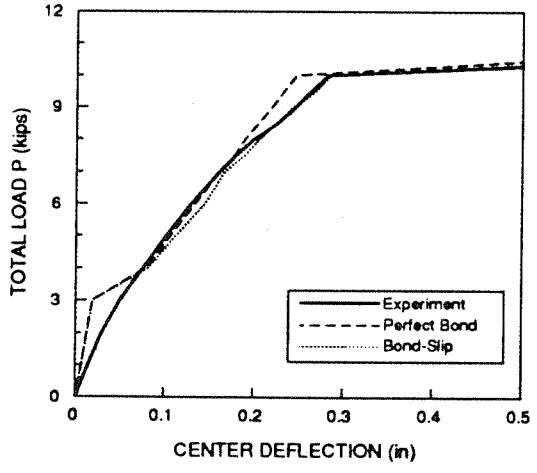

Fig. 4.17b Bond-Slip Effect without Tension Stiffening of Beam T1MA

Fig. 4.16 compares the analytical results with the measured load-deflection relation of specimen T1MA. The results of a previous study by Bashur and Darwin (1978) are also shown in Fig. 4.16. The results of the proposed model in Fig. 4.16 include the effects of tension stiffening and bond slip. The initial discrepancy between analysis and experiment stems from the fact that the specimen was probably extensively cracked before loading. Otherwise the proposed model shows very satisfactory agreement with the measured response.

Figs. 4.17a and b show the effect of tension stiffening and bond slip and the relative contribution of each source of deformation to the load-displacement response of the specimen. It is concluded that the contribution of tension stiffening and bond-slip is of comparable magnitude but of opposite effect near the ultimate load of the specimen, in agreement with the results from specimen J-4. Thus the exclusion of both effects in Fig. 4.17b yields good overall agreement between analysis and experiment, even though the analytical response is a little too flexible in the initial post-cracking stage and a little to stiff near yielding of the specimen. This can be attributed to the load dependence of bond damage and the bond-slip contribution.

4.4 Beam to Column Joint Subassemblage

Experimental studies have shown that bond slip has a pronounced effect on the global deformation of beam-column subassemblages which are subjected to loading simulating the effect of high lateral loads. This happens because the anchorage length of the reinforcing bars in the joint does not suffice to transfer to the concrete the steel forces at the beam-column interfaces of the joint. These forces cause the reinforcing bars to be pulled from one end of the joint and pushed from the other, so that a force equal to almost twice the yield force of the bar needs to be transferred to the concrete within the joint. When lateral load reversals occur, the stress transfer problem is aggravated by bond deterioration under cyclic load reversals.

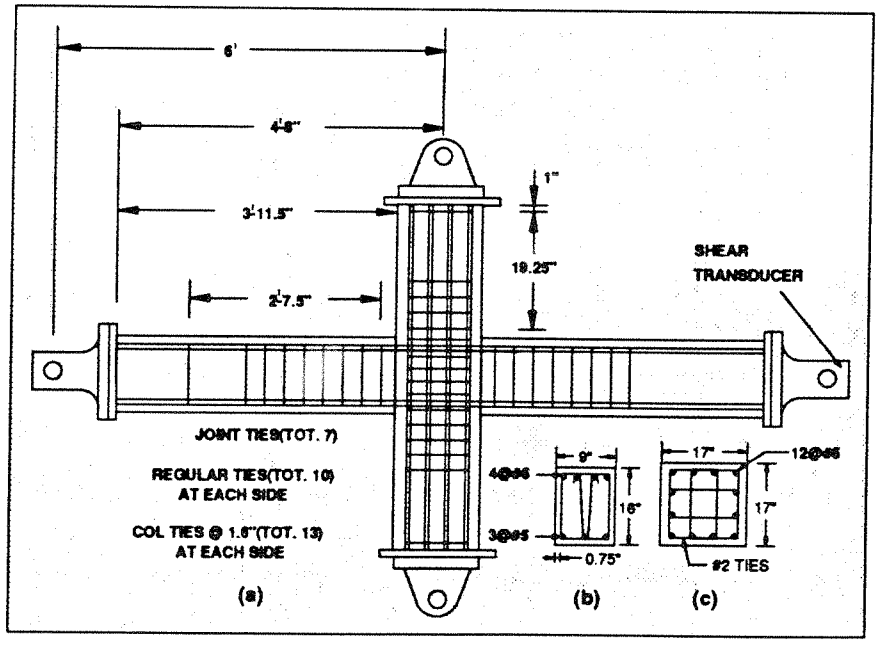

Fig. 4.18 Geometry and Reinforcing Details of Beam to Column Subassemblage

In order to assess the ability of the proposed finite element model to simulate the behavior of beam-column joint subassemblages, specimen BC4, which was tested by Viwathanatepa et al. (1979a), is selected for further study. The subassemblage consisted of two 9 in. by 16 in. girders framing into a 17 in. by 17 in. square column. The dimensions and the reinforcing arrangement of the subassemblage are shown in Fig. 4.18. The column was bolted at the top and bottom to steel clevises for mounting the specimen on the testing frame. The main longitudinal reinforcement of the beams consisted of 4#6 bars at the top and 3#5 bars at the bottom of the section with #2 tied stirrups spaced at 3.5 in. as transverse reinforcement (Fig. 4.18b). The longitudinal reinforcement of the column consisted of 12#6 bars with #2 ties spaced 1.6 in. center-to-center along column providing the transverse reinforcement (Fig. 4.18c). Seven #2 ties were placed inside the beam-column joint region to satisfy the confinement and shear resistance requirements of the building code. The material properties of the specimen are summarized in Table 4.1. The bond stress-slip relation and any other material properties not specifically mentioned in Table 4.1 are the same as those used in the analysis of beam J-4, since the concrete composition and strength of the two specimens is not much different (Viwathanatepa et al. 1979a).

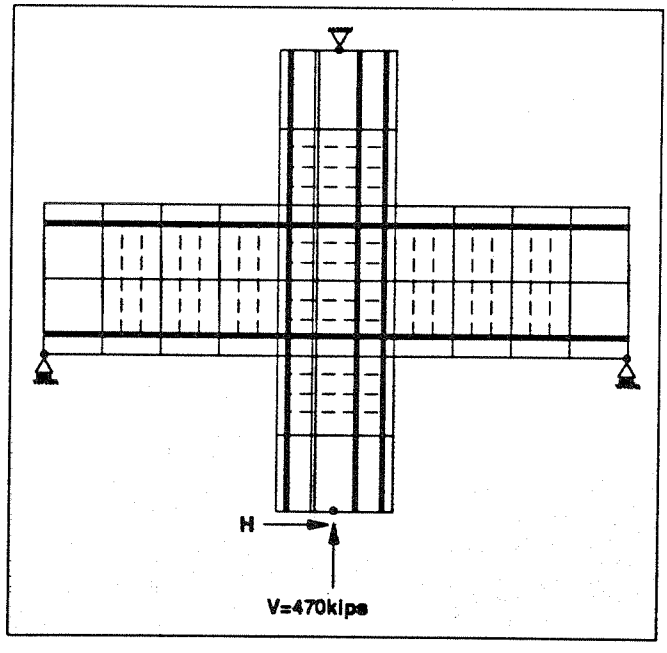

Fig. 4.19 Finite Element Idealization of Beam to Column Subassemblage

The beam-column subassemblage was subjected to a constant axial load P of 470 kips which simulated the effect of gravity loads and a horizontal load H at the lower column end which was cycled to simulate the effect of lateral loads on the subassemblage. Specimen BC4 was subjected to a very severe, pulse-type loading with a single load reversal in order to study the monotonic behavior

of the subassemblage and establish the load-displacement response envelope. Other specimens were then cycled several times with gradually increasing displacement ductility to simulate the effect of earthquake excitation on the subassemblage. Since the load-displacement response of subassemblage BC4 during the first load cycle, which represents a monotonic load test to near failure, was well established during the experiment, it serves as an ideal case study for the proposed model.

The finite element representation of the beam-column subassemblage is shown in Fig. 4.19. Concrete was modeled by 8-node isoparametric elements and the longitudinal and transverse reinforcement was modeled by 2-node truss elements. The bond-slip effect is included in the analysis with bond link elements, as described in Sections 2.4 and 2.5.

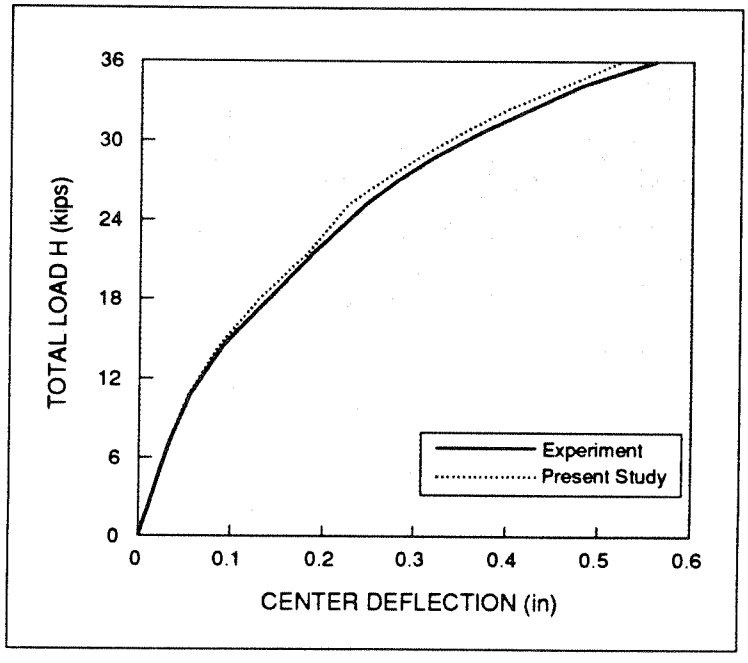

Fig. 4.20 Load-Displacement Relation of Beam to Column Subassemblage

Fig. 4.20 compares the analytical results with the measured load-displacement response of the subassemblage. With the effects of tension stiffening and bond-slip the analysis shows excellent agreement with the experimental results. The lateral force of 36 kips in Fig. 4.20 closely approximates the ultimate load of the specimen.

Fig. 4.21 shows that the effect of bond slip affects the behavior of the subassemblage much more than tension stiffening. In this case the bond-slip of reinforcing bars in the joint contributes approximately 33% of the total deformation of the subassemblage near the ultimate load of 36 kips. The observation of the significance of bond-slip in the beam-column subassemblage agrees with the results of the over-reinforced concrete beam A-1, where the interaction of bond and shear plays a significant role in the response. This interaction also has an important effect on the stress transfer in

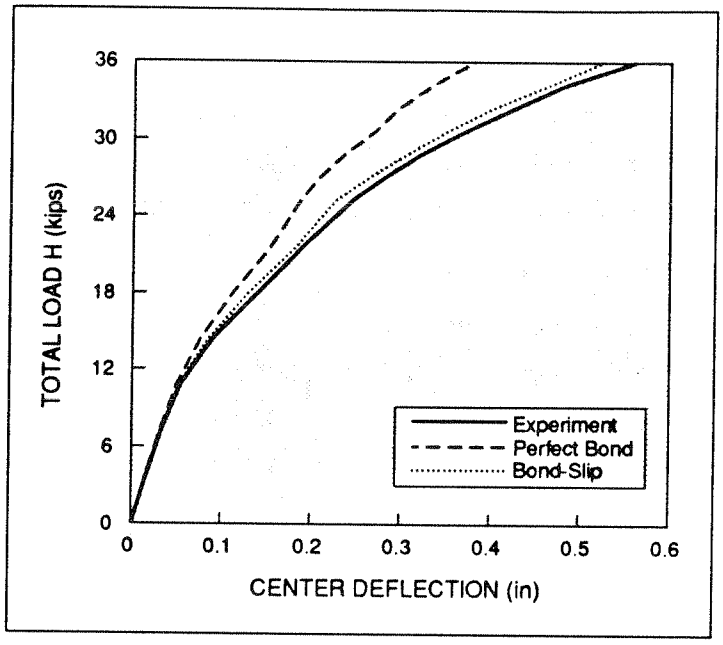

Fig. 4.21 ***Tension Stiffening and Bond-Slip Effect in Beam to Column Subassemblage***

beam-column joints, particularly, when these are subjected to loading simulating the effect of lateral loads. Even though the tension stiffening effect plays a minor role in the response of this beam-column joint, it should not be concluded that it can be excluded from the model, since it helps prevent numerical instability problems in connection with crack formation and propagation.

4.5 Reinforced Concrete Slabs

Tension stiffening has a significant effect in the analysis of RC slabs. In order to investigate the validity of the proposed model a corner-supported two-way slab tested by Jofriet and McNeice (1971) was used in the correlation studies. The slab is square in plan and spans 36 in. with a thickness of 1.75 in. It is reinforced with wire mesh with a steel ratio of 0.85% in both directions and is subjected to a concentrated load at midspan, as shown in Fig. 4.22. The material properties of the specimen are summarized in Table 4.1. This slab was previously studied by a number of investigators (Jofriet and McNeice 1971; Hand et al. 1973; Lin and Scordelis 1975; Bashur and Darwin 1978) and it, therefore, provides a good case study for the comparison of different models with measured data.

Fig. 4.22 shows the finite element representation of one quarter of the slab only, because of symmetry considerations. Nine elements were used in the basic analysis with eight concrete layers through the thickness of the slab for a total of 72 elements.

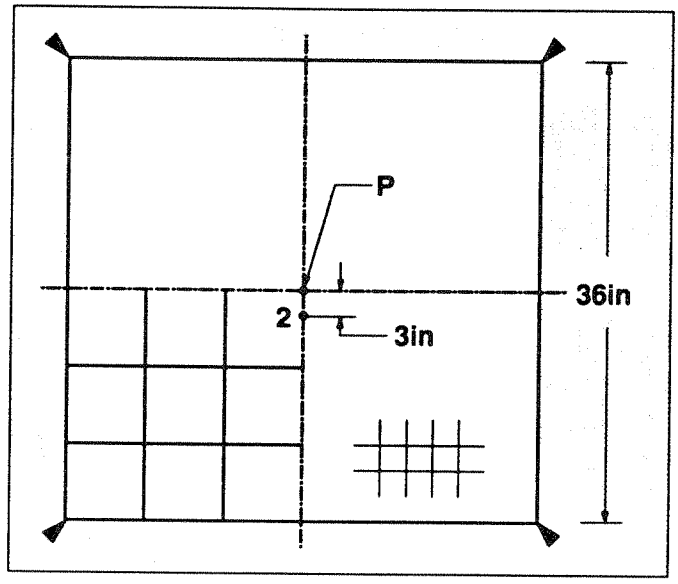

Fig. 4.22 Configuration and Finite Element Discretization of Jofriet-McNeice Slab

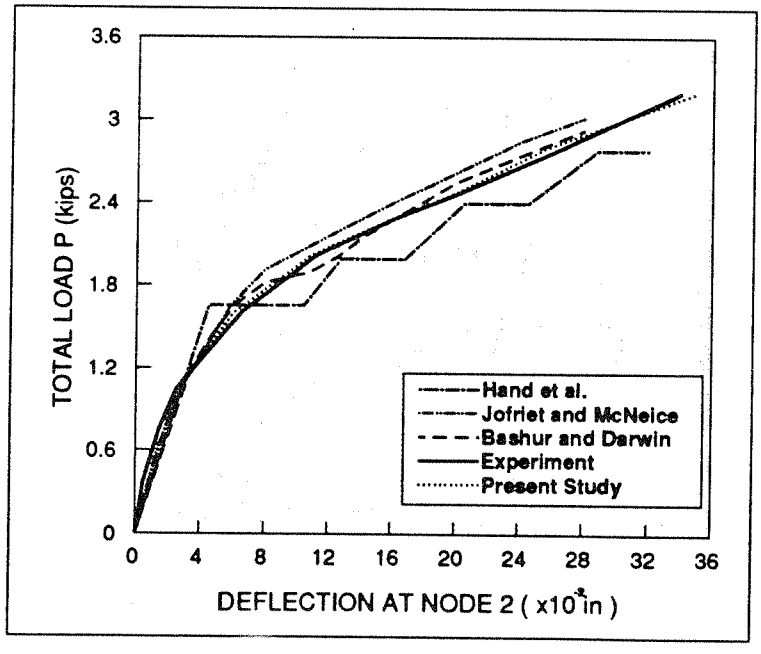

Fig. 4.23 Load-Deflection Relationship at Node 2 in Fig. 4.22

Fig. 4.23 compares the analytical load-deflection relation at node 2 in Fig. 4.22 with measured data. The deflection at node 2 is obtained by interpolation of measured deflections at nearby nodes. Fig. 4.23 shows that the predictions of the proposed model, which is based on a fracture energy criterion, are in very good agreement with experimental data. In the analysis of the same slab Joffriet

and McNeice (1971) used the effective stiffness approach and treated, both, steel and concrete as elastic materials; Lin and Scordelis (1975) included the elasto-plastic behavior of reinforcing steel and concrete and accounted for the coupling effect between membrane and bending action in the slab; Bashur and Darwin (1978) used the analytical moment-curvature relation based on yield line theory to analyze the slab; finally, Hand, Pecknold and Schnobrich (1973) considered both the shear and the in-plane deformation of the slab, but neglected the tension-stiffening effect.

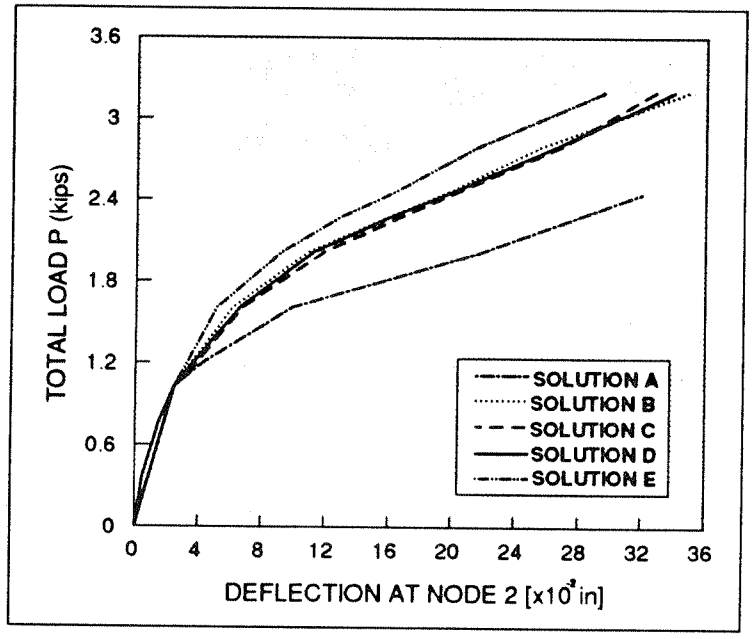

Fig. 4.24 Effect of Mesh Size on Load-Deflection Relation at Node 2

A: No Strain Softening (9 elements)
B: Strain Softening and Element Size Effect Included (9 elements)
C: Strain Softening and Element Size Effect Included (4 elements)
D: Experiment
E: Case C without Element Size Effect

In order to investigate the effect of finite element mesh size on the results, a nine and a four element mesh is used in the finite element idealization of the slab and the results are compared in Fig. 4.24. Solutions **B** and **C** which are obtained by including the tension stiffening effect and the size of the element, as proposed in Section 2.2.3.3, are virtually identical and agree very well with the experimental results. By contrast, solution **E** which does not include the element size effect significantly overestimates the slab deflection. In this case the crack band width extends over the entire element and the model is much more flexible than the real structure. A much finer mesh is required to improve the accuracy of the results at the expense of computational efficiency. Fig. 4.24 also shows that neglecting the strain softening of concrete in solution **A** results in a model which is

stiffer than the actual slab. Fig. 4.24 underlines the significance of tension stiffening in the analysis of slabs and stresses the computational advantage of the proposed model, which is independent on finite element size and thus computationally very efficient.

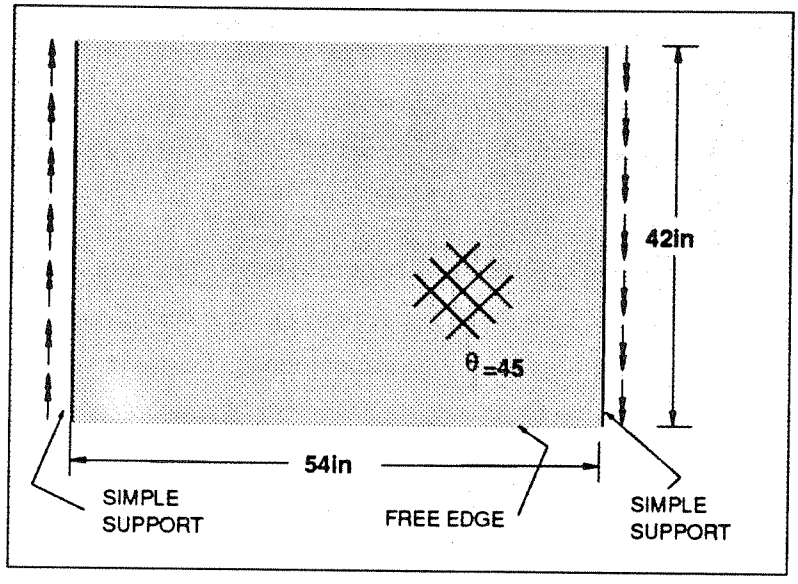

Fig. 4.25 Cardenas Rectangular Slab B7

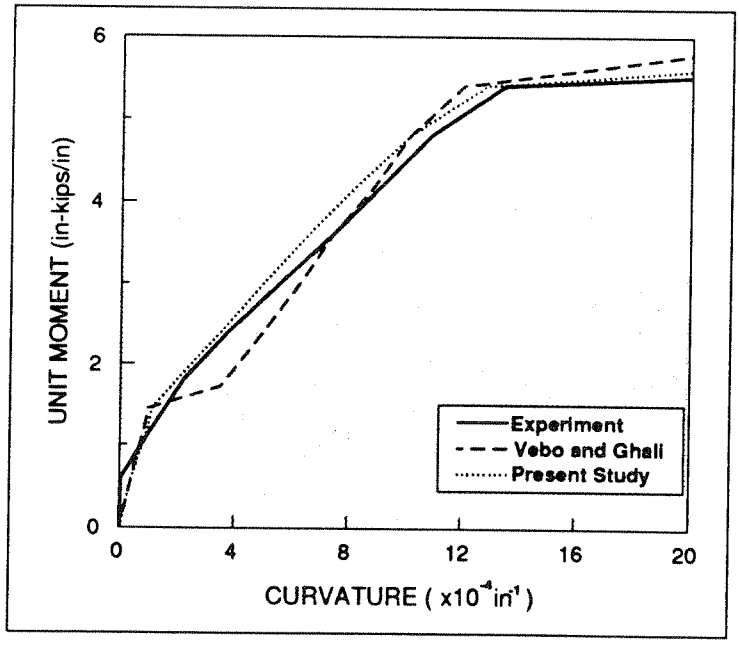

Fig. 4.26 Moment-Curvature Relationships of B7

Finally, the rectangular slab B7 which was tested by Cardenas and Sozen (1968) is used as the last test case of this study. The slab was simply supported along two opposite edges and free along the other two, as shown in Fig. 4.25. Uniformly distributed moments were applied along the simply supported edges. The dimensions of the slab and the loading arrangement are shown in Fig. 4.25. The slab was reinforced with wire mesh oriented at 45° to the edges with equal amount of reinforcement in both directions.

The slab is modeled with nine 8-node isoparametric elements using nine concrete layers through the thickness of the slab for a total of 81 elements. The material properties used in the analysis are summarized in Table 4.1.

Fig. 4.26 compares the experimental moment-curvature relation of the slab with the results of this study and an earlier study by Vebo and Ghali (1977). The results of the present study which include the effects of tension stiffening and finite element mesh size are in very satisfactory agreement with measured data.

CHAPTER 5
CONCLUSIONS

The objective of this study is to develop reliable and computationally efficient finite element models for the analysis of reinforced concrete beams, slabs and beam-column joint subassemblages under monotonic loading conditions. Since this is part of a larger study which endeavors to study the hysteretic behavior of reinforced concrete members, the models developed in this first part should also be general enough, so that they can be extended to cyclic loading conditions.

It is assumed that the behavior of RC beams, slabs and beam-column joints can be described by a plane stress field. Concrete and reinforcing steel are represented by separate material models which are combined together with a model of the interaction between reinforcing steel and concrete through bond-slip to describe the behavior of the composite reinforced concrete material. The material behavior of concrete is described by two failure surfaces in the biaxial stress space and one failure surface in the biaxial strain space. Concrete is assumed as a linear elastic material for stress states which lie inside the initial yield surface. For stresses outside this surface the behavior of concrete is described by a nonlinear orthotropic model, whose axes of orthotropy are parallel to the principal strain directions. The concrete stress-strain relation is derived from equivalent uniaxial relations in the axes of orthotropy. The behavior of cracked concrete is described by a system of orthogonal cracks, which follow the principal strain directions and are thus rotating during the load history. Crushing or cracking of concrete takes place when the strains lie outside the ultimate surface in the biaxial strain space.

A new smeared finite element model is proposed based on an improved cracking criterion, which is derived from fracture mechanics principles. This model retains objectivity of the results for very large finite elements, since it considers cracking to be concentrated over a small region around the integration point and not over the entire finite element, as do previous models.

A new reinforcing steel model which is embedded inside a concrete element, but accounts for the effect of bond-slip is developed. This model results in significant savings in the number of nodes needed to account for the effect of bond-slip, particularly, in three dimensional finite element models. A new nonlinear solution scheme is developed in connection with this model.

The correlation studies between analytical and experimental results and the parametric studies associated with them lead to the following conclusions:

- The effect of tension-stiffening is important in the analysis of RC beams, but more so in the analysis of RC slabs.
- The inclusion of tension-stiffening is important for the independence of the analytical results from the size of the finite element mesh, but also for avoiding numerical problems in connection with crack formation and propagation.
- Present smeared models are too stiff in connection with large finite elements. A new criterion which limits the effect of tension stiffening to the vicinity of the integration point yields very satisfactory results.
- The effect of bond-slip is very important in the analysis of RC beams and beam-column subassemblages even under monotonic loads. This effect is more pronounced in heavily reinforced beams and in beam-column joints, which are subjected to loads simulating the effect of lateral loads on the structure.
- Tension-stiffening and bond-slip cause opposite effects on the response of RC members. While tension-stiffening, which accounts for the concrete tensile stresses between cracks, increases the stiffness of the member, bond-slip leads to a stiffness reduction. In lightly reinforced beams, these effects can cancel each other at certain load stages, thus, leading to the erroneous impression that they can be neglected in the analysis. Since bond-slip increases with loading, while tension-stiffening does not, consistent results can only be obtained when both effects are included in the model. Moreover, the effect of bond-slip clearly outweighs the contribution of tension-stiffening in heavily reinforced beams and beam-column joint subassemblages. In these cases the exclusion of the bond-slip effect can lead to significant overestimation of the stiffness of the member.
- The tensile strength of concrete has insignificant effect on the load-displacement response of RC beams. Crack formation and propagation is rather influenced by the fracture energy of concrete.
- The value of the cracked shear constant λ has negligible effect on the response of slender RC beams in bending, since most of the member is in the stress state of compression-compression or tension-tension and only a small portion of the structure near the supports is in a stress state of tension-compression. It is only under a stress state of tension-compression that the coupling between normal and shear strains represented by the cracked shear constant λ plays an important role. While this coupling effect is negligible in the case of slender beams in bending, it becomes significant in the analysis of shear walls and deep beams.

REFERENCES

Abdel Rahman, H.H. and Hinton, E. (1986). "Nonlinear Finite Element Analysis of Reinforced Concrete Stiffened and Cellular Slabs". *Computers & Structures*, Vol. 23, No. 3, pp. 333-350.

Adeghe, L.N. and Collins, M.P. (1986). "A Finite Element Model for Studying Reinforced Concrete Detailing Problems". *Publication No. 86-12*, Department of Civil Engineering, University of Toronto.

Arnesen, A., Sorensen, S. I. and Bergan, P.G. (1980). "Nonlinear Analysis of Reinforced Concrete". *Computers & Structures*, Vol. 12, pp. 571-579.

ASCE Task Committee on Finite Element Analysis of Reinforced Concrete Structures. (1982). *State-of-the-Art Report on Finite Element Analysis of Reinforced Concrete*, ASCE Special Publications.

Balakrishnan, S. and Murray, D.W. (1988). "Concrete Constitutive Model for NLFE Analysis of Structures". *Journal of Structural Engineering, ASCE*, Vol. 114, No. 7, pp. 1449-1466.

Barzegar, F. and Schnobrich, W.C. (1986). "Nonlinear Finite Element Analysis of Reinforced Concrete under Short Term Monotonic Loading". *Civil Engineering Studies SRS No. 530*, Univ. of Illinois at Urbana, Illinois.

Bashur, F.K, and Darwin, D. (1978). "Nonlinear Model for Reinforced Concrete Slabs". *Journal of Structural Division, ASCE*, Vol. 104, No. ST1, pp. 157-170.

Bazant, Z.P. and Cedolin, L. (1980). "Fracture Mechanics of Reinforced Concrete". *Journal of the Engineering Mechanics, ASCE*, Vol. 106, No. EM6, pp. 1287-1306.

Bazant, Z.P. and Cedolin, L.. (1983). "Finite Element Modeling of Crack Band Propagation". *Journal of Structural Engineering, ASCE*, Vol. 109, No. 1, pp. 69-93.

Bazant, Z.P. and Oh, B.H. (1983). "Crack Band Theory for Fracture of Concrete". *Materials and Structures*, RILEM, Paris, Vol. 16, pp. 155-176.

Bazant, Z.P. and Ozbolt, J. (1989) "Nonlocal Microplane Model for Fracture, Damage, and Size Effect in Structures", *Journal of Engineering Mechanics, ASCE*, Vol. 116, No. 11.

Becker, J.M. and Bresler, B.. (1974). "FIRES-RC-A Computer Program for the Fire Response of Structures-Reinforced Concrete Frames". *Report No. UCB/FRG 74-3*, Department of Civil Engineering, University of California, Berkeley.

Bedard, C. and Kotsovos, M.D.. (1986). "Fracture Processes of Concrete for NLFEA Methods". *Journal of Structural Engineering, ASCE*, Vol. 112, No. 3, pp. 573-587.

Bergmann, R. and Pantazopoulou, V. A. (1988). "Finite Element for R/C Shear Walls Under Cyclic Loads". Department of Civil Engineering, *Report UCB/SEMM-88/09*, University of California, Berkeley, 1988.

de Borst, R. and Nauta, P. (1985) "Non-Orthogonal Cracks in a Smeared Finite Element Model". *Engineering Computations*, Vol. 2, pp. 35-46.

Bresler, B. and Scordelis, A.C. (1963). "Shear Strength of Reinforced Concrete Beams". *Journal of ACI*, Vol. 60, No. 1, pp. 51-72.

Bresler, B. and Bertero, V.V. (1968). "Behavior of Reinforced Concrete Under Repeated Load". *Journal of the Structural Division, ASCE*, Vol. 94, No. ST6, pp. 1567-1590.

Broek, D. (1974). **Elementary Engineering Fracture Mechanics**, Sijthoff & Noordoff, London.

Burns, N.H. and Siess, C.P. (1962). "Load-Deformation Characteristics of Beam-Column Connections in Reinforced Concrete". Civil Engineering Studies, SRS No. 234, University of Illinois, Urbana.

Cardenas A. and Sozen, M.A. (1968). "Strength and Behavior of Isotropally and Nonisotropally Reinforced Concrete Slabs Subjected to Combinations of Flexural and Torsional Moments". *Civil Engineering Studies SRS No. 336*, Univ. of Illinois at Urbana, Illinois.

Comité Euro-International du Beton (CEB) (1978). **CEB-FIP Model Code of Concrete Structures**. Bulletin d'Information 124/125E, Paris, France.

Cervenka, V. (1970). "Inelastic Finite Element Analysis of Reinforced Concrete Panels". *Ph.D. Dissertation*, University of Colorado, Boulder.

Cervenka, V., Eligehausen, R. and Pukl, R. (1990). "SBETA-Computer Program for Nonlinear Finite Element Analysis of Reinforced Concrete Structures". *Report 90/1*, Institute of Building Materials, University of Stuttgart.

Chang, T.Y., Taniguchi, H. and Chen, W. F. (1987). "Nonlinear Finite Element Analysis of Reinforced Concrete Panels". *Journal of Structural Engineering, ASCE*, Vol. 113, No. 1, pp. 122-140.

Chen, W.F. (1976). **Plasticity in Reinforced Concrete**, McGraw-Hill, New York.

Chia, C.Y. (1978). **Nonlinear Analysis of Plates**, McGraw-Hill, New York.

Ciampi, V., Eligehausen, R., Bertero, V.V. and Popov, E.P. (1982). "Analytical Model for Concrete Anchorages of Reinforcing Bars under Generalized Excitations". *Report No EERC 82-23*, Earthquake Engineering Research Center, University of California, Berkeley.

Cope, R.J., Rao, P.V., Clark, L.A. and Norris, R. (1980). "Modeling of Reinforced Concrete Behavior for Finite Element Analysis of Bridge Slabs". *Numerical Methods for Nonlinear Problems* , C. Taylor, E. Hinton and D.R.J. Oden, eds., Pineridge Press, Swansea, pp. 457-470.

Crisfield, M.A. (1982). "Accelerated Solution Techniques and Concrete Cracking". *Computer Methods in Applied Mechanics and Engineering*, Vol. 33, pp. 585-607.

Darwin, D. and Pecknold, D.A. (1977). "Analysis of Cyclic Loading of Plane R/C Structures". *Computers & Structures*, Vol. 7, No. 1, pp. 137-147.

Desai, C.S. and Siriwardance, H.J. (1972). **Constitutive Laws for Engineering Materials**, Prentice-Hall, Englewood Cliffs, New Jersey.

Dotroppe, J.C., Schnobrich, W.C. and Pecknold, D.A. (1973). "Layered Finite Element Procedure for Inelastic Analysis of Reinforced Concrete Slabs". *IABSE Publication*, Vol. 33-11.

Dougill, J.W. (1976). "On Stable Progressively Fracturing Solids," *Journal of Applied Mathematics and Physics*, Vol. 27, pp. 423-437.

Eligehausen, R., Popov, E.P. and Bertero, V.V. (1983). "Local Bond Stress-Slip Relationships of Deformed Bars Under Generalized Excitations". *Report No. UCB/EERC 83-23*, Earthquake Engineering Research Center, University of California, Berkeley.

Filippou, F.C., Popov, E.P., and Bertero, V.V. (1983). "Effects of Bond Deterioration on Hysteretic Behavior of Reinforced Concrete Joints". *Report No. UCB/EERC-83/19*, Earthquake Engineering Research Center, University of California, Berkeley.

Filippou, F.C. (1986). "A Simple Model for Reinforcing Bar Anchorages Under Cyclic Excitations". *ASCE, Journal of Structural Engineering*, Vol. 112, No. 7, pp. 1639-1659.

Franklin, H.A. (1970). "Non-Linear Analysis of Reinforced Concrete Frames and Panels". *Ph.D. Dissertation*, Division of Structural Engineering and Structural Mechanics, University of California, Berkeley, SEMM 70-5.

Gaston, J.R., Siess, C.P. and Newmark, N.M. (1972). "A Layered Finite Element Non-Linear Analysis of Reinforced Concrete Plates and Shells". *Civil Engineering Studies, SRS No. 389*, University of Illinois, Urbana.

Gilbert, R.I. and Warner, R.F. (1978). "Tension Stiffening in Reinforced Concrete Slabs". *Journal of Structural Division, ASCE*, Vol. 104, No. ST12, pp. 1885-1900.

de Groot, A.K., Kusters, G.M.A. and Monnier, T. (1981). "Numerical Modeling of Bond-Slip Behavior". *Heron, Concrete Mechanics*, Vol. 26, No. 1B.

Gupta, A.K. and Akbar, H. (1983). "A Finite Element for the Analysis of Reinforced Concrete Structures". *International Journal for Numerical Methods in Engineering*, Vol. 19, pp. 1705-1712.

Hand, F.R., Pecknold, D.A. and Schnobrich, W.C. (1973). "Nonlinear Layered Analysis of RC Plates and Shells". *Journal of Structural Division, ASCE*, Vol. 99, No. ST7, pp. 1491-1505.

Hayashi, S. and Kokusho, S. (1985). "Bond Behavior in the Neighborhood of the Crack". *Proceedings of the U.S.-Japan Joint Seminar on Finite Element Analysis of Reinforced Concrete*, pp. 364-373, Tokyo, Japan.

Hillerborg, A., Modeer, M. and Petersson, P.E. (1976). "Analysis of Crack Formation and Growth in Concrete by Means of Fracture Mechanics and Finite Element". *Cement and Concrete Research*, Vol. 6, No. 6, pp. 773-782.

Hognestad, E. (1951). "A Study of Combined Bending and Axial Load in Reinforced Concrete Members". University of Illinois Engineering Experiment Station, *Bulletin Series No. 399*, Bulletin No. 1.

Jain, S.C. and Kennedy, J.B. (1974). "Yield Criterion for Reinforced Concrete Slabs," *Journal of Structural Division, ASCE*, Vol. 100, No. ST3, pp. 631-644.

Jenq, Y.S. and Shah, S.P. (1986). "Crack Propagation in Fiber-Reinforced Concrete". *Journal of Structural Engineering, ASCE*, Vol. 112, No. 1, pp. 19-34.

Jofriet, J.C. and McNeice, G.M. (1971). "Finite Element Analysis of RC Slabs". *Journal of Structural Division, ASCE*, Vol. 97, No. ST3, pp. 785-806.

Keuser, M. and Mehlhorn, G. (1987). "Finite Element Models for Bond Problems". *Journal of Structural Engineering, ASCE*, Vol. 113, No. 10, pp. 2160-2173.

Kupfer, H., Hilsdorf, H.K. and Rüsch, H. (1969). "Behavior of Concrete under Biaxial Stresses". *ACI Journal*, Vol. 66, No. 66-62, pp. 656-666.

Kwak, H.G. (1990). "Material Nonlinear Finite Element Analysis and Optimal Design of Reinforced Concrete Structures". *Ph.D. Dissertation*, Department of Civil Engineering, KAIST, Korea.

Leibengood, L.D., Darwin, D. and Dodds, R.H. (1986). "Parameters Affecting FE Analysis of Concrete Structures," *Journal of Structural Engineering, ASCE*, Vol. 112, No. 2, pp. 326-341.

Lin, C.S. and Scordelis, A.C. (1975). "Nonlinear Analysis of RC Shells of General Form". *Journal of Structural Division, ASCE*, Vol. 101, No. ST3, pp. 523-538.

Meyer, C. and Okamura, H., eds. (1985). "Finite Element Analysis of Reinforced Concrete Structures". *Proceedings of the US-Japan Joint Seminar on Finite Element Analysis of Reinforced Concrete*, Tokyo, Japan.

Milford, R.V. and Schnobrich, W.C. (1984). "Nonlinear Behavior of Reinforced Concrete Cooling Towers". *Civil Engineering Studies SRS No. 514*, Univ. of Illinois at Urbana, Illinois.

Nayak, G.C. and Zienkiewicz, O.C. (1972). "Elasto-Plastic Stress Analysis". *International Journal of Numerical Methods in Engineering*, Vol. 5, pp. 113-135.

Ngo, D. and Scordelis, A.C. (1967). "Finite Element Analysis of Reinforced Concrete Beams," *Journal of ACI*, Vol. 64, No. 3, pp. 152-163.

Nilson, A.H. (1972). "Internal Measurement of Bond Slip". *Journal of ACI*, Vol. 69, Title No. 69-41, pp. 439-441.

Owen, J. and Hinton, E. (1978). **Finite Elements in Plasticity**, Pineridge Press, Swansea.

Park, P. and Paulay, T. (1975). **Reinforced Concrete Structures** John Wiley & Sons, New York.

Popovics, S. (1969). "A Review of Stress-Strain Relationships for Concrete". *Journal of ACI*, Vol. 66, No. 5, pp. 756-764.

Rajagopal, K.R. (1976). "Nonlinear Analysis of Reinforced Concrete Beams, Beam-Columns and Slabs by Finite Elements". *Ph.D. Dissertation*, Iowa State University.

Rashid, Y.R. (1968). "Analysis of Prestressed Concrete Pressure Vessels". *Nuclear Engineering and Design*, Vol. 7, No. 4, pp. 334-344.

Reinhardt, H.W. (1986). "The Role of Fracture Mechanics in Rational Rules for Concrete Design". *IABSE Surveys*, Vol. S-34, pp. 1-15.

Rots, J.G., Nauta, P., Kusters, G.M.A. and Blaauwendraad, J. (1985). "Smeared Crack Approach and Fracture Localization in Concrete". *HERON*, Vol. 30, No. 1, pp. 3-48.

Scanlon, A. and Murray, D.W. (1974). "Time Dependent Reinforced Concrete Slab Deflections". *Journal of the Structural Division, ASCE*, Vol. 100, No. ST9, pp. 1911-1924.

Scordelis, A.C., Ngo, D. and Franklin, H.A. (1974). "Finite Element Study of Reinforced Concrete Beams with Diagonal Tension Cracks". *Proceedings of Symposium on Shear in Reinforced Concrete, ACI Publication SP-42.*

Selna, L.G. (1969). "Creep, Cracking and Shrinkage in Concrete Frame Structures". *Journal of the Structural Division, ASCE*, Vol. 95, No. ST12, pp. 2743-2761.

Suidan, M.T. and Schnobrich, W.C. (1973). "Finite Element Analysis of Reinforced Concrete". *Journal of the Structural Division, ASCE*, Vol. 99, No. ST10, pp. 2109-2122.

Tasuji, M.E., Slate, F.O. and Nilson, A.H. (1978). "Stress-Strain Response and Fracture of Concrete in Biaxial Loading". *Journal of ACI*, Vol. 75, No. 3, pp. 306-312.

Taylor, C. and Hinton, E. (1980). **Numerical Methods for Nonlinear Problems**, Pineridge Press, Swansea.

Vebo, A. and Ghali, A. (1977). "Moment-Curvature Relation of Reinforced Concrete Slabs". *Journal of Structural Division, ASCE*, Vol. 103, No. ST3, pp. 515-531.

Vecchio, F. and Collins, M.P. (1982). "The Response of Reinforced Concrete to In-Plane Shear and Normal Stress". *Publication No. 82-03*, Department of Civil Engineering, University of Toronto, Toronto, Canada.

Viwathanatepa, S., Popov, E.P. and Bertero, V.V. (1979a). "Seismic Behavior of Reinforced Concrete Interior Beam-Column Subassemblages". *Report No. UCB/EERC-79/14*, Earthquake Engineering Research Center, University of California, Berkeley.

Viwathanatepa, S., Popov, E.P. and Bertero, V.V. (1979b). "Effects of Generalized Loadings on Bond of Reinforcing Bars Embedded in Confined Concrete Blocks". *Report No EERC 79-22*, Earthquake Engineering Research Center, University of California, Berkeley.

Wamba, T.E. (1980). "Nonlinear Analysis of Reinforced Concrete Beams by Finite Element Method". *Ph.D. Dissertation*, Department of Civil Engineering, State University of New York at Buffalo.

Welch, G.B. and Haisman, B. (1969). "Fracture Toughness Measurements of Concrete". *Report No. R42*, University of New South Wales, Sydney, Australia.

Wunderlich, W., Stein, E. and Bathe, K.J., eds. (1980). Nonlinear Finite Element Analysis in Structural Mechanics, *Proceedings of the Europe-US Workshop*, Ruhr-University, Germany.

Yankelevsky, D.Z. (1985). "New Finite Element for Bond-Slip Analysis", *Journal of Structural Engineering, ASCE*, Vol. 111, No. 7, pp. 1533-1542.

Yoshikawa, Y. and Tanabe, T. (1987). "An Analytical Model for Frictional Shear Slip of Cracked Concrete". *IABSE Colloquium Computational Mechanics of Concrete Structures*, pp. 75-86, Delft University, Netherlands.

Zulfiqar, N. and Filippou, F.C. (1990). "Models of Critical Regions in Reinforced Concrete Frames under Seismic Excitations". *Report No. UCB/EERC-90/06*, Earthquake Engineering Research Center, University of California, Berkeley.